WAVEFORM-SIMILARITY LINK ANALYSIS FOR LOW FREQUENCY EARTHQUAKE DETECTION

A DISSERTATION

SUBMITTED TO THE DEPARTMENT OF GEOPHYSICS

AND THE COMMITTEE ON GRADUATE STUDIES

OF STANFORD UNIVERSITY

IN PARTIAL FULFILLMENT OF THE REQUIREMENTS

FOR THE DEGREE OF

DOCTOR OF PHILOSOPHY

ANA CRISTINA AGUIAR MOYA

MARCH 2015

This dissertation is online at: http://purl.stanford.edu/yh695wn8051

I certify that I have read this dissertation and that, in my opinion, it is fully adequate in scope and quality as a dissertation for the degree of Doctor of Philosophy.

Gregory Beroza, Primary Adviser

I certify that I have read this dissertation and that, in my opinion, it is fully adequate in scope and quality as a dissertation for the degree of Doctor of Philosophy.

Jesse Lawrence

I certify that I have read this dissertation and that, in my opinion, it is fully adequate in scope and quality as a dissertation for the degree of Doctor of Philosophy.

Paul Segall

Approved for the Stanford University Committee on Graduate Studies.

Patricia J. Gumport, Vice Provost for Graduate Education

This signature page was generated electronically upon submission of this dissertation in electronic format. An original signed hard copy of the signature page is on file in University Archives.

Abstract

Slow slip events were first detected by GPS as a reversal of motion of the Earth's surface due to episodic slip on the deep extension of the Cascadia subduction zone, down dip of the seismogenic zone (Dragert *et al.*, 2001; Miller *et al.*, 2002). They were initially thought to be silent, but later related to a seismic signal resembling coherent noise across a network. This signal was called non-volcanic tremor (Obara, 2002; Dragert *et al.*, 2004) and the association of the tremor and slow slip sources came to be called Episodic Tremor and Slip (ETS) (Rogers and Dragert, 2003). Since its discovery, this type of event has been found in many tectonic regimes and other seismic signals, such as low frequency earthquakes (LFEs), have been associated with them, as a manifestation of the same process at depth. LFEs were originally found in Japan within tectonic tremor (Katsumata and Kamaya, 2003). Tectonic tremor was later described as a superposition of LFEs, making it possible to locate the tremor with greatly improved accuracy (Shelly *et al.*, 2006; Shelly *et al.*, 2007b). Initially, LFEs were found in Japan by visual inspection. These were then used as templates to find other LFEs within the tremor using a match filter technique (Shelly *et al.*, 2007a; Shelly *et al.*, 2007b). An autocorrelation method was later developed to find the repeating signals where templates were not known (Brown *et al.*, 2008). Both of these methods are based on detection in a pair wise manner but do not exploit the fact that LFE signals repeat many times.

I have derived a method based on autocorrelation that exploits the repetitive nature of the LFEs. To do this I apply Google's PageRank algorithm to the window pairs found as matches above a statistically significant threshold. This algorithm ranks windows based on the links to other windows, and considers both direct and indirect links. With this, the PageRank algorithm takes into account the complex hierarchical relationships between windows and assigns a ranking to each window based on all

links. I use the PageRank results to create robust templates by stacking windows linked directly and indirectly to the highest ranked window.

I validate this method against data from the April 2006 Shikoku, Japan tremor episode and find that stacks created using the PageRank algorithm match known LFEs from the JMA catalog that locate to the same area of LFEs from the 2006 event. Using these templates we find similar detections to Shelly *et al.* (2007a) for the same time periods, but also find detections for weaker segments of tremor not previously reported. I also show that the PageRank algorithm can help differentiate between tremor and noise by using the histogram of its the probabilities where tremor data show far greater numbers of highly ranked values and noise data shows relatively fewer numbers of high values.

I have applied the PageRank algorithm to two new data sets. The first is from Northern New Zealand, where tremor is not easily observed due to attenuation and a limited seismic coverage (Kim *et al.*, 2011). I create stacks using the PageRank algorithm for different tremor bursts during this slow slip event. I find that LFE templates from different small tremor bursts have a high correlation suggesting a similar source for both. Using these templates, I detect many LFEs within the tremor bursts as well as outside of the tremor, suggesting that the tremor may not be easily observed in this data set.

The second data set I applied my method to is tremor in southern Taiwan. Here tremor has been found to be triggered by surface waves and also occurs spontaneously (Peng and Chao, 2008; Tang *et al.*, 2010; Chao *et al.*, 2012). It is composed of LFEs (Peng and Chao, 2008), which were found manually and later used as templates. I applied the PageRank algorithm both during triggered and ambient tremor. I found a repeating signal in both data sets and find that the stacks created from data during the triggered tremor closely match the stacks created from ambient tremor suggesting a similar location for both.

Finally, as a different focus, I use estimates of attenuation terms from Ground Motion Prediction Equations calculated from tremor in Cascadia (Baltay and Beroza (2013)) to map the spatial variability of the amplitude attenuation term across the northern Cascadia subduction zone.

To Brian

I would not have accomplished this
without your support.

Acknowledgements

I would like to thank my advisor, Greg, for giving me the opportunity of a lifetime. Thank you for guiding me through this rollercoaster of a PhD, for always having encouraged me on the many times I felt I was hitting another wall and for pushing me to work hard. I am also grateful to my committee members, Jesse and Paul, for always having insightful comments and crucial questions that helped me push my research further.

It is safe to say at this point that this was not easy, and if I would not have been so lucky to find such an amazing family here at Stanford it would have been even harder. I never knew I could acquire such an international family, but that is exactly what has happened to me here at Stanford. Katherine, Alec and Rob, your support and friendship through my years here was amazing and I am very grateful for all the fun times we have shared together. Mandy, Elita and Ohad, I have learned so much from you and I can say that my programming skills are in a much better place because of you. Angie, what a blessing to have had you as my officemate, thank you for being such a wonderful friend, for all the words of advice and always sharing a friendly ear as it was needed plenty of times. And lastly, Randi, I believe I have found in you the little sister I never had. Thank you for sharing so many awesome baking moments with me, as you know that sugar and chocolate are always therapeutic. Your friendship has been key in helping me get through the hardest part, the end!

I also want to thank all the girls in my research group. Annemarie, Marine, Sarah and Clara, what would I have done without all of you! Any challenge, from personal to research to computational, you have always been there for me and helped me when things were falling apart no matter what it was. I am also grateful to have

learned that I had some sort of hidden art and craft talents, something I never knew and definitely owe to you.

Lastly, I would like to thank my family. Their support through so many years of school has always been amazing. Knowing that they believe in me, no matter what, is a priceless treasure. This has given me the strength to pursue all my dreams and to keep trying when it has not been easy. Gracias Mami y Papi! And to save the best for last, I would like to thank Brian. Your patience, companionship, love and support have been the main reason I was able to get through the ups and downs of the past 6 years. Thank you for holding me in one piece during this part of my life!

Table of Contents

List of Tables

List of Figures

CHAPTER 1

Introduction

Using Hi-Net data in southwest Japan, Obara (2002) discovered a new type of seismic source that he called "non-volcanic tremor" due to its similarity to volcanic tremor, but distinct origin. Non-volcanic tremor is characterized by weak signals, typically of deep (> 30 km) origin, that, in Japan, are most prominent in the 1-10 Hz frequency band. At about the same time, slow slip events were observed in the Cascadia subduction zone, and were shown to be a reversal of crustal motion observed on GPS stations across the network. These signals were first thought to be silent (Dragert *et al.*, 2001; Miller *et al.*, 2002), in that it was believed that they were not accompanied by a detectable seismic signal (Linde *et al.*, 1988), since they were thought to have rupture rates lower than can be detected by most seismic instruments (Melbourne *et al.*, 2002). It was also recognized that this type of earthquake could last from a few days to a few weeks. To date, slow slip events have not only been seen in Cascadia but in other convergent margins such as Japan, Alaska, Mexico, Costa Rica and New Zealand (Rogers and Dragert, 2003; Brown *et al.*, 2005; McCaffrey *et al.*, 2008; Payero *et al.*, 2008; Peterson and Christensen, 2009), and in other tectonic environments as well.

Slow slip was later related to the newly discovered non-volcanic tremor signal, now known as tectonic tremor (Figure 1.1), and it was evident that it was a manifestation of the same process at depth (Rogers and Dragert, 2003; Obara and Hirose, 2006).

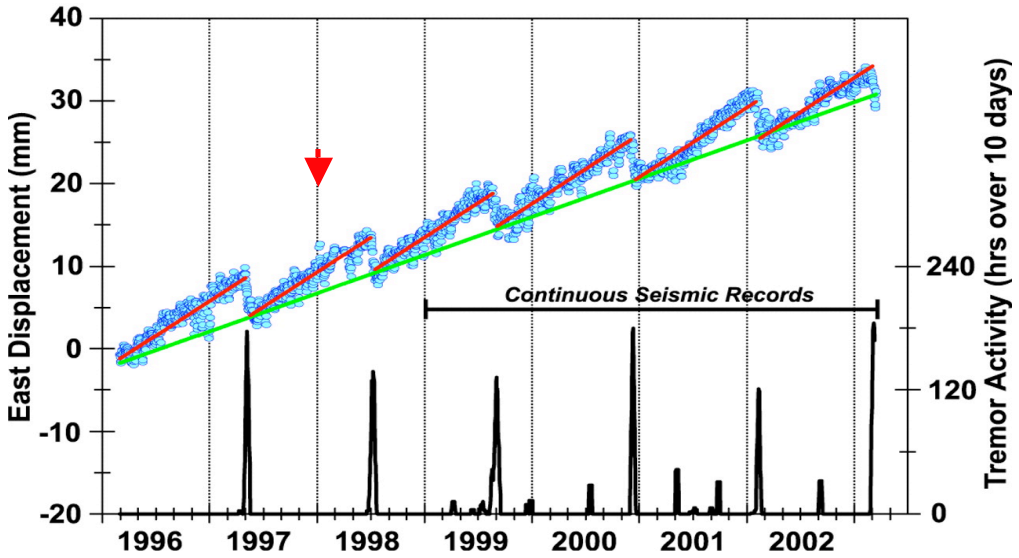

Figure 1.1: From Rogers and Dragert (2003). Comparison of slip and tremor activity observed for the Victoria, BC. Blue circles show daily changes in the east component of the GPS site ALBH (Victoria). Green line shows the long-term (interseismic) eastward motion and red line segments show the mean elevated eastward trends between the slip events. Black lines shows the total number of hours of tremor activity observed for southern Vancouver Island within a sliding 10-day period.

Tectonic tremor is challenging to locate because it is an extended and persistent signal, but lacks the clear *P*- and *S*-wave arrivals that are typical of earthquakes (Obara, 2002). Despite this, there is clear modulation of tremor amplitudes that can be tracked between stations and used to localize the tremor source. Several envelope methods were applied to detect and locate tremor though they offer only weak constraints on depth as a result of errors in arrival time measurements (Obara, 2002; McCausland *et al.*, 2005; Aguiar *et al.*, 2007; Wech and Creager, 2008).

Like slow slip events, tectonic tremor has not only been observed in Japan and Cascadia but also in other places such as Costa Rica and Alaska always associated with the slow slip events (Brown *et al.*, 2005; Peterson and Christensen, 2009). It has also been observed on the San Andreas Fault (Nadeau and Dolenc, 2005) where it is not associated with a detectable slow slip event, but correlates with changes in local seismicity.

Recent studies have revealed that non-volcanic tremor can be triggered by the strong shaking from distant large earthquakes, or teleseisms. Some examples of this are the 2003 Mw 8.1 Tokachi-oki earthquake which triggered tremor in western Shikoku, the Kii peninsula and the Tokai region in Japan (Miyazawa and Mori, 2005), the 2002 M_w 7.8 Denali, Alaska earthquake which triggered tremor on Vancouver Island, British Columbia (Rubinstein *et al.*, 2007) as well as throughout California (Gomberg *et al.*, 2008), and the 2001 Mw 7.8 Kunlun earthquake that triggered tremor beneath the Central Range in Taiwan (Peng and Chao, 2008). So, tectonic tremor does not only occur in subduction zones such as Japan or Cascadia, but in a wider variety of tectonic regimes (Figure 1.2), making this a highly important behavior to understand.

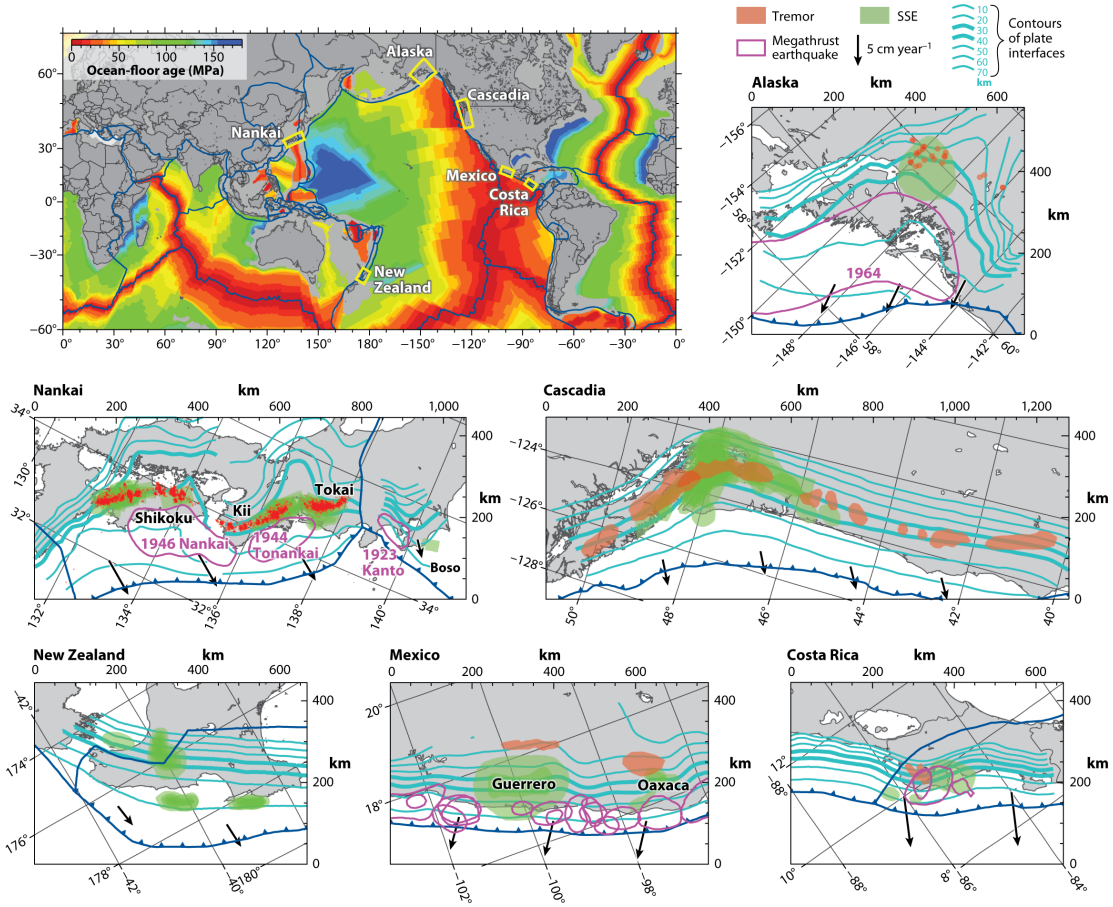

Beroza GC, Ide S. 2011.
Annu. Rev. Earth Planet. Sci. 39:271–96

Figure 1.2: From Beroza and Ide (2011). Tremor and slow-slip events (SSEs) in different subduction zones.

In Japan, tectonic tremor was later shown to be formed by low frequency earthquakes (LFEs) (Shelly *et al.*, 2006; Shelly *et al.*, 2007b). This type of earthquake was initially discovered in Japan, as data analysts observed many events in the data without clear *P*-wave arrivals (Figure 1.3). Given the number of events they were finding in the data, it was decided to add these to the catalog as a new category of events, and they decided to call them LFEs (Katsumata and Kamaya, 2003).

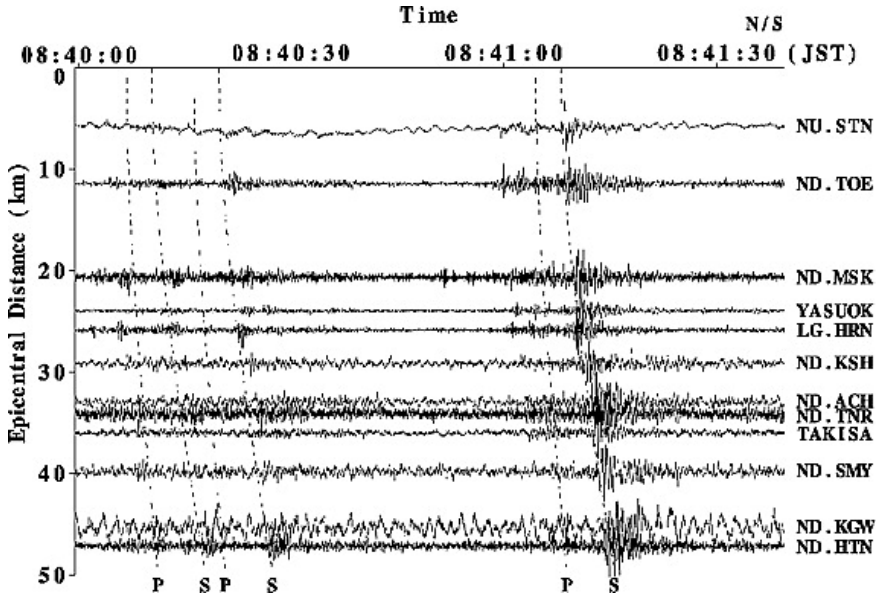

Figure 1.3: From Katsumata and Kamaya (2003). Example of low frequency tremor with estimated *P*- and *S*- arrivals.

The relationship between tremor and LFEs made it possible to locate the tremor accurately by identifying *P*- and *S*-waves in these signals (Shelly *et al.*, 2006; Ide *et al.*, 2007a), and quickly proved to be critical in understanding the genesis of tectonic tremor. Shelly *et al.* (2006) showed that LFEs correlate strongly with times of tremor and that they occur on the plate interface. Shelly *et al.* (2007b) showed that tremor consists of swarms of LFEs, and by inference occurred on the plate interface as well. Follow-up work by Ide *et al.* (2007a) demonstrated that LFEs and tremor occurred as shear slip and hence were part of a family of slow earthquakes (Ide *et al.*, 2007b) (Figure 1.4). This new family of events, including other types of signals such

as the very low frequency earthquakes (VLFEs), has a different physical behavior than regular earthquakes. For the slow earthquake family the seismic moment increases linearly with duration in contrast to and increase with the cube of duration observed for regular earthquakes, which further validates the difference between the two populations (Ide *et al.*, 2007b; Beroza and Ide, 2011).

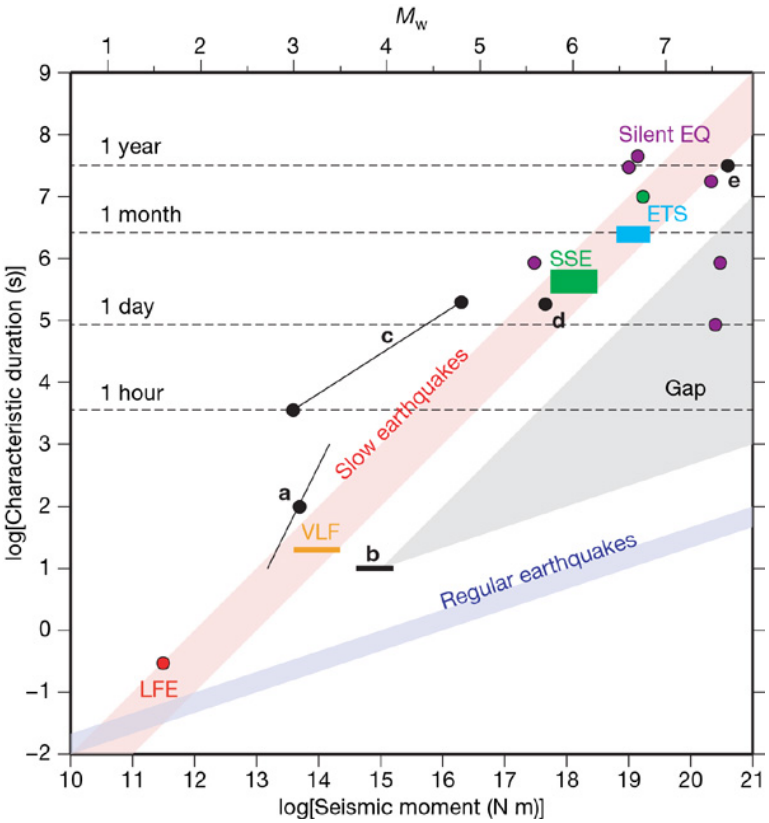

Figure 1.4: From Ide *et al.* (2007b). Scaling relationship for the family of slow earthquakes (SSE, ETS, LFEs, and VLFs) compared to regular earthquakes.

Given the relationship of LFEs to slow slip and tremor, once they were manually identified, several methods were developed to find these signals automatically. Initially, previously known LFEs were cataloged and used with a match filter technique by cross-correlating the signal of the LFE with tremor (Shelly *et al.*, 2007a; Shelly *et al.*, 2007b), Later, where there was no a priori knowledge of the LFEs, auto-correlation of all the tremor data was applied to find similar signals within

the tremor (Brown *et al.*, 2008). Lastly, for cases where the tremor location is already known, a beamforming method has been applied by calculating travel times of virtual LFEs and using these to search for them in continuous data (Frank and Shapiro, 2014).

LFEs have been found at many different areas where slow slip occurs, and in very different tectonic regimes such as Japan, Cascadia, Mexico, Costa Rica and the San Andreas Fault (Shelly *et al.*, 2006; Brown *et al.*, 2009; Shelly *et al.*, 2009; Walter *et al.*, 2011; Bostock *et al.*, 2012; Frank *et al.*, 2013) giving further insight into the processes related to slow slip.

To date, LFE detection methods, even though effective in finding similar waveforms, do not fully exploit the fact that LFEs repeat, with similar waveforms, not once, but multiple times. In Chapter 2, I develop a detection method that takes advantage of this repetitive nature of the LFEs by using a previously developed data-mining algorithm called PageRank. PageRank was originally developed for Google to give web pages a ranking of importance as a measure of how pages link to each other (Page *et al.*, 1999). I use this algorithm to find links within the seismic data and by doing so to find the frequently repeating LFEs. I test the method using data from the 2006 Shikoku, Japan slip event, to facilitate comparison with previous research of the same sequence. I create an LFE template and use it to find more LFEs within the data. With the new template I find detections previously found as well as many new LFEs during the SSE that were previously missed. I also show that the PageRank algorithm can be used as a tremor detector, for places were tremor is not known to exist or is hard to observe.

In Chapter 3, I apply the now validated detection method to tremor from northern New Zealand. In New Zealand, it has been shown that tremor, in relation to slow slip, is very difficult to observe. Because of this, I focus on the 2010 Gisborne SSE that has small tremor bursts associated to it. I apply the PageRank algorithm to several tremor bursts from the 2010 Gisborne slow slip event to study the occurrence of tremor and to

see if LFEs are present within the tremor. I find a repeating signal within the tremor and create an LFE template to search through the entire event. I find LFE detections during the short tremor bursts but also find frequent detections outside of the tremor signal.

Another area that I have focused on is Taiwan. Here, tremor has been found to occur both when triggered by surface waves, as spontaneously, in the absence of triggering. In Chapter 4, I compare the signal between the triggered and ambient tremor from southern Taiwan. I apply the PageRank algorithm to data from both triggered and ambient tremor and create an LFE template for both. The templates for both data sets are very similar and I test this similarity by interchanging the template by using the template from ambient tremor on triggered tremor and vice versa. Both templates work well in detecting the LFEs within the signal.

In the final chapter of my thesis I use tremor as a source of seismic waves, and focus on a particular use for the tremor signal itself. Baltay and Beroza (2013) used data from the Cascadia subduction zone to show that tremor can be used to estimate attenuation parameters in places where there is not enough background earthquake data to establish reliable ground motion prediction relations. Cascadia is a great example of this, where background seismicity is very sparse, but tremor activity is abundant. In Chapter 5, I use the attenuation results from Baltay and Beroza (2013) calculated from tremor during three different slow slip events to map the magnitude and scale-length of ground motion attenuation variability across the northern Cascadia subduction zone.

CHAPTER 2

PageRank for Earthquakes: An Application to Low Frequency Earthquake Detection

In this study we take advantage of the similarity of Low Frequency Earthquakes (LFEs) within tremor by developing a test of significance that explicitly accounts for short-time correlations in the data, and the likelihood that the sources repeat more than once. To do this, we use the structure of how similar windowed waveforms are linked with one another. A complicating factor is that these links don't form closed loops that satisfy closure, but have links that may be incomplete. Despite this lack of closure, we would like to take full advantage of the structure of similar seismograms. Our problem maps very closely to one that has been solved previously. One of the initial web page searching algorithms implemented by Google used the links between pages to calculate the quality of a document. This data mining algorithm is known as PageRank and was developed by Page *et al.* (1999). If we relate this to our problem, but substitute candidate windows in place of web pages, and we know that these windows are linked to one another, we can use the PageRank algorithm to rank them by the number of times they are linked. In applying PageRank to tremor data, we find the ranking of a specific window and show statistically how windows rank relative to each other. This identifies those windows that are most likely to be LFEs, and can be used to construct templates through waveform stacking. These stacks provide high signal to noise ratio (*snr*) templates that can be used to find other LFEs.

We use the April 2006 Shikoku, Japan tremor episode to test our method due to the wealth of available information concerning tremor in this area (Obara, 2002; Shelly *et al.*, 2006; Shelly *et al.*, 2007b; Ide, 2010) and this specific tremor episode

has been analyzed in great detail (Shelly *et al.*, 2007a). By applying the PageRank approach we create robust LFE templates that match known LFEs from the Japan Meteorological Agency (JMA) catalog. Using these templates we find detections in data for the April episode with similar results to Shelly *et al.* (2007a) for the same time periods. We also find detections for weaker segments of tremor that were not previously reported. Our approach suggests a new approach to differentiate tremor signals from noise for sparse data sets using the fact that PageRank behavior is qualitatively different for tremor vs. noise.

2.1 Multiplicity of Repeats

Non-volcanic tremor has been shown to be formed by swarms of LFEs, and these swarms explain most of the tremor. These swarms occur as many of the LFEs repeat many times within short time periods. Shelly *et al.* (2007b) first showed this using data from a 2005 slow slip event in Japan. We can see this in Figure 2.1, where the LFEs (red traces) occur during most of the 30 minutes of tremor.

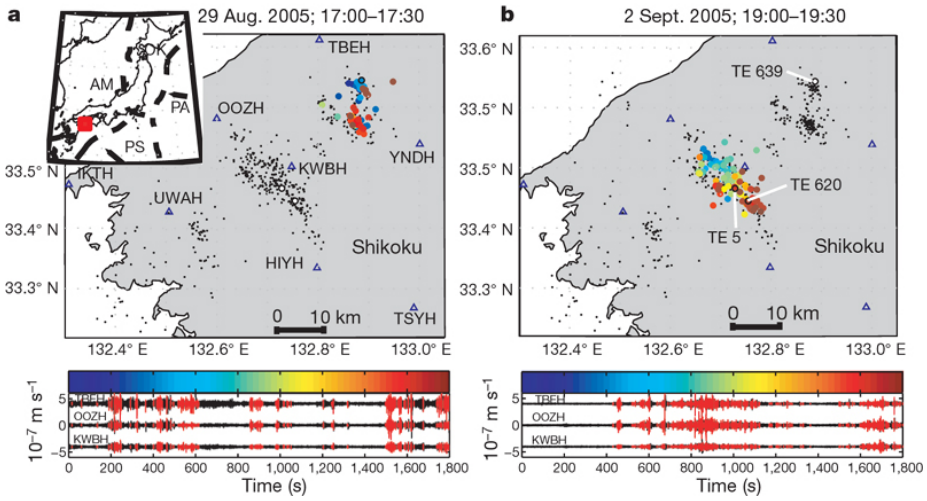

Figure 2.1: Figure from Shelly *et al.* (2007b) Example of LFEs within tremor a) for a 30-min period on 29 August 2005 showing areas active (colored circles). Black dots show epicenters for LFEs used in their study. Red indicates times with a detected event. b) Same as a, but for 2 September 2005.

Brown *et al.* (2009) also showed that tremor in Cascadia and Costa Rica, as well as Japan is formed by many LFEs and found large numbers of repeating detections in these three locations. These studies show how LFEs repeat many times but do not fully exploit this repetitive nature. We want to take advantage of this knowledge and incorporate it into our detection scheme in the following manner.

To find LFEs within the tremor data, we begin with the autocorrelation method of Brown *et al.* (2008), which detects potential LFEs in a pair-wise manner. This method finds the signals by correlating each window with all other windows in time during a tremor segment of interest. We divide the tremor data in 10 s windows lagged by 0.08 s or 2 samples for data with 25 samples per second. This creates a population of 44,900 windows for 1 hour of data. The population of values for the correlation coefficients (CC) between these windows closely follows a normal distribution (Figure 1). We have applied the Fisher transformation to the CC values, where $z = \frac{1}{2}\left[\ln(1+\mathrm{CC}) - \ln(1-\mathrm{CC})\right]$. This transformation accounts for the fact that the distributed values cut off at CC = ±1. After applying this transformation, we can assume normal statistics for the distribution of the CC values. We find that in our case the transformation made no significant difference in the distribution, due to the small values of CC (Fisher, 1973). For this reason, we base our detection threshold on a normal distribution with zero mean and focus on the large positive values to declare a positive detection. For a normal distribution, σ = 1.253 x mean absolute deviation (MAD). MAD is the mean of the absolute deviations of a set of data about the data's mean and is a measure that is chosen to be insensitive to outliers. Our objective is to find the positive outliers in the data, which represent the repeating signals within the tremor. Because the MAD will not be affected by a limited population of outliers it should not bias our estimate of σ, so we can use this as a measure to establish a threshold of detection. By assuming zero mean (Figure 2.2), we can calculate the MAD directly from the population of CC values and estimate σ from this. Here we have chosen to use the mean instead of the median, which has been preferred in previous analyses (Shelly *et al.*, 2006; Brown *et al.*, 2008). Our expectation is that

both the mean and the median cross correlation of signals will tend to zero in the absence of correlated signals.

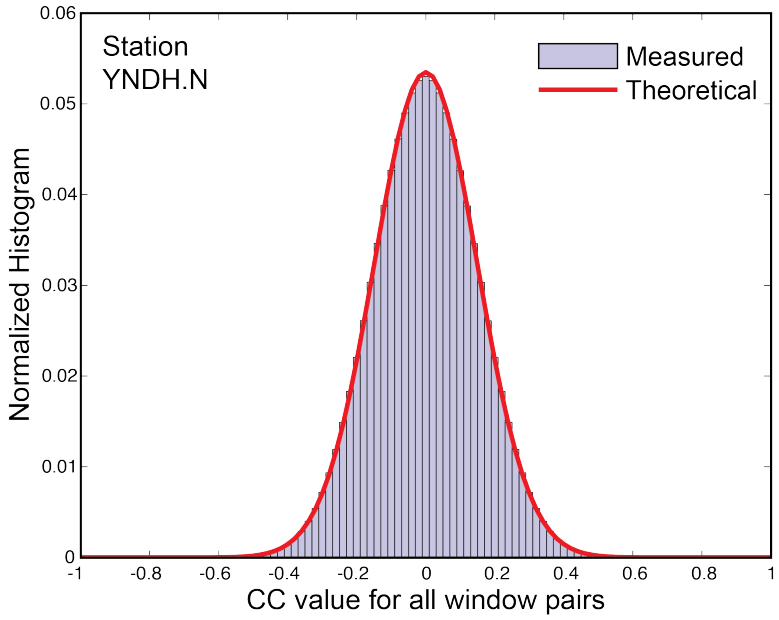

Figure 2.2: Distribution of CC values for all window pairs of 1 hour of tremor data on station YNDH.N. Black line represents the theoretical normal distribution calculated using σ = 1.253 x MAD. Here MAD is computed from all window pairs.

We found that for a very large set of window pairs the computational costs of calculating the median are substantial whereas the mean is easily computed. With this, we perform the autocorrelation to find detection pairs for each of the stations analyzed with a low positive threshold of 3σ, which corresponds to a two-sided significance level of 99.7%. This level, which we use to define a positive correlation, is a trade-off between a higher threshold, which will provide more confident matches at the cost of fewer positives for low *snr* data, and a lower threshold, which will provide more positives, but with less confidence in the reliability of individual matches. The noise level, and therefore the statistical behavior of the autocorrelations, varies between stations so we perform the analysis one station at a time.

Finding detection pairs within the tremor data does not ensure closure because LFEs repeat multiple times during a single tremor episode (Shelly *et al.*, 2007b) and the *snr* is low. Figure 2.3 shows this lack of closure schematically. Window A correlates significantly with Window B and Window D. Later in time, Window B

matches with Window C, but Window A does not match with Window C, and Window B does not match with Window D. Such a lack of closure is inevitable with low *snr* signals, and complicates detection statistics, yet we have to make full use of the information we have. That is, we want to use all the links, and the complex hierarchical relationships they express, to identify the windows most likely to represent LFE signals.

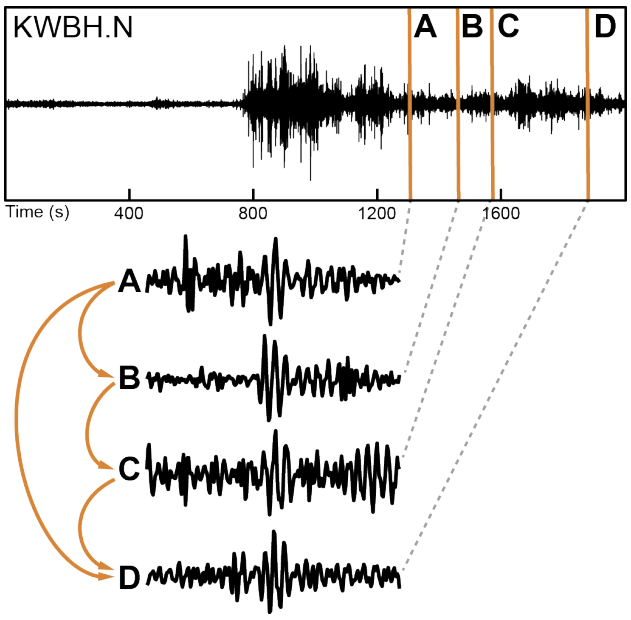

Figure 2.3: Window pair links: A, B, C, and D are windows that were found to be a match with another window given the threshold selected. This figure shows how all these pairs are linked together. Some windows are linked directly: A → B and B → C. Other windows are linked indirectly: A is linked indirectly to C (since B → C) and B is indirectly linked to D (since C → D).

We use a tool developed for data mining to address this problem. Specifically we apply the PageRank algorithm (Page *et al.*, 1999) to the detection pairs from the autocorrelation process to determine which windows have the most number of links. We then calculate a ranking for each window and if the probability is high, this suggests a robust LFE detection for that window within the data.

2.2 The PageRank Approach

The PageRank method calculates the probability of importance of each web page in a set of web pages, assembled in a vector. These probabilities are based on the

number of links each web page has, assigning a high probability to web pages with a high number of links and low probability to pages with a low number of links. Specifically, each of the elements of this vector is the probability that a "random surfer" will visit a particular page on the web (Page *et al.*, 1999; Moler, 2011). Like a Markov Chain, PageRank is a random, iterative method where the probability at one stage in the iterations is computed from the previous stage, with an initial condition of equal probabilities for all pages. For our problem of seismic data, we form a connectivity matrix $\mathbf{G}$ from the detection pairs found during the autocorrelation that contains all the information on links between all windows. If we find a match between window *i* and window *j* in time, then $g_{ij} = 1$, otherwise $g_{ij} = 0$. Now, if we consider p to be the probability of the random walk following a specific link to a window, and the probability of an arbitrary window to be chosen as $1 - p$, then the probability that a certain random window is chosen will be $\delta = (1 - p)/n$, where n is the total number of windows. With this, we form a matrix $\mathbf{A}$ that scales the $\mathbf{G}$ matrix by the sum of its columns:

$$a_{ij} = \begin{cases} pg_{ij}/c_j + \delta : \; c_j \neq o \\ 1/n : \; c_j = o \end{cases} \tag{1}$$

where $c_j = \sum_i g_{ij}$ and $\mathbf{A}$ is the transition probability matrix (Moler, 2011). We then solve equation (2) iteratively to find the PageRank:

$$\mathbf{x} = \mathbf{A}\mathbf{x} \tag{2}$$

This equation has a unique, nonzero solution if a scaling factor is chosen such that $\sum_i x_i = 1$. Given this condition, $\mathbf{x}$ is the steady state vector of $\mathbf{A}$ and therefore the PageRank (Moler, 2011).

As a starting point, we assign equal probabilities to each window of $1/n$ and then iterate equation (2) until **x** converges to a desired tolerance. Here, we have selected a standard value of $p = 0.85$ and a tolerance of 0.01 to calculate the PageRank for each window in the tremor analysis. As we iterate, we calculate the 1-norm between the probabilities of the previous and current iteration to estimate the tolerance. If it is below $0.01/n$, we stop the iteration and use that **x** for PageRank.

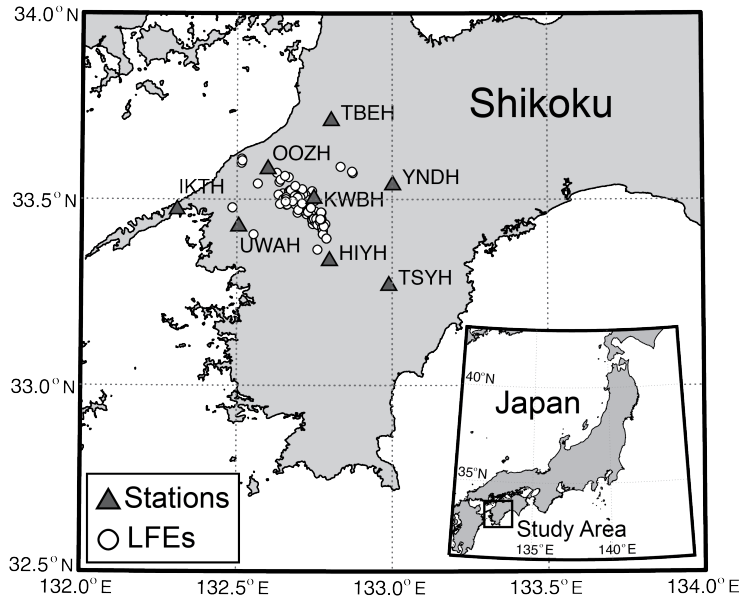

Figure 2.4: Map of Shikoku, Japan with the location of stations (dark gray triangles) used in our analysis. Circles represent LFE locations from Shelly *et al.* (2007a) during the tremor episode of April 16, 2006. Inset map shows the location of the study area in Japan.

To test our method, we use data from 8 stations in Shikoku Japan (Figure 2.4) during the April 2006 tremor event. This group of stations was selected due to the locations of a large number of well-studied LFEs that have occurred within this area (Shelly *et al.*, 2007a). We analyzed 1 hour of data at 25 samples per second from April 16, 2006, where a large number of LFEs have been previously detected using templates (Shelly *et al.*, 2007a). We chose a time period where the tremor signal is small at the beginning and increases in amplitude towards the end (Figure 2.5) to understand differences in the behavior of PageRank. Using these data, we first calculated the autocorrelations using the population of 44,900 windows created from the 10 sec windows lagged by 2 samples. We then applied the PageRank approach to

the detection pairs to find the probabilities for each window. Figure 2.5 shows the PageRank values for each window in one hour of Japan data for several stations.

Once we have computed the PageRank for each window, we know which windows have the highest probabilities of being repeating signals, and are the most likely to be LFE waveforms. A large PageRank value here signifies a window with a large number of links to other windows, both direct and indirect. Figure 2.5 shows that the PageRank values get higher as the tremor amplitude increases for all three stations shown. It is also noteworthy that there are high values towards the beginning where tremor amplitude is smaller. This may reflect the initial stages of tremor where there are not enough LFEs active to generate a large amplitude tremor burst.

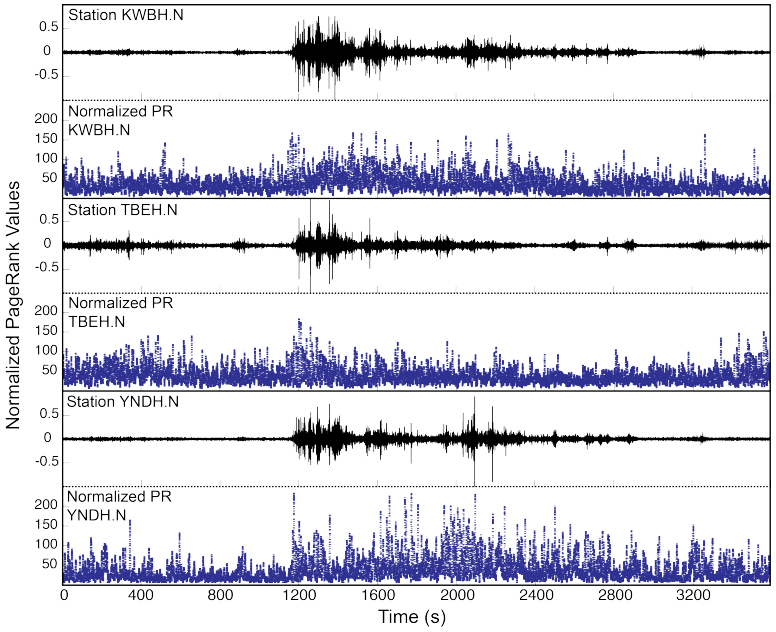

Figure 2.5: One hour of tremor data (black) during the tremor event in Shikoku, Japan, on April 16, 2006 for stations KWBH, TBEH, and YNDH associated to its PageRank values (blue). The PageRank values are normalized by the total number of windows analyzed.

We use the windows with the highest PageRank values to create template signals by stacking the matched windows. To exploit the multiplicity of the LFEs, we use both the direct and indirect matches of the high ranked windows (Figure 2.5) to create the stack for the template LFE. Figure 2.6 shows a stack with all the windows that were found to be a match to a window with a high number of matches for station YNDH.N during the one hour of tremor data analyzed. On the left, the stacked signal

(Figure 2.6a) is formed by windows with direct links only. On the right (Figure 2.6b), the stacked signal includes windows from both direct and indirect links to the window with high PageRank.

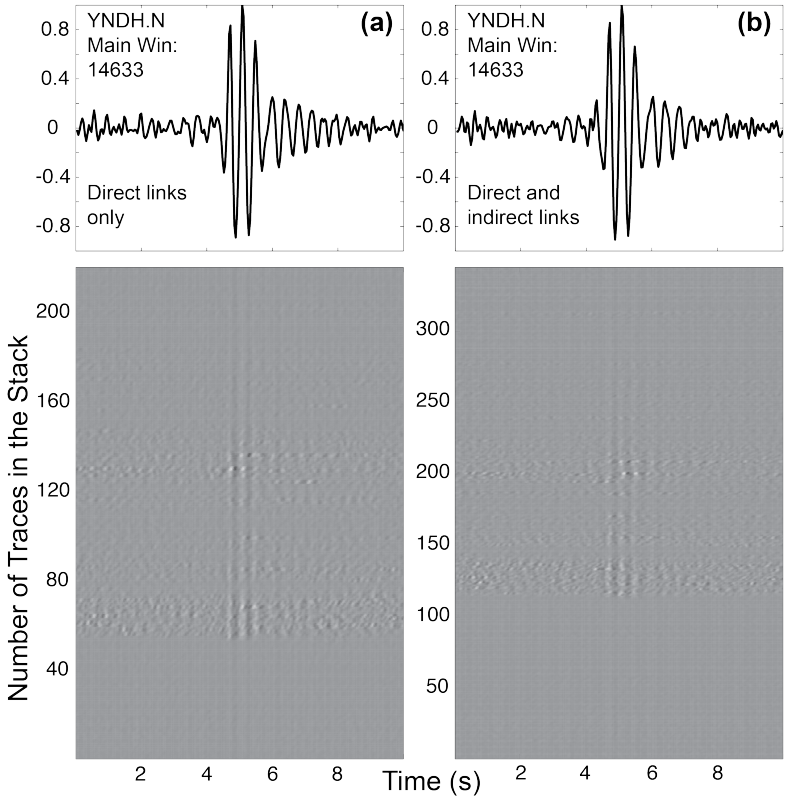

Figure 2.6: Stacked signal (top) formed by summing all the windows (a) using only windows with direct links (221 traces) and (b) using windows with direct and indirect links (345 traces) that were found as a match to the window with highest PageRank. Grayscale plot (bottom) of each one of the windows forming the stack.

We form the template from both the windows that directly match the main window, and also all the windows that match each one of those initial matches. These are the windows with indirect links to the main window. The advantage of this process can be seen in Figure 2.7, which shows a comparison between the first, second and third level stacks for several stations used in the analysis. The signal of the stacked waveform improves significantly once a second level of detections is added to the stack (windows with indirect links). The difference is apparent from Level 1 to Level 2 (Figure 2.7), where each signal has less noise around the main peak of the largest amplitude arrival

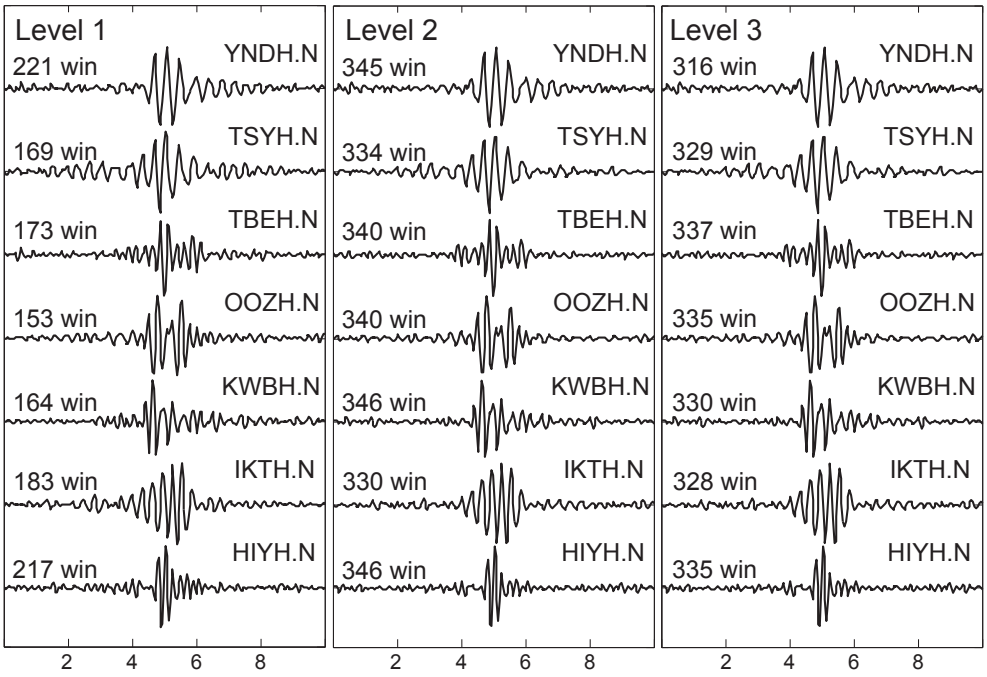

Figure 2.7: Plot of stacked signals formed by windows of three different levels of links. Level 1 shows stacks created using only the windows with direct links to the window with highest PageRank. Level 2 shows stacks created with windows with direct links and one level of indirect windows (windows matched to the matches of the main window). Level 3 plot shows the stacks created with direct windows and two levels of indirect windows. The number on the left of each plot shows the number of traces that were used to create each stack.

Here, each level of stack was created with a different number of windows. In the case of Level 1, the lowest number of windows was used because these stacks only include the windows with direct links to the highest ranked window. Each window from the direct links has its own set of links. These would be the first level of windows with indirect links to the main window. Level 2 has a larger number of stacks than Level 1 because it also includes these windows, the first level of windows with indirect links. Adding these windows to each stack improves the signal for each template (Figure 2.7).

We can add another level of links by stacking the windows with links to the first level of windows with indirect links. These stacks are shown in Figure 2.7 as

Level 3. We can see that adding one more level of windows does not change the stack significantly and the number of signals used is very similar to Level 2. The reason for this is that the windows added at this step are mostly windows that were already present as links to other windows. For that reason they do not contribute independent information to the stack. We note here that in some cases the number of windows used for Level 3 is slightly lower than in Level 2. This is caused by the way we have defined the near repeat window elimination in the processing. As we scan the list of windows, we eliminate the near repeats by finding the window that was paired with the best CC value. We do this in ascending numerical order for a 3 second time span. If the window with the highest CC was not the first on that group then this pushes the selected window number forward. These might cause the next group of windows to be considered now as a near repeat if the window number of the first of the group is now less than 3 seconds than the previously selected one. Adding one more level of windows only finds more similar windows to the signals used in Level 2 and some of these might fill some small gaps in, causing a few more near repeats to be eliminated. Given the similarity of the stacks from Level 2 and Level 3 (Figure 2.7), this suggests that it is only necessary to create the stacks using one level of windows with indirect links to get an optimum result for creating a template waveform.

We validate the templates created with these stacks by comparing the stacked signals to known LFEs from the JMA catalog. We selected various events from the catalog that locate in the same general area as the LFEs reported for the April 2006 sequence (Shelly *et al.*, 2007a). Figure 2.8 shows the waveform comparison between the LFEs from the JMA catalog and the templates created in this study for the stations available in the catalog. The stacks created for the five stations, shown in Figure 2.8, match the three different events from the catalog and preserve the move-out across the network.

A potentially significant advantage to the PageRank approach is that it can also be used to distinguish between tremor and noise. We compared an hour of tremor data

from the April 16, 2006 episode to an hour of noise data for the same stations in Shikoku. Figure 2.8 shows the differences between the normalized PageRank histograms for three different stations used in this analysis. These histograms are significantly different between tremor and noise because tremor has many more windows with high PageRank.

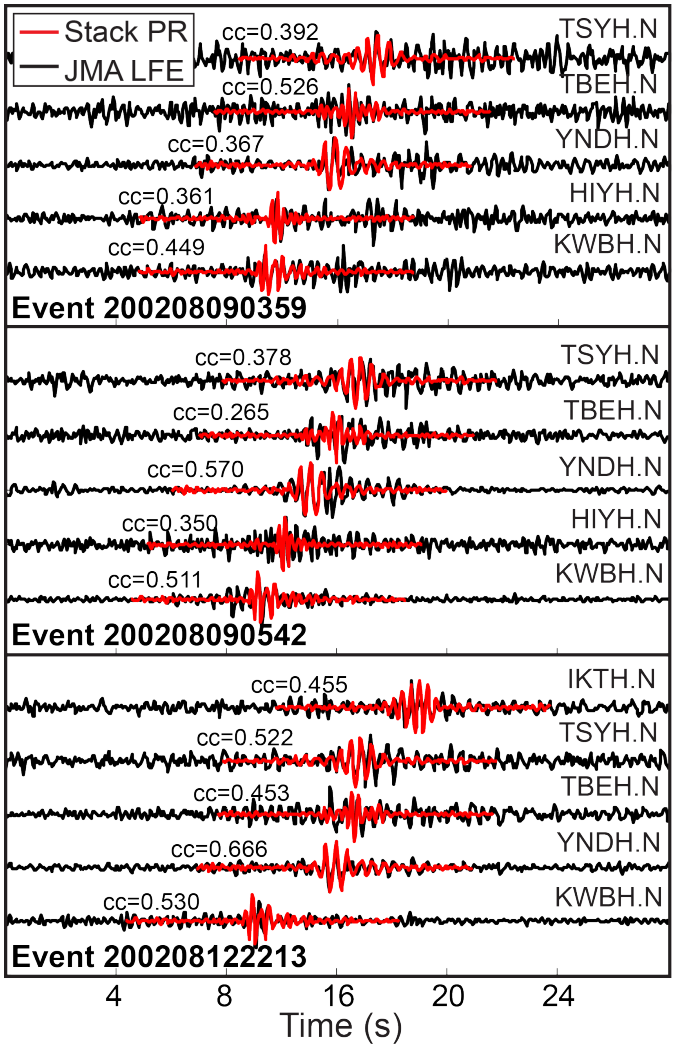

Figure 2.8: Three different LFEs from the JMA catalog (black) compared with one template stack (red) created using the PageRank approach from an hour of April 16, 2006 of Shikoku tremor data.

If the data has a lower *snr*, then this characteristic of PageRank could be used to help distinguish tremor from noise. Because the differences show up in single-components at different stations independently, it should also help to distinguish tremor from noise for sparse data.

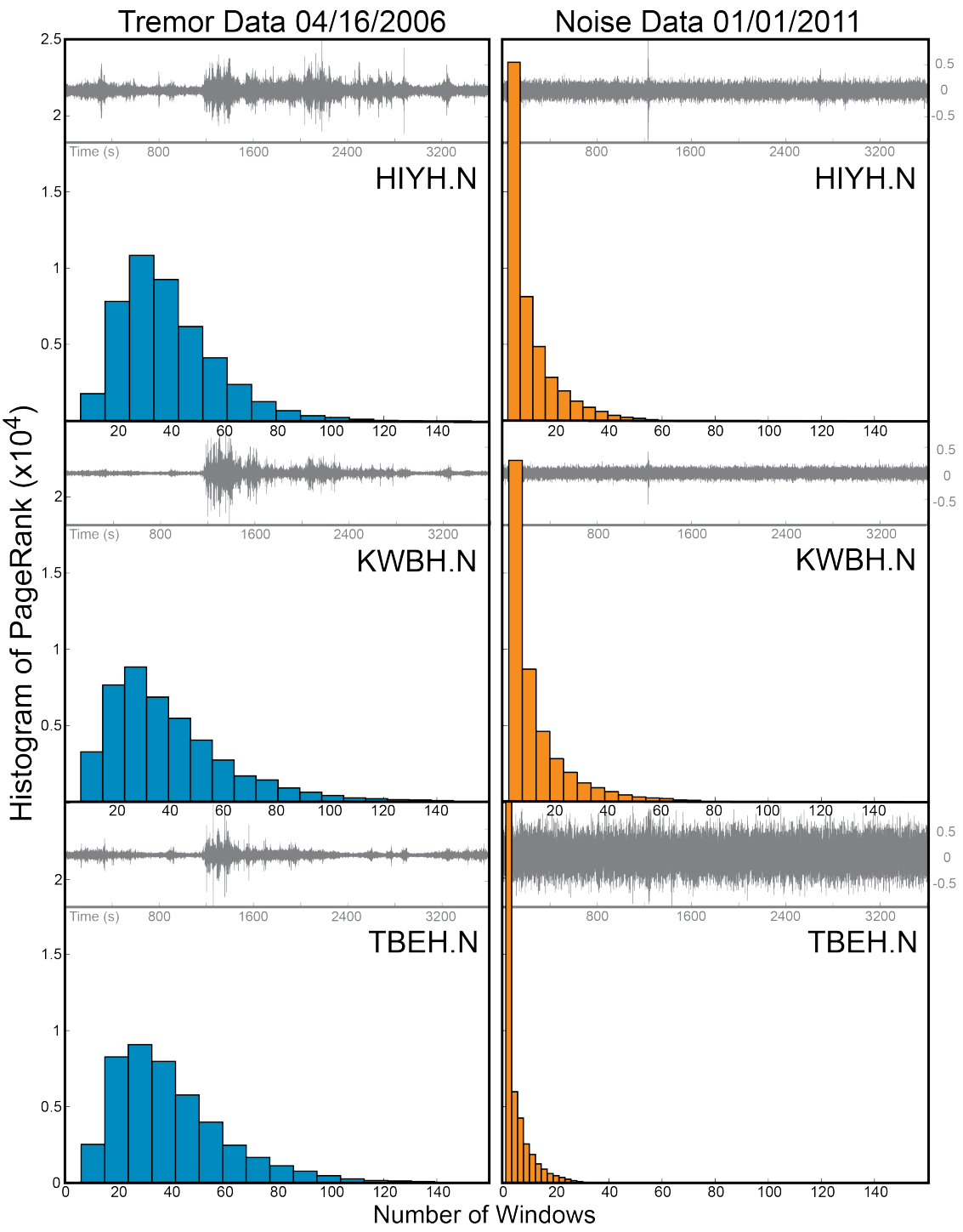

Figure 2.9: Histograms of normalized PageRank values for tremor data (left) and noise data (right) for three different stations used in the analysis. Noise data shows large numbers of low PageRank values whereas the tremor data have higher PageRank values.

2.3 Application to Continuous Data: South West Japan

Having found robust signals to use as LFE templates, we applied these to search through continuous data during the Shikoku event in April of 2006. We picked data where it is clear that the strong tremor episode is getting started, so we can observe small tremor bursts but also larger amplitude, more significant bursts (Figure 2.10) to test the ability of our detector to find LFEs within lower *snr* tremor data. We cross-correlate the templates with 10 second windows and move the window every 2 samples through the data to find matches. We perform this analysis one station at a time using a low threshold (3σ) and later compare the results between stations to distinguish between true and false detections.

Figure 2.10 shows the second half of April 16, 2006 for Shikoku Hi-Net data. This data set shows small tremor bursts between 12,000 and 24,000 seconds and larger amplitude tremor bursts towards the end of the day, around 32,000 seconds. Here we used only stations were it was possible to compare our LFE template to LFE picks present in the JMA catalog (Figure 2.8). To associate detections found for each station (Figure 2.10a), we compare all stations within a 2-s window and declare a positive detection if three or more of the stations show detections within those 2 seconds. Using this simple association algorithm we find very similar results to Shelly *et al.* (2007a), particularly for the stronger tremor burst towards the end of April 16, 2006. We also find a large number of detections that were missed previously, during smaller tremor bursts (Figure 2.10b) between 12,000 and 24,000 seconds and between 32,000 and 36,000 seconds.

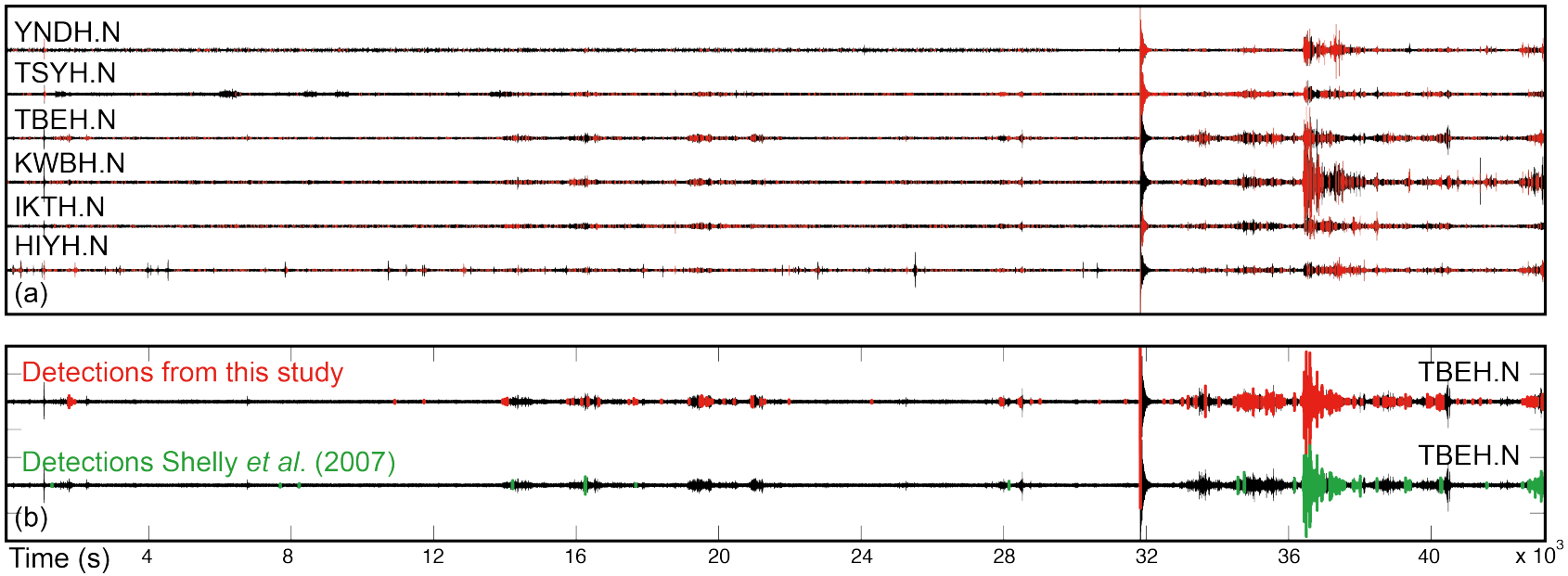

Figure 2.10: Half day of data during April 16, 2006 of several stations in Shikoku showing the beginning of the tremor episode. (a) Detections (black) found individually for each station using the stack created with the PageRank approach for 6 of the stations in the analysis. (b) Detections found on at least three of the stations within a 2 s window (top), compared to Shelly *et al.* (2007a) detections (bottom) using template matching.

2.4 Discussion and Conclusions

We use the PageRank approach to detect LFEs during the April, 2006 tremor episode in Shikoku Japan. We selected this data set to facilitate the comparison of results with Shelly *et al.* (2007a) to test our method's ability to detect LFEs within data with both high and low *snr*. Analyzing one station at a time, and applying low initial detection thresholds, we created robust LFE templates that match real LFE signals from the JMA catalog for this tremor episode without the use of any previous knowledge of event times. These templates include windows with both direct and indirect links to the highest PageRank window, which improves the *snr* of the template created for each station. These templates will facilitate the detection of other events within the data.

We cross-correlated the stacks we developed using the PageRank approach to find other LFEs within the April 2006 tremor episode in Shikoku, Japan. We find that our detections are comparable to detections found by Shelly *et al.* (2007a) where the tremor burst has large amplitudes compared to the rest of the time. We also find a number of detections within smaller tremor bursts that were previously missed. This suggests that the PageRank approach is a good tool for finding LFEs within lower *snr* data.

We have also found that the PageRank distribution differs between tremor and noise. By looking at histograms of PageRank values we can differentiate between tremor and noise because unlike noise, tremor data has large numbers of high PageRank values due to the significant links between windows within a short period of time. This could prove to be a useful tool for automated tremor detection and for detecting tremor where it has not been detected previously, or where it has been found but the signal is not as prominent as it is on Hi-Net data. Finally, although we have applied it to detect LFEs within tremor, the PageRank approach may be useful for

other situations such as swarms or aftershock sequences, for which many similar waveforms may be present.

Aguiar, A. C, and G. C. Beroza (2014) PageRank for earthquakes. *Seismological Research Letters*, Volume **85**, Number 2, p. 344-350, doi: 10.1785/0220130162.

CHAPTER 3

Low Frequency Earthquake Detection in Northern New Zealand

The North Island of New Zealand lies on the Hikurangi subduction zone, where the Pacific plate subducts under the Australian plate. Here the plate motion is accommodated by a complex forearc clockwise rotation that includes dextral strike slip on the upper plate, with convergence rates that range between 60 mm/yr and 20 mm/yr north to south (Wallace *et al.*, 2004; Wallace and Beavan, 2010).

The Hikurangi subduction zone is another region were slow slip has been observed on the transition between the locked section of the fault and the aseismic creeping section (Douglas *et al.*, 2005; Wallace and Beavan, 2006; 2010). The duration of slow slip episodes observed in this area ranges from a few days to a year or more (Wallace and Beavan, 2010). Here, slow slip was initially identified without any visible tectonic tremor associated with it, although some microseismicity occurred coincident with the time of slow slip during the 2004 Gisborne event (Delahaye *et al.*, 2009). Deep tremor bursts were later identified by Fry *et al.* (2011) in the central North Island, triggered by the 2010 Mw 8.8 Chile earthquake; as were small tremor bursts, lasting just a few minutes, during the 2010 Gisborne slow slip event (Kim *et al.*, 2011) suggesting that tremor may be difficult to observe due to a combination of strong attenuation and limited seismic station coverage. Another important aspect of the Hikurangi subduction zone is that slow slip seems to occur at a variety of scales, and much of the slow slip locates offshore of the North Island (Wallace and Beavan, 2010). This adds to the difficulty of detecting tremor associated with slow slip in this region.

The March/April 2010 Gisborne slow slip event was equivalent to a Mw 6.7 event, that occurred just offshore, and lasted for about 16 days (Wallace and Beavan, 2010). Because of the difficulty of observing tremor during the 2010 Gisborne event, as well as a suggestion of recognizable *S* waves within the tremor reported by Kim *et al.* (2011) showing LFEs within the signal, we have selected this area to apply the PageRank algorithm for detecting multiple repeats of the same waveform signature. We searched for repeating signals during the known tremor bursts in March of 2010 reported by Kim *et al.* (2011). We also explored the possibility of detecting tremor outside of those times, given that not a lot of tremor has been reported for this event during the 2 weeks of slip. We analyzed this data set following the LFE detection method described in Chapter 2.

3.1 PageRank applied to New Zealand data

To analyze the tremor bursts during the 2010 Gisborne slow slip event, we selected data from GeoNET, New Zealand's geological hazard monitoring system. Many stations were available during the time period of this event, but only 5 stations show the tremor clearly. These are the 5 stations shown in Figure 3.1. Four of these stations are short period stations (CNGZ, MHGZ, PRGZ and RIGZ) and one is a broadband station (MWZ). We used all three components for all stations in the analysis.

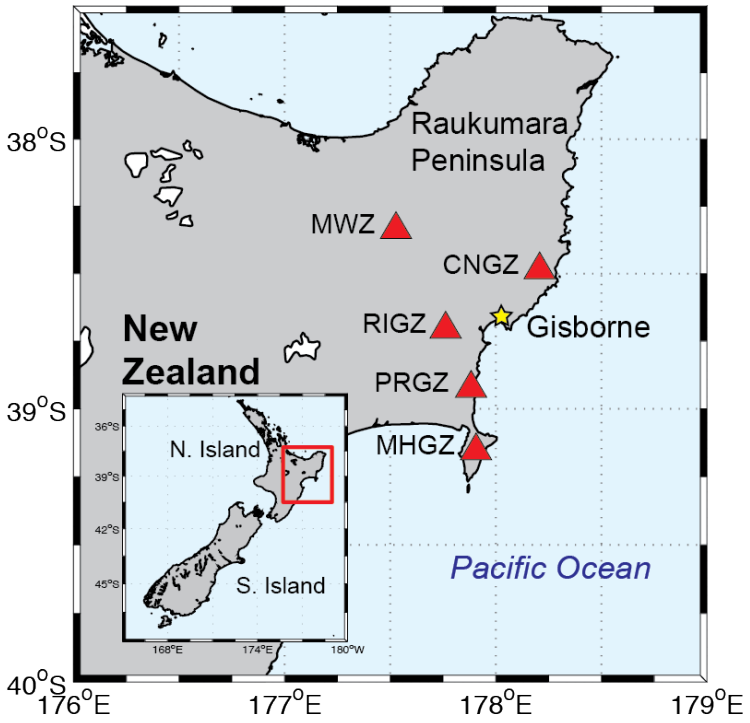

Figure 3.1: Map of the northern section of the North Island, New Zealand. Red triangles show the stations used in the analysis. Red box shows the study area.

The observed tremor bursts during this slip event are only a few minutes long, which is much shorter than tremor from other regions where tremor signals can persist for hours. We analyzed two 30-minute sections of data, each containing one of the most clear small tremor bursts found by Kim *et al.* (2011). These tremor bursts are 8 days apart. The first set is on March 21, 2010, the second on March 29, 2010, and both are about 3 minutes long. We analyze these data using the PageRank algorithm, as described in Chapter 2, to search for a repeating signal within the small tremor bursts. For this analysis, the data from the 5 stations (Figure 3.1) were filtered between 2-4 Hz, the frequency band over which tremor is best observed in this area. This is a narrower frequency band than what has been used before in other areas, where a wider band of 1-8 Hz has been used. But similar to the narrow frequency band where tremor is observed in Guerrero, Mexico (1-2 Hz) (Payero *et al.*, 2008; Frank *et al.*, 2013; Frank and Shapiro, 2014).

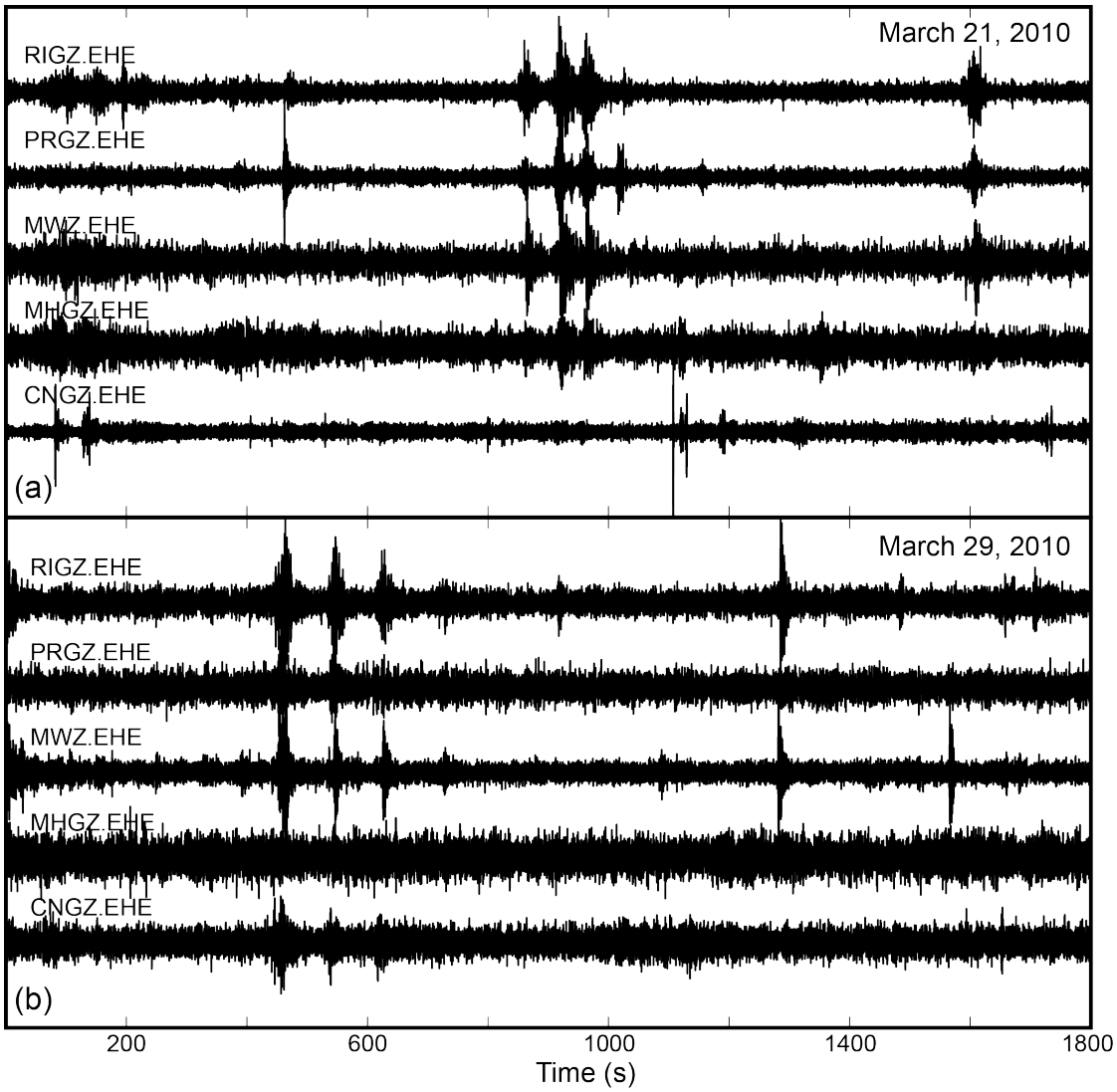

Figure 3.2: Plots of data used in the analysis. (a) 30 minutes of data during March 21, 2010 containing the tremor burst found that day. (b) 30 minutes of data with tremor during March 29, 2010.

After filtering, the data were divided into 8 s windows lagged by 0.08 s to perform the initial autocorrelations and prepare for the PageRank analysis. We used the highest PageRank window found with this method to find a repeating signal for each of the two tremor bursts analyzed individually, and compare the signal from each data set.

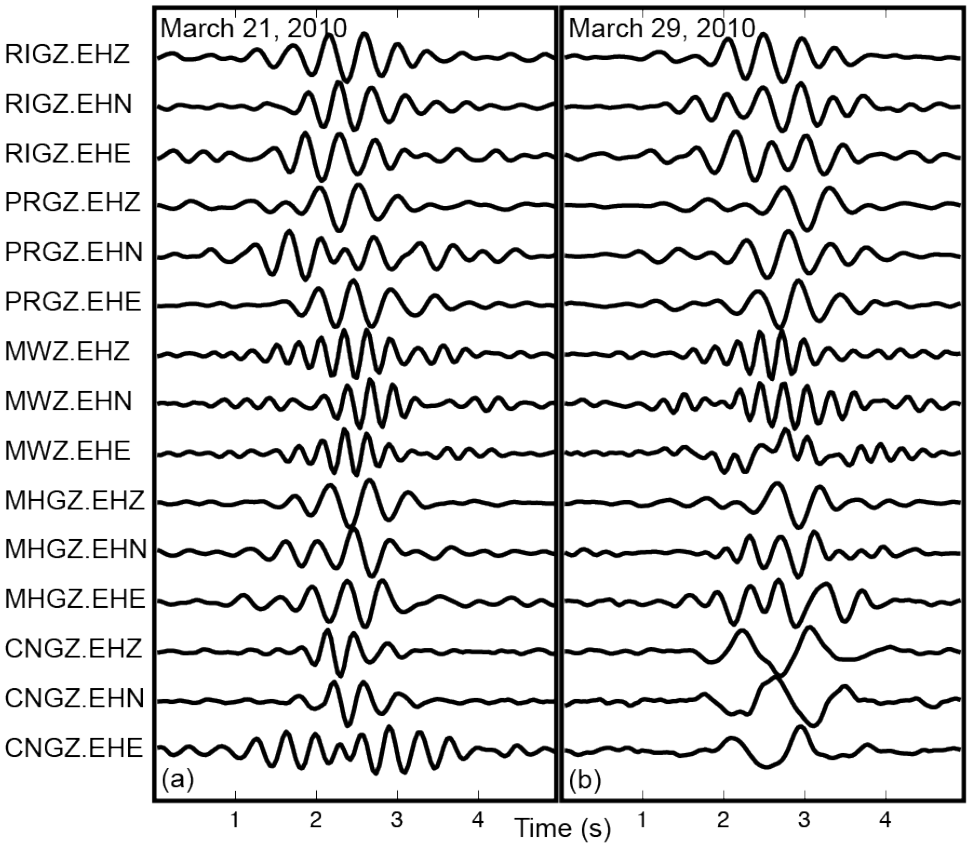

Figure 3.3: Plots of the template created for each data set (a) LFE template for data during March 21, 2010, (b) LFE template for data with tremor during March 29, 2010.

The LFE templates created for each data set (Figure 3.3) show a very similar signal. To test this similarity, we used each template interchangeably, that is, we use the LFE template created for one data set to detect LFEs in the second data set and the template created from the second data set to detect repeating LFEs in the first data set. For this analysis we used the same two 30-minute tremor data sets shown in Figure 3.2. We also cross-correlated each template with its counterpart to find a measure of similarity and all stations except one (CNGZ) show a CC value higher than 0.5 suggesting high similarity between the two. Figure 3.4 shows this similarity, with the template created from data during March 21 shown in red, and the template created from data during March 29 shown in black for all components.

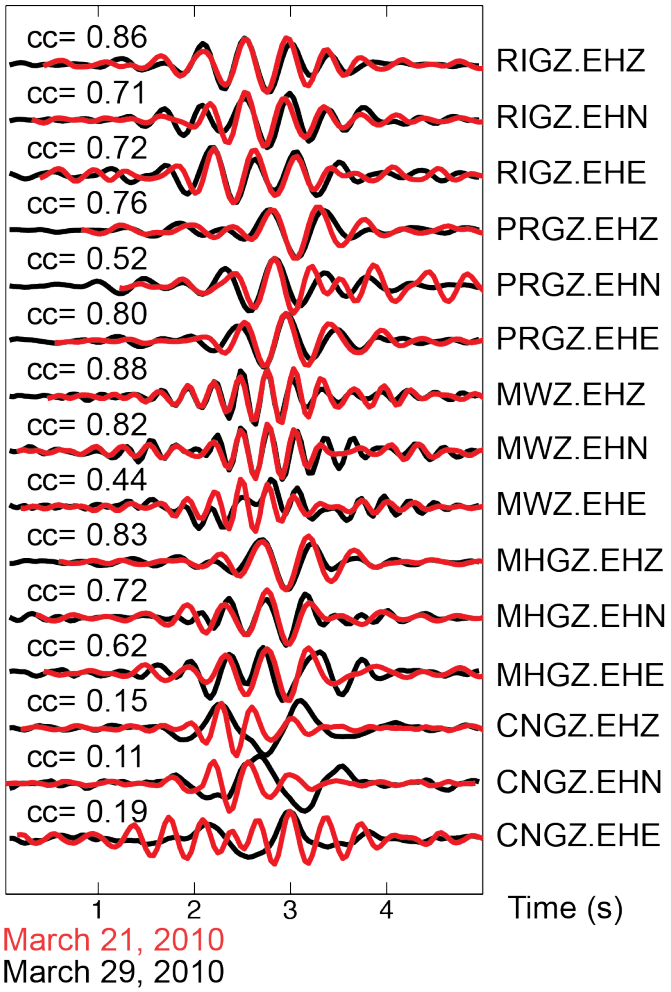

Figure 3.4: Comparison of the template derived independently from each data set. Red is the template for data with tremor during March 21, and black is the LFE template for data with tremor during March 29, 2010.

After comparing both signals, we selected the LFE template created from the tremor data during March 21, 2010 to detect other LFEs within the data, given that station CNGZ seems to show a template for each of the three components that is more consistent with the frequency content of the signal that is observed at other stations compared to the result from the March 29, 2010. For that episode, this template seems to show a longer period than any of the other stations, which could be due to a repeating local noise source at the time of that record.

To validate the existence of a repeating signal within this data set, we have compared the tremor data to noise data during a different time period where no signals are evident (Figure 3.5). For the same set of stations, we created histograms of the PageRank values for both the tremor data and the noise data to see if these histograms differ, as we have shown to be the case for the Japan data in the previous chapter (Figure 2.9).

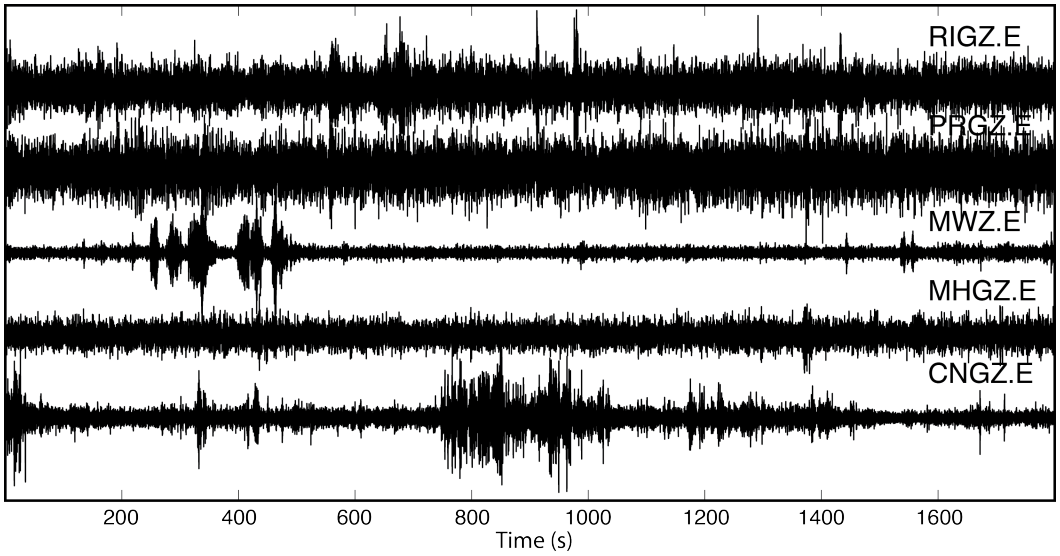

Figure 3.5: Noise data during March 19, 2010 for the same set of stations used in the PageRank analysis of tectonic tremor.

Here, we repeat the analysis using the PageRank algorithm on the noise data and calculate histograms for the normalized PageRank values to compare with histograms of PageRank values from the tremor data analysis. We can see in Figure 3.6 that, for Northern New Zealand, the histograms of normalized PageRank values for noise data differ from the histograms calculated from the tremor data in that there are more values with a larger number of similar windows than in noise data, where fewer similar windows are present, weighting the distribution towards small values. Although the difference between the noise and tremor histograms is more subtle than what was shown for the Japan study in Chapter 2 (Figure 2.9), this is not surprising

given that the tremor bursts observed for this slow slip event have very short durations, unlike in Japan, and possibly weaker or less similar repeating signals as well.

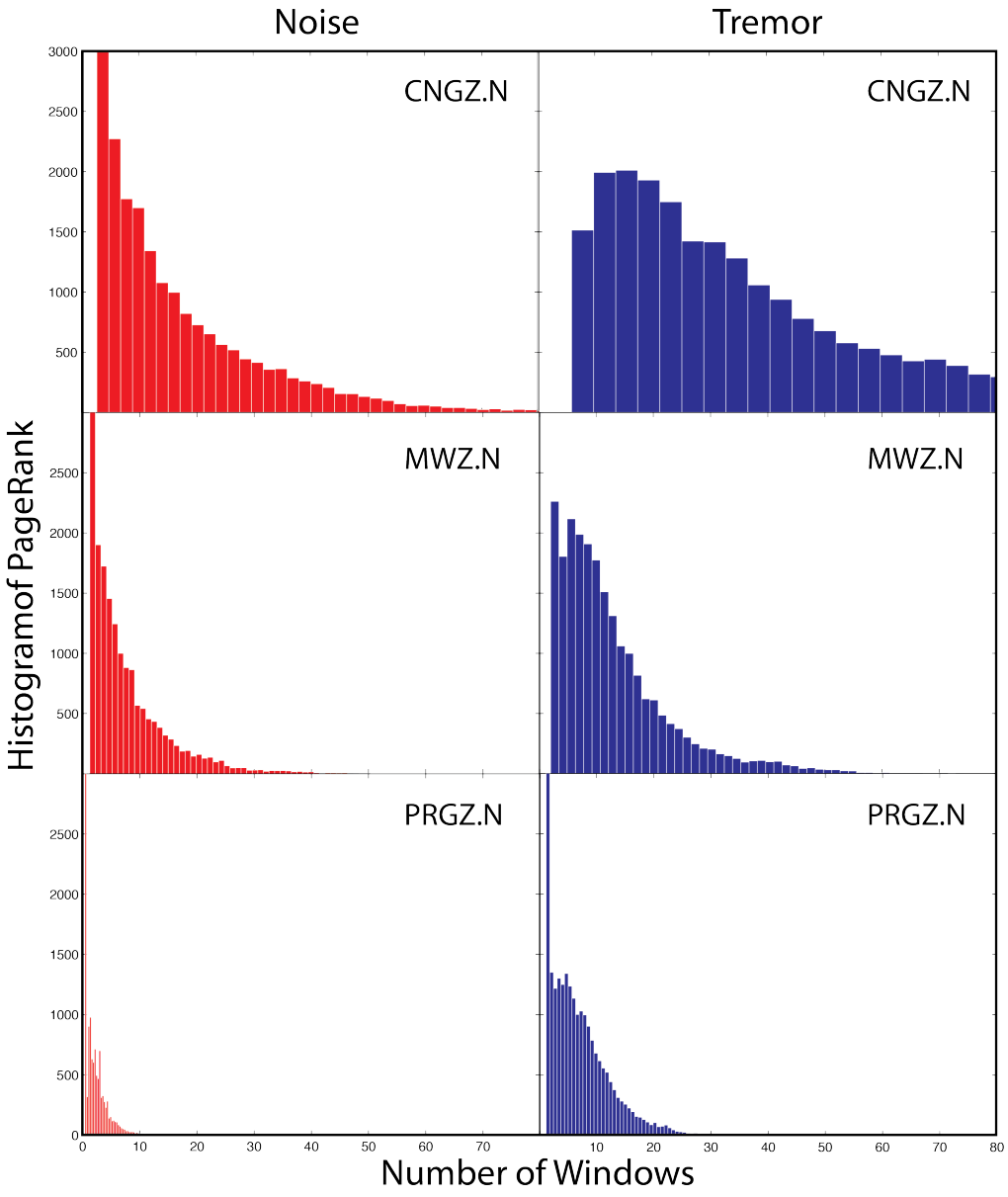

Figure 3.6: Histograms of normalized PageRank values for noise data (left) and tremor data (right) for three different stations used in the analysis of New Zealand data. Noise data shows large numbers of low PageRank values whereas the tremor data have higher PageRank values.

3.2 LFE Detections in the Northern Island

Using the LFE template created from the tremor burst during March 21 we search for other LFEs by cross-correlating the template with the 30 minutes of data previously selected to see if all tremor is explained by LFEs and whether there are LFEs occurring outside of the times of recognized tremor. We use each template on each component individually and later associate all stations and declare an LFE detection if at least eight components show a detection within a 2 second window. With this association, we show below the detections found during the tremor event on March 21, several days after the SSE has started. These detections are shown in red during the 30 minutes analyzed in Figure 3.7.

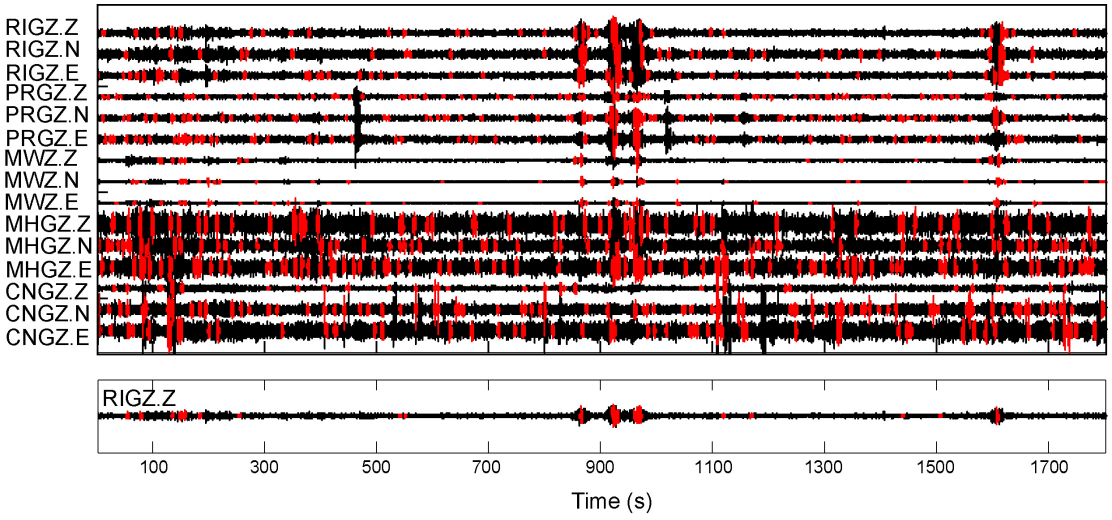

Figure 3.7: Detections found using template created from data during March 21, 2010 in 30 minutes of data during the slow slip event. (Top) Each station with detections found individually, (Bottom) Detections found after the association of stations where a detection is found in at least 8 stations show a detection within a 2 second window..

From the bottom plot in Figure 3.7, we can see in detail how the LFEs are active during the time periods were the tremor has been previously identified (between 800 to1000 s in Figure 3.7), as has been shown for tremor in other areas of the world. But we can also see that a large number of detections were found outside of these times as well.

The 2010 Gisborne slow slip event lasted about 2 weeks (Kim *et al.*, 2011). We used the LFE template created from the tremor event in March 21 to detect potential LFEs during the time period containing the entire slow slip event. We can see this result in Figure 3.8, where every bar represents three hours, and DOY 76 corresponds to March 17. The plot shows the numbers of LFE detections found from March17 to April 3, 2010 using the template create from the small tremor burst on March 21.

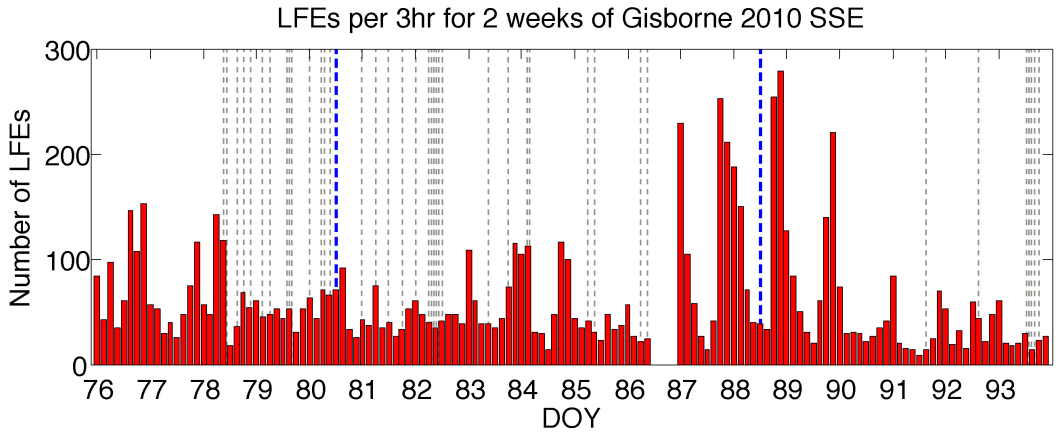

Figure 3.8: Number of detections per 3 hours of data during the 2010 Gisborne slow slip event. The plot covers the time period of March 17 to April 3. Grey lines represent a specific tremor burst from Kim *et al.* (2011) and blue lines represent the two tremor bursts used to create templates in this study.

Figure 3.8 shows many more detections outside of the known tremor bursts (Figure 3.7 and Figure 3.8) and where we might otherwise not be able to see the tremor due to attenuation, yet are still able to recover repeating signals during those times without prior knowledge of the template waveform. From Figure 3.8 we can see that the previously reported times of tremor activity from Kim *et al.* (2011) don't seem to follow a similar trend as the amount of detections found in this study increase or decrease. On closer inspection to specific days with higher numbers of detections, we find that many of these detections occur during what appears to be tremor activity of lower amplitude. Also, we find that some of the detections seem to be associated with small local seismic events. A couple of the best of these are shown in the next two

figures selected from day 87 which shows one of the highest peaks of detections (Figure 3.9 and Figure 3.10).

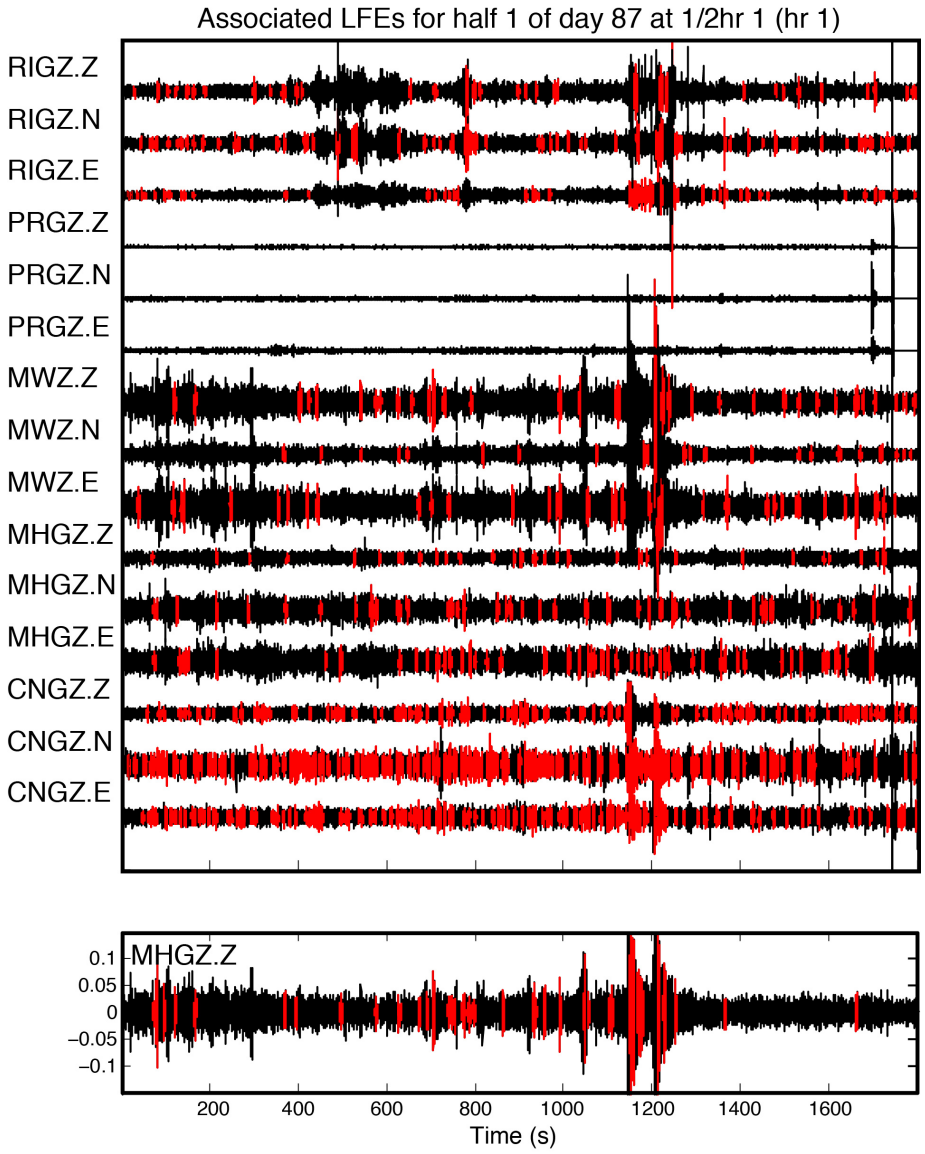

Figure 3.9: Detections found during 30 minutes of hour 1 of the first half of DOY 87 of the analysis. The top plot shows detections found independently for each station analyzed and bottom plot shows the associated station result with true detections.

The example in figure 3.9 shows two small tremor bursts, one before 200 s and another between 600 and 800 seconds. As well as some detections around the 1200 s mark that seem to be related to local seismic activity.

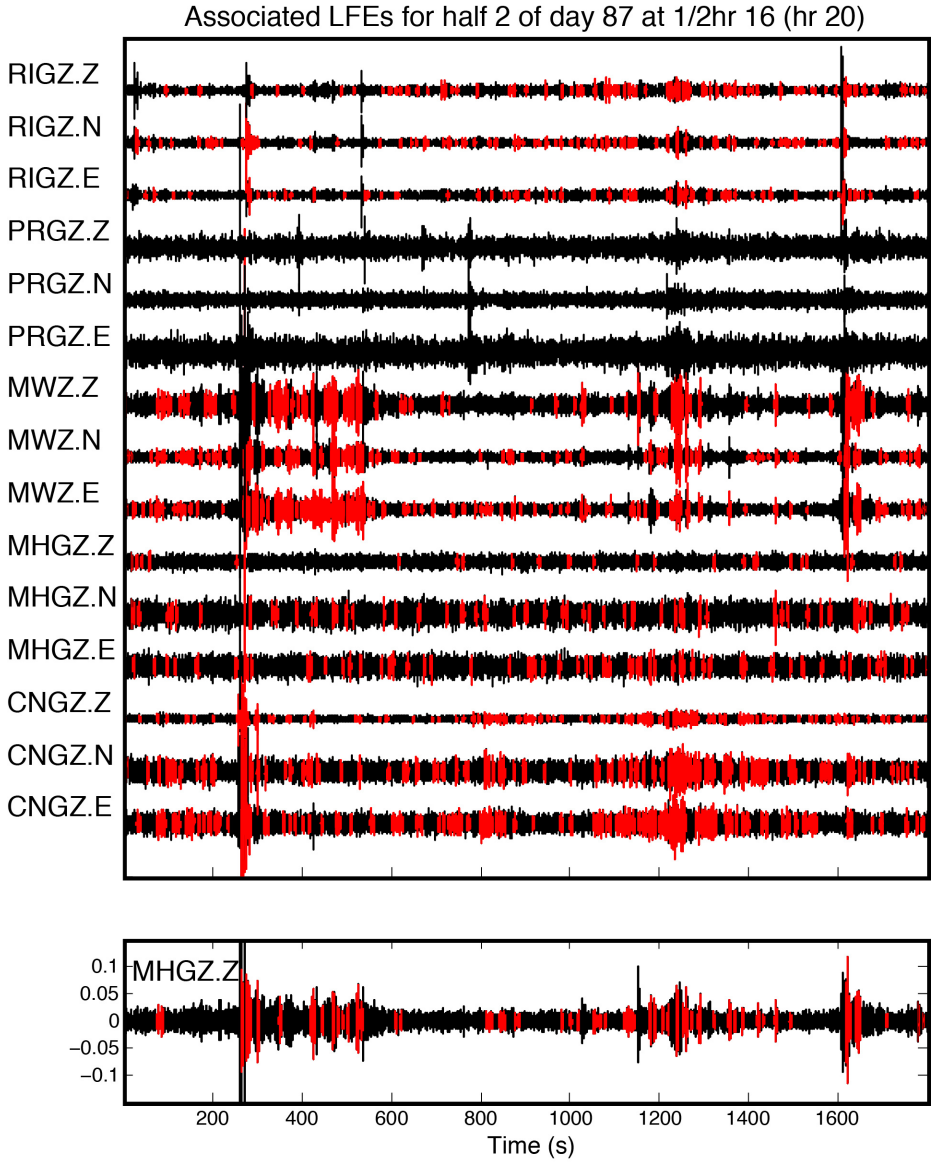

Figure 3.10: Detections found during 30 minutes of hour 20 of the second half of DOY 87 of the analysis. Top plot shows detections found independently for each station analyzed and bottom plot shows the associated station result with true detections.

The example in Figure 3.10 shows a small tremor bursts, after the 1200 s mark and another past the 1600 s mark.

3.3 Station Association based on Binomial Statistics

As previously mentioned, the PageRank algorithm was applied to each station individually due to differences in noise levels for each station. These differences translate into a variation of the statistical behavior of CC values in the autocorrelation process. Because of this, the analysis is done one station at a time and all stations are then associated based on binomial statistics.

After applying the PageRank algorithm, each station, prior to the association, has a number of individual detections - between 140 and 260 - during the 30 minutes of data shown in Figure 3.7. In those 30 minutes of data there is a population of 44,875 windows. Since I have selected the initial detection threshold to be 3σ, assuming normal statistics, the initial one-sided probability of finding a detection is 1 in 370 or 0.0027. Using this initial probability, we can use binomial statistics to calculate the probability of finding a certain number of detections on one component given our total population of 44,875 windows.

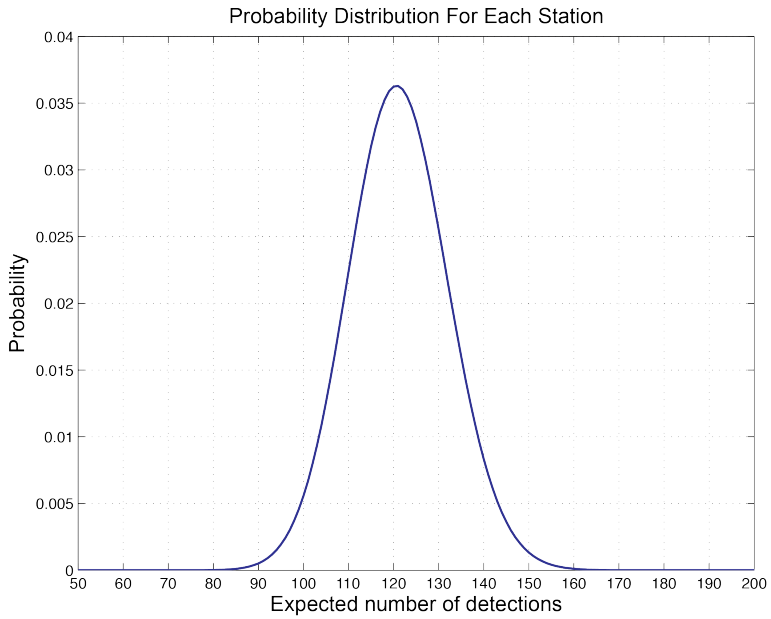

Figure 3.11: Probability distribution for the expected number of detections for each station with an equal initial one-sided probability of 0.0027 for normal statistics.

For an initial equal chance of each window to be a true detection, the binomial distribution predicts a most probable number of detections of 121 for each station (Figure 3.11). The number of detections that I find for each station is higher than this number (140-260). The difference in our detection numbers is to be expected given that we expect a repetitive signal within the data, which should result in a higher number of correlated windows; however, this only describes the probabilities for one station. Assuming that all stations are independent, and if we have a population of 15 components, we can calculate the probability of at least a significant number of components showing a positive detection, where the initial probability can be approximated as the total number of detections divided by the population of independent windows.

We consider windows that are detected within 2 seconds of each other to be redundant detections of the same signal. We don't want to count this type of detection twice so we have to consider this factor in our population of windows. A 2-second window in our data is equivalent to 50 samples for data with 25 sps. Taking this into account, the total number of windows in our population becomes n = 44,875/50 or ~878 windows. The initial probability for each station is the total number of detections divided by n. Since the total number of detections for each component does not vary substantially (140-260), we decided to calculate the initial probability for each station using an average of this range. The average of the range of detections for our group of stations is about 150, so our initial probability will be p_i = 150/878. With this initial probability, we can again use binomial statistics to calculate the probability density function. We determine the probability of finding a window to be a true detection if the same window is found in a significant number of components that we consider to be robust.

We have worked with a total of 15 components for this analysis. We choose to declare a window a true detection if that window is found in the total number of stations that gives us a probability of finding one false detection in about 1000 or

0.001. From Figure 3.12, this probability is closest to an expected number of 8 stations to find a positive detection for a specific window in time. Using this, during the association process, we declare a detection if a positive detection was registered on at least 8 of the individual components analyzed. Following the description above we can calculate the probability of finding at least 8 components to show a detection for a specific window. With this, and using binomial statistics, the probability of finding at least 8 components with a positive detection on a given window is 0.0011 (Figure 3.12). Under the null hypothesis this would result in one false positive in 909 windows.

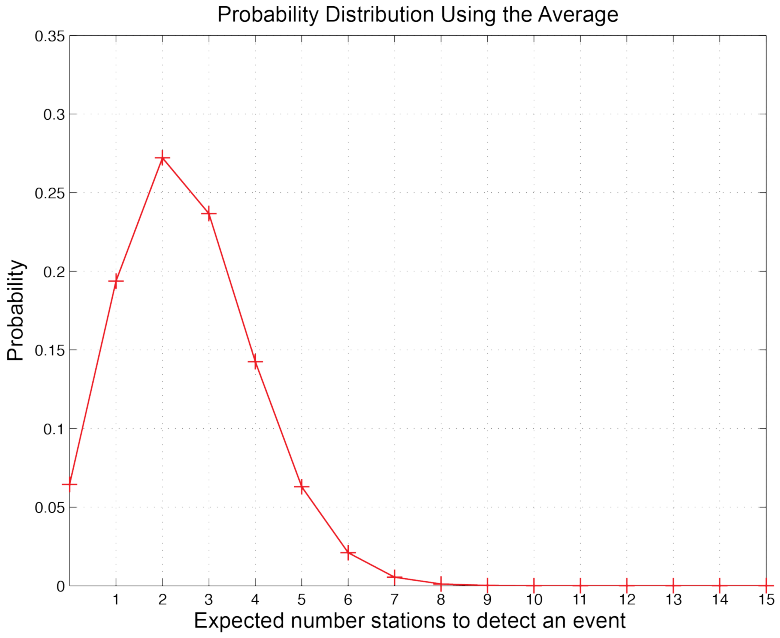

Figure 3.12: Probability distribution for all stations using an average equal probability for each station for 15 components.

3.3 Search for LFE *P*-waves during the 2010 Gisborne SSE

We have assumed that the signal obtained with PageRank corresponds to the *S*-wave of the LFE templates because it is well observed on all three components for each station. Given this assumption, we later expanded the window size to search for *P*-waves in the March 21 data set. I illustrate this with gray-scale plots (Figure 3.13)

with the expanded windows and visually inspect the data for a clear arrival prior to the *S*-waves detected.

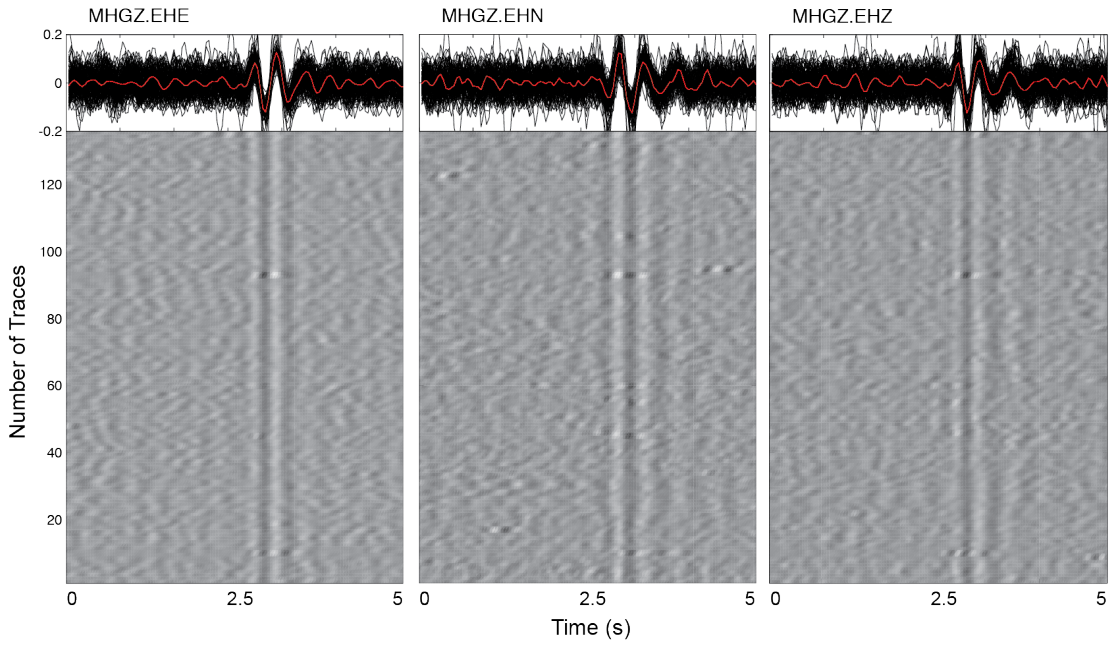

Figure 3.13: Gray-scale plots showing the *S* wave found by aligning all events (black traces on the top) detected during the New Zealand analysis for data during March 21, 2010. Each plot shows a different component for station MHGZ and they were created using data from. Red trace represents the summed aligned traces, and each line on the gray scales represents each LFE detection found.

We performed an inspection and cross-correlation of times prior to the *S*-wave during the possible relative arrival times, calculated from the tremor locations to the stations used in the analysis. After detailed visual analysis, no *P*-waves are apparent on any of the stations used in this study for the LFE detections found using the template from March 21st, 2010. Given that the tremor events observed are very small, and only a few of them are observed during the slip event, it is possible that with the existing data, we are unable to observe the *P*-waves associated to these detections. We also performed a location test using only *S*-wave cross-correlation relative times to use in a double difference earthquake hypocenter location (using hypoDD). The locations

obtained from these relative arrival times just from the *S*-wave presented large errors and are not robust, therefore we don't show them here.

The slow slip event occurred offshore of Gisborne and all the stations used in this analysis are inland suggesting that the waves have to travel through a highly attenuating medium of marine sedimentary rocks (Eberhart-Phillips and Chadwick, 2002; Kim *et al.*, 2011), preventing the tremor signal from being well observed on these stations. Also, given that all stations used are surface stations, noise levels are higher, also creating a higher difficulty to show a clear tremor signal. These constraints, as well as the lack of visible *P*-waves in the data have not allowed us to locate the LFE events found during the two tremor bursts analyzed here as well as the 2 weeks of data analyzed.

3.4 Discussion and Conclusions

We have applied the PageRank algorithm to detect LFEs within tremor data for the 2010 New Zealand Gisborne slow slip event. We selected this data set given that tremor has been shown to occur, even though the clear, large-amplitude tremor bursts are of much shorter duration than in other tectonic settings were tremor is observed.

We focus the analysis on two distinct tremor bursts, eight days apart, during the slow slip event and find that the templates created using the PageRank algorithm are very similar for both data sets analyzed, suggesting a similar location and mechanism for both tremor bursts. We selected the template created from the data set of March 21 given that all stations are more consistent and use this as a template to search for LFEs in a longer data set.

We use the template created from March 21 for each stations and component to detect new LFEs within the two weeks of data during the 2010 Gisborne slip event.

We find many LFE detections within the data not only during the small tremor bursts previously documented by Kim *et al.* (2011), but outside of them as well. Closer inspection of detection times show that many detections are within many possible smaller amplitude tremor bursts that were previously missed as well as we observe that some detections seem to be associated to small seismic activity in the area. Over all, it is evident that tremor is not easily observable in this data set, possibly due to high seismic activity in the area as well as noise signal, poor seismic coverage, or a more sporadic nature than elsewhere, or some combination of these three factors; however, we are still able to recover the LFEs within the signal even though we are not able to observe any *P*-waves, but relative arrival times from cross-correlation from only the *S*-waves do not provide reliable locations for the events found during the analysis. For New Zealand tremor on the North Island, a larger station coverage and data set will be necessary to observe tremor clearly and find more robust repeating LFEs within the tremor, as well as locate these LFEs with little uncertainty. But with the available data, we were able to show that the small tremor bursts from March 21 and March 29, which we focused our analysis on, are mostly explained by LFE detections, as has been shown in other places of the world were this phenomenon occurs. We were also able to identify smaller amplitude tremor activity by applying the PageRank algorithm.

Finally, to test PageRank against noise data, we created histograms of the normalized PageRank values for tremor and compared this result with noise data from the same stations. We find that distributions of PageRank for tremor have a tendency towards the large values whereas the noise distributions trend towards small values, showing that there are many more windows with connections within the tremor data set and suggesting a true repeating signal within the data.

CHAPTER 4

Comparing Low Frequency Earthquakes within Ambient and Triggered Tremor in Southern Taiwan

The Island of Taiwan is located in a complex tectonic setting. To the northeast, the Philippine Sea Plate subducts under the Eurasian Plate forming the Ryukyu arc system and to the south, the South China Sea subducts under the Philippine Sea Plate at the Manila trench (Yu *et al.*, 1997). The island is divided into several north-northeast trending geologic provinces (Yu *et al.*, 1997). The Central Range province is part of this arc-continent collision environment and it is another place where tectonic tremor has been observed. Tremor was first observed here under the southern Central Range, triggered by the Love waves of the 2001 M_w 7.8 Kunlun earthquake in northern Tibet (Peng and Chao, 2008).

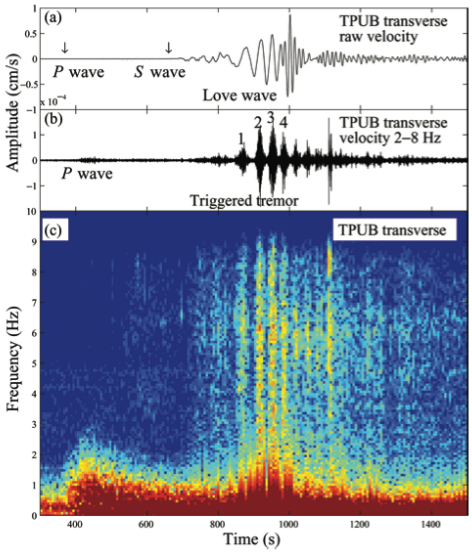

Figure 4.1: Figure from Peng and Chao (2008) showing examples of triggered tremor during the surface waves of the 2001 November 14 *M* 7.8 Kunlun earthquake. (a) Broad-band transverse- component seismogram recorded at station TPUB. (b) 2–8 Hz bandpass-filtered vertical-component data showing the high-frequency *P* waves and the triggered tremor during the passage of the Love waves. (c) Spectrogram of the vertical-component seismogram.

Tremor was later observed to be triggered by a series of teleseismic earthquakes (Tang *et al.*, 2010; Chao *et al.*, 2012; Chao *et al.*, 2013). As the Love waves travel perpendicular to the Central Range, tremor has been triggered under the southern Central Range (Figure 4.2) (Tang *et al.*, 2010; Chao *et al.*, 2012), and there is evidence of tremor triggered below the northern Central Range(Chao *et al.*, 2013).

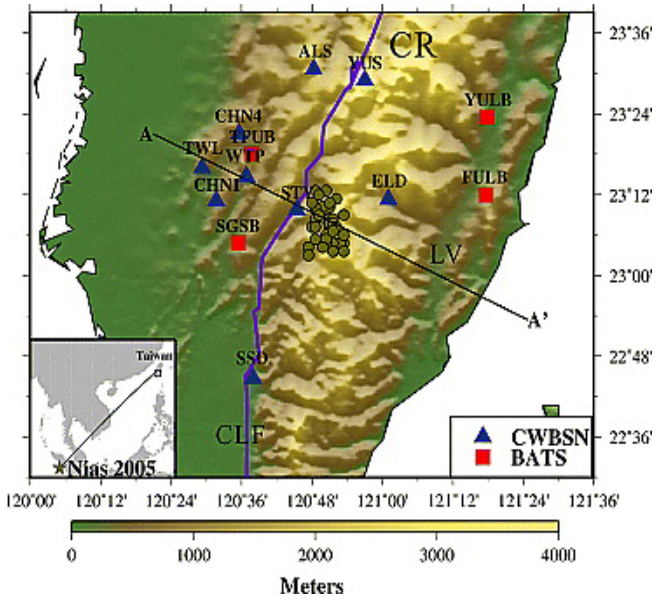

Figure 4.2: Figure from Tang *et al.* (2010) showing the location of their study and locations of LFEs in southern Taiwan, under the Central Range.

As observed elsewhere, Tang *et al.* (2010) demonstrated that triggered tremor in Taiwan is also composed of LFEs, which were originally identified manually and later used as templates to detect more triggered LFEs (Tang *et al.*, 2010). They were able to explain part of the tremor with LFEs and found that these locate under the central Range (Figure 4.2), close to downward extension of the steep-dipping Chaochou-Lishan fault (Figure 4.3).

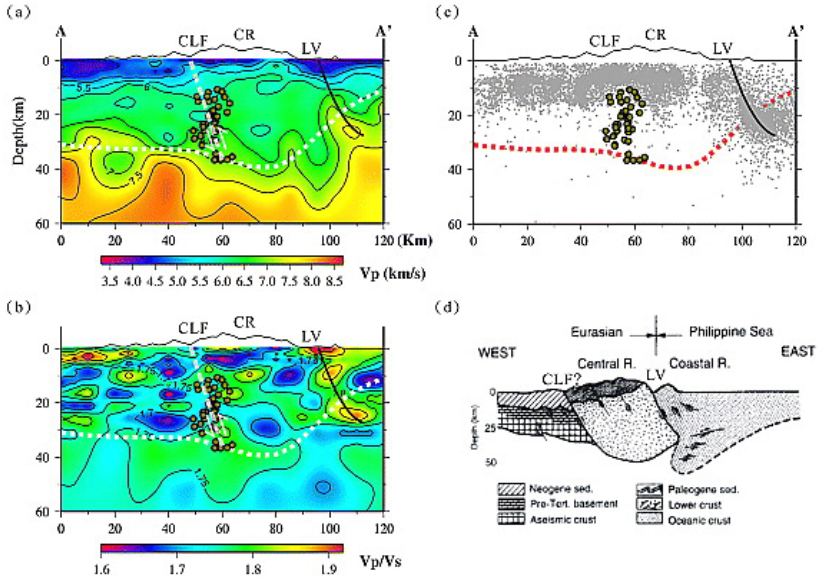

Figure 4.3: Figure from Tang *et al.* (2010). (a) LFEs locations plotted on a V_P velocity model, (b) V_P/V_S profile, and (c) background seismicity from 1991 to 2008 along the AA' projection shown in Figure 4.1. White dotted lines show the Moho depth approximation. CLF, Choachou-Lishan Fault; LV, Longitudinal Valley suture. Black solid line indicates a assumed direction of the LVF. Thick gray dashed line represents the depth extension the CLF. (d) A simple illustration of the Lithospheric Collision Model

Ambient tremor has also been reported under the southern Central Range (Chuang *et al.*, 2014), and it locates to a similar area to where the triggered tremor has been located (Figure 4.4).

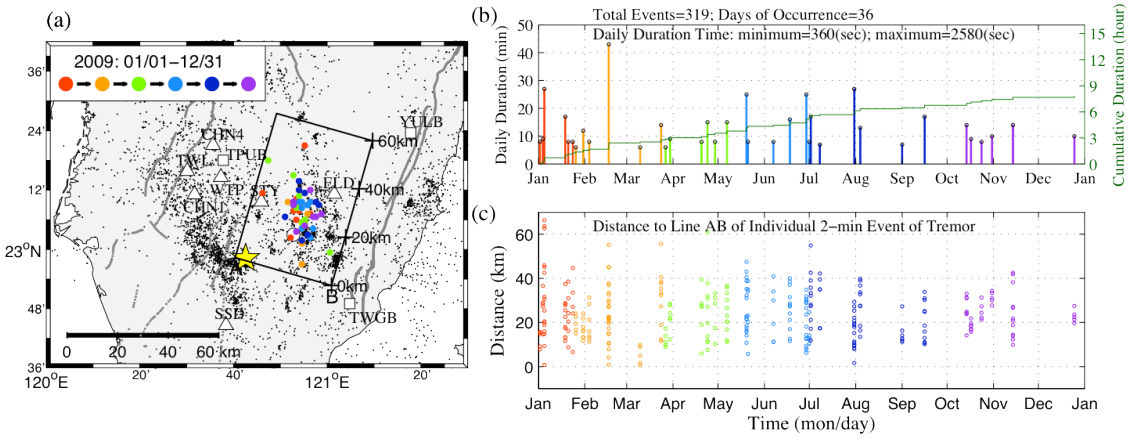

Figure 4.4: Figure from Kevin Chao. (a) Tremor locations color coded by time. (b) Tremor duration during 2009. (c) Distance to AB line.

Even though these studies locate the tremor bursts under the southern Central range and possibly close to the Choachou-Lishan Fault (Tang *et al.*, 2010), the location uncertainties leave it unclear whether the downward extension of this fault is the source of the tremor, and therefore the source of the LFEs.

4.1 Page Rank applied to Tremor in Taiwan

To help constrain the source of the tremor and the LFEs in this area, we applied the PageRank algorithm described in Chapter 2 to compare triggered and ambient tremor by creating LFE templates for tremor during each case, triggered and ambient independently, in the southern Central Range. We do this without *a priori* knowledge of the template signature.

4.1.1 Ambient Tremor:

Ambient tremor bursts are ongoing in southern Taiwan, so to start our analysis we selected one day with very clear 30-minute tremor episode (Figure 4.5) on January 19, 2009.

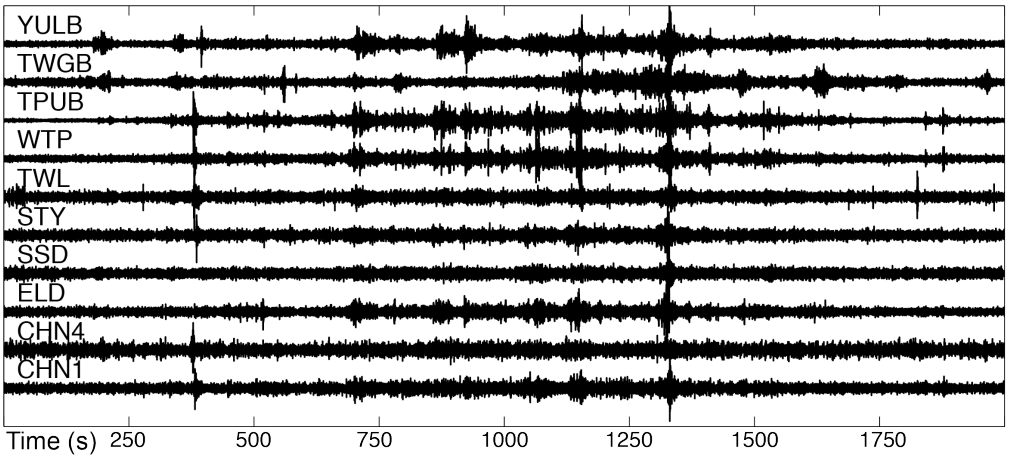

Figure 4.5: Ambient tremor data analyzed in this study using the PageRank algorithm. The plot shows 30 minutes for the horizontal component of the 10 stations that were available during January 19, 2009.

We apply the PageRank algorithm to these 30 minutes of ambient tremor data and create an LFE template for each of the 10 stations available during this time period. We perform this analysis one station, and one component at a time, as explained in Chapter 2, for tremor data band-pass filtered between 4 to 6 Hz. For this analysis we use a 10 second window for the initial cross-correlation.

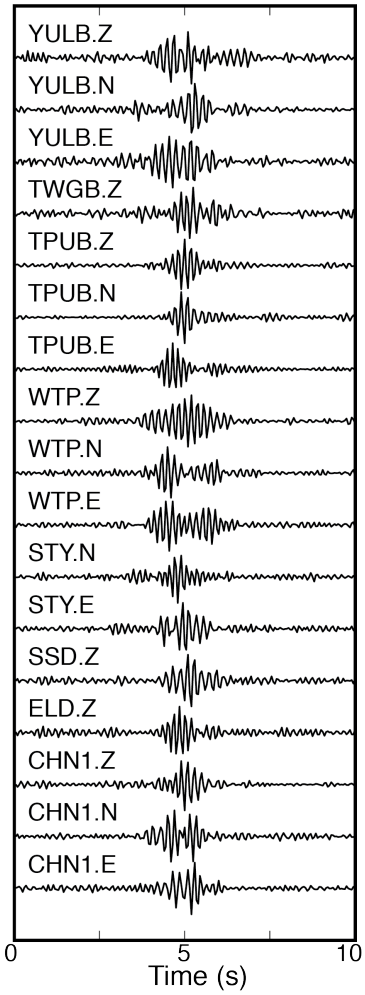

Figure 4.6: Plot of the all three components of the stack created using the PageRank analysis of ambient tremor data during 30 minutes of January 19, 2009. The plot shows the 10 stations available during the tremor event selected.

The LFE stacks created (Figure 4.6) for all components of the 10 stations, each done independently, are very consistent within stations and will be used as templates to find other LFEs within continuous data.

To analyze whether there are a large number of repeating events, we calculated the histograms of the tremor PageRank values, as was done in the previous chapters, to see if the distributions show larger numbers of linked windows. Figure 4.7 shows that this is the case for the ambient Taiwan tremor, suggesting a real repeating signal within the tremor under analysis.

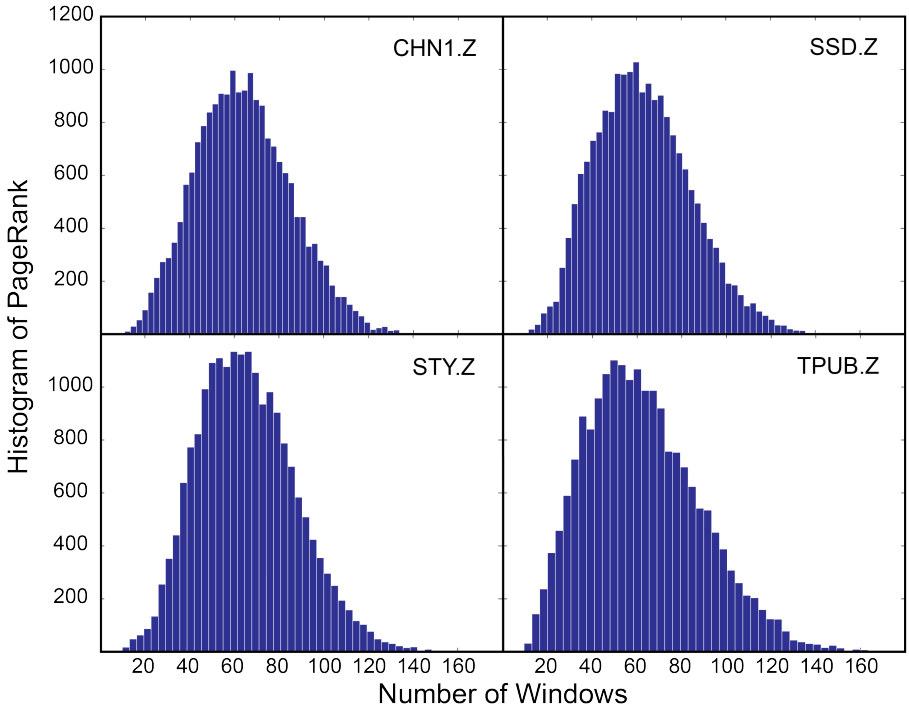

Figure 4.7: PageRank histograms for 4 different stations in Southern Taiwan, showing that the distributions for each station have large numbers of highly ranked windows during the tremor data analyzed.

In previous chapters, we were able to compare the PageRank distributions of tremor to similar distributions calculated for noise data. For this data set we only have segmented data with tremor in it, not continuous data. Because of this, the comparisons between the tremor and noise PageRank distributions have not been possible, but we would expect the noise data to behave as in previous analysis, showing that small numbers of links are predominant in the data.

4.1.2 Triggered Tremor:

As mentioned before, several earthquakes have triggered tremor in southern Taiwan. The 2005 March 28 *Mw 8.6* Nias earthquake is one of the earthquakes that triggered tremor here, and Tang *et al.* (2010) used LFEs found manually as templates to detect other LFEs within the tremor. We selected data during the time period of this earthquake to apply the PageRank algorithm. We focus on 30 minutes of data where the tremor is clearly observed, through the passing of the surface waves. We selected the stations that match stations used in the analysis of the ambient tremor in the previous section. These are 8 stations from the previous 10 stations analyzed and the tremor is shown in Figure 4.8.

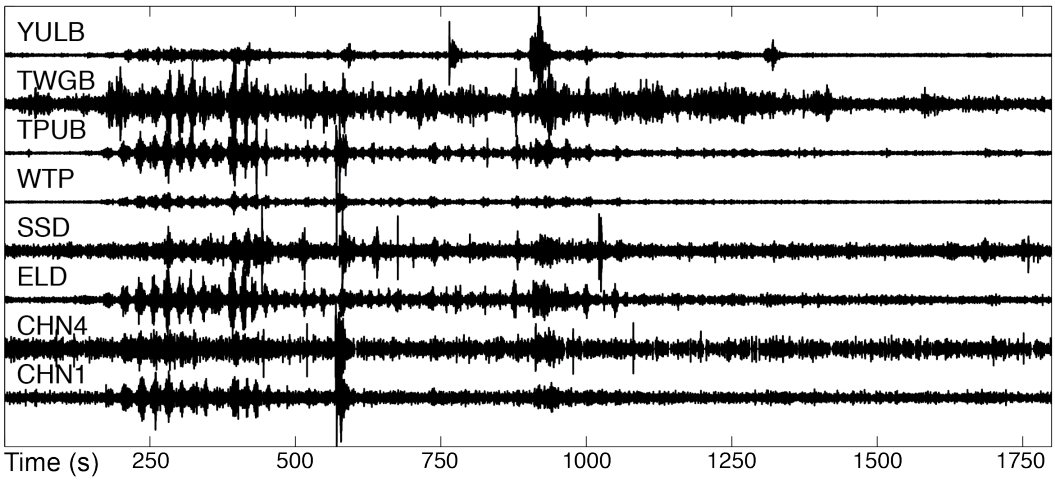

Figure 4.8: Triggered tremor data analyzed in this study using the PageRank algorithm. The plot shows 30 minutes for the horizontal component of the 8 stations that were available during the 2005 March 28 *Mw 8.6* Nias earthquake.

We apply the PageRank algorithm to these 30 minutes of data and create an LFE template for each of the 8 stations available during this time period. As for the ambient tremor, we do this analysis to each component individually using a filter of 4-6 Hz and a 10 second window for the initial cross-correlation. The templates created for triggered tremor are shown in Figure 4.9 below.

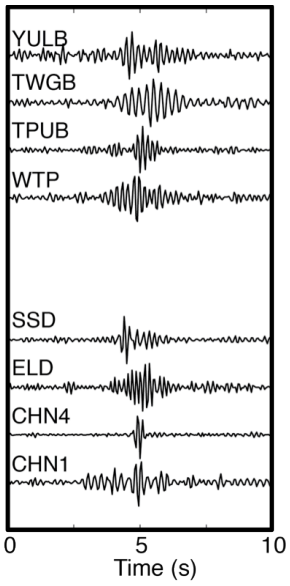

Figure 4.9: Plot of the north component of the stack created using the PageRank analysis of triggered tremor data shown in Figure 4.5. Here, the 8 stations available are shown in the plot.

4.2 Comparing the LFE Templates from Ambient and Triggered Tremor

As has been shown in previous studies, using both envelope cross-correlations as well LFE found manually within the tremor to locate the tremor source; ambient and triggered tremor seem to originate from a similar area (Chao *et al.*, 2012; Chao *et al.*, 2013; Chuang *et al.*, 2014) (Figure 4.2, Figure 4.4, and Figure 4.10). We have compared the templates created from both ambient and triggered tremor.

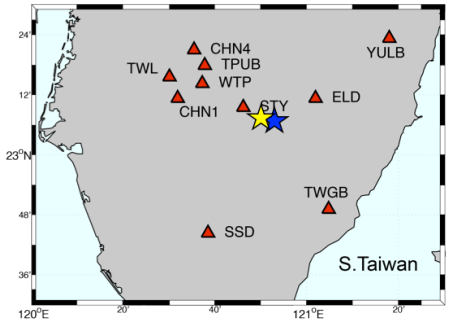

Figure 4.10: Map of southern Taiwan showing the approximate location for ambient (blue star) and triggered (yellow star) tremor inferred from previous studies (Chao *et al.*, 2012; Chao *et al.*, 2013; Chuang *et al.*, 2014). Red triangles are stations used on in the analysis.

During the triggered tremor events, only 8 of the stations were available, and among these stations, not all components were available. For the comparison, we use all components available at the time of the 2005 Nias earthquake and compare them to the components for ambient tremor (Figure 4.11).

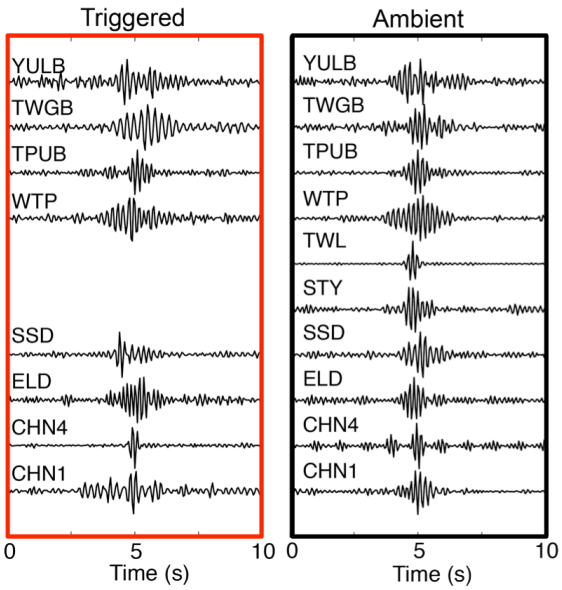

Figure 4.11: Plot of the vertical component of the stack created using the PageRank analysis of triggered tremor in red and ambient tremor in black.

The LFE templates created from triggered tremor are very similar to those created from ambient tremor. This can be seen in Figure 4.12 as the cross correlation coefficients of the signals are mostly above 0.5

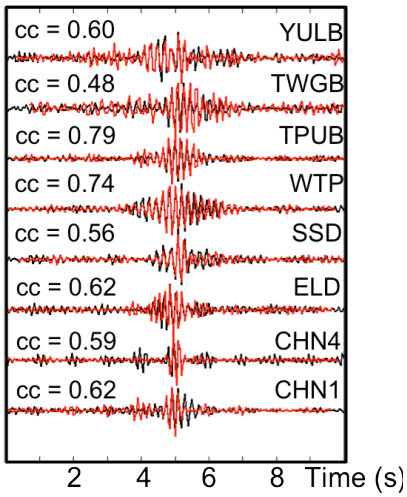

Figure 4.12: Comparison of the waveforms of both templates created from triggered (red) and ambient (black) tremor using the PageRank analysis on data shown in the previous sections.

To test this similarity further, we have used both templates interchangeably, that is, we use the template created from triggered tremor to detect LFEs within ambient tremor and use the template of ambient tremor to detect LFEs within triggered tremor. Here, we show results of both stacks used during the triggered tremor of the 2005 Nias earthquake (Figure 4.13 and Figure 4.14).

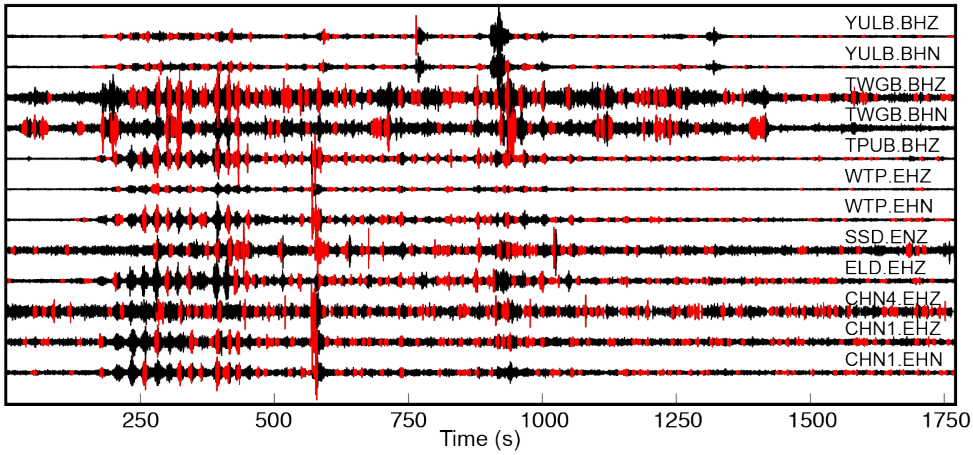

Figure 4.13: LFE template created during ambient tremor in 2009 used to detect LFEs within triggered tremor in 2005. Red traces are detections found for each station individually.

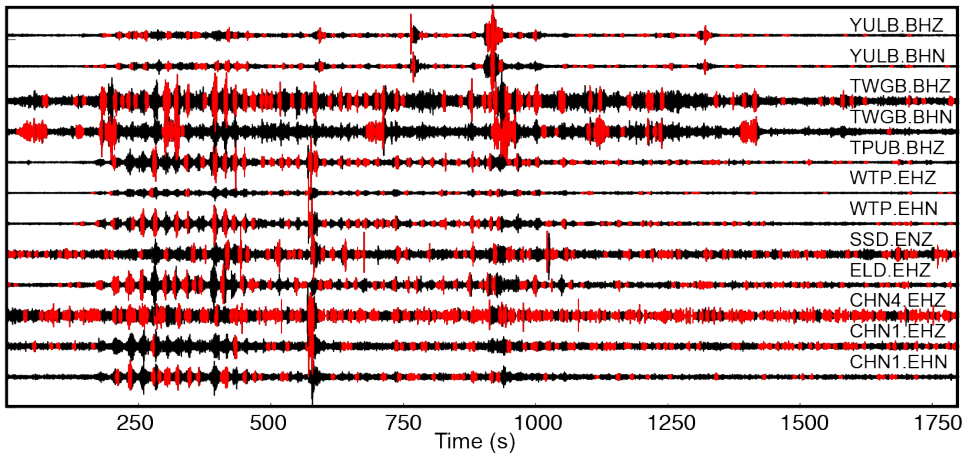

Figure 4.14: LFE template created during triggered tremor in 2005 used to detect LFEs within the same triggered tremor. Red traces are detections found for each station individually.

We find that most of the ambient tremor can be detected by the LFE templates created from either data set. We also find that most triggered tremor bursts are explained by both templates. Given that each station has a different number of detections, we compare both results for each station individually to quantify how much overlap was detected using both templates. The number of detections found for each component is listed in Table 4.1, as well as how much detection overlap occurs between the two cases.

Table 4.1: Total number of detections found using each template and total overlapping detections

Component	Triggered Tremor Template	Ambient Tremor Template	Overlap
YULB.BHZ	76	59	33
YULB.BHN	73	69	29
TWGB.BHZ	75	78	31
TWGB.BHN	61	57	35
TPUB.BHZ	74	85	53
WTP.EHZ	33	55	21
WTP.EHN	67	75	42
SSD.EHZ	87	66	31
ELD.EHZ	87	80	41
CHN4.EHZ	208	92	71
CNH1.EHZ	84	81	36
CHN1.EHN	54	73	21

To declare true detections, we associate all stations for each case as shown in section 3 of chapter 3. These results are shown in figure 4.15 in red for each tremor case.

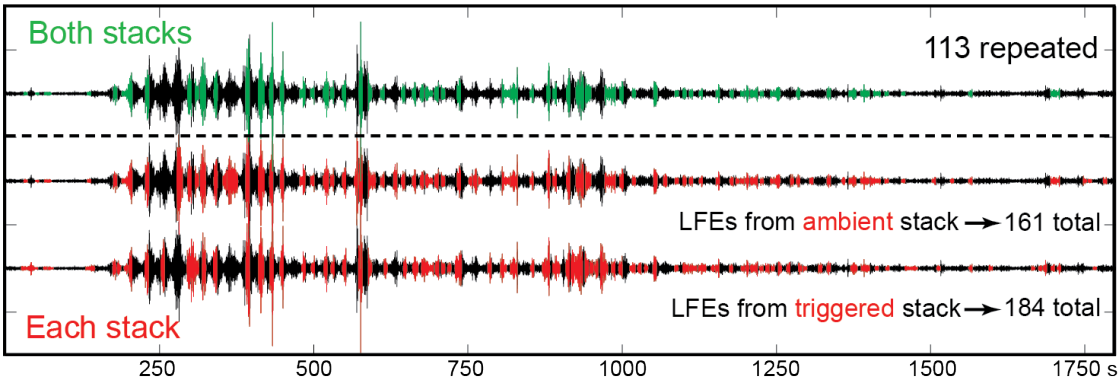

Figure 4.15: Detections found by association of stations for both ambient and triggered tremor analyzed independently (red top and bottom respectively) compared to the detections that overlap in both analyses plotted in green on the top trace.

After associating all stations for each case, the stack from triggered tremor revealed a total of 184 detections for a population of 19,920 windows during the 30 minutes of data. The template from the ambient tremor found a total of 161 detections for the same data set. By comparing these, both templates found a total of 113 detections that overlap (green, Figure 4.15). This means that 61% of the detections found by the triggered tremor template are detections in common, and 70% of the detections found by the ambient tremor template are detections in common. Calculating this percentage for both cases we find an average of about 66% of detection overlap between the two templates. This similarity between both LFE templates suggests that the LFEs for both events (triggered and ambient) are generally coming from similar sources.

4.3 Comparing the LFE Templates to Local Earthquakes

The templates we have created from ambient tremor represent the *S*-wave from the LFEs. After detailed visual inspection of times ahead of the *S*-wave, no clear P-waves are present. As an initial attempt to observe the P-waves in the data, after visual

inspection proved unsuccessful, we rotated each horizontal component independently to the angle that maximized the amplitude of the tremor. Testing a series of angles between 0 and 90 degrees, we picked the rotated component (Figure 4.16) with the maximum amplitudes for the tremor signal and used that to look for the *P*-waves in the same manner as before.

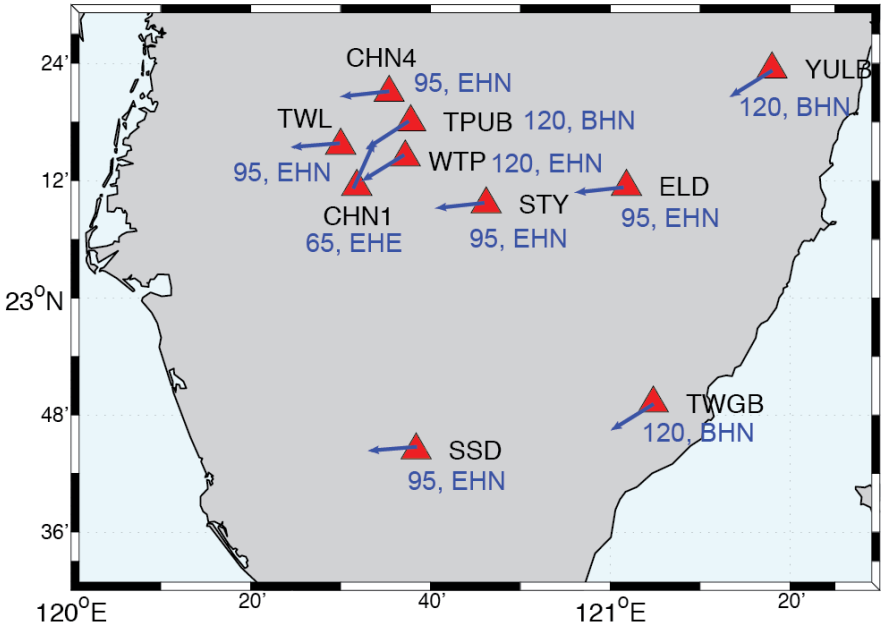

Figure 4.16: Map showing the angles of rotation for each station, and the component that show the maximum amplitude after the rotation. Both the angle, in degrees and the component are shown in blue next to each station on the map.

After detailed analysis of the horizontal components, rotated as shown in Figure 4.16, there is still no clear evidence of a *P*-wave signal that rises above the noise in the data.

Given this difficulty, we proceeded by taking a different approach to extract the *P*-wave information. The area where tremor has been observed is a tectonically active area, where many small earthquakes can be detected. With previous knowledge of local seismicity, we take advantage of small earthquakes that locate in nearly the

same area as the tremor. From the data available, we picked a set of earthquakes that widely sample the area were tremor occurs, but still have highly similar waveforms. We make this selection by applying a simple clustering algorithm based on cross-correlation. The group of earthquakes selected by the clustering algorithm has 27 events, which are shown in yellow in Figure 4.17.

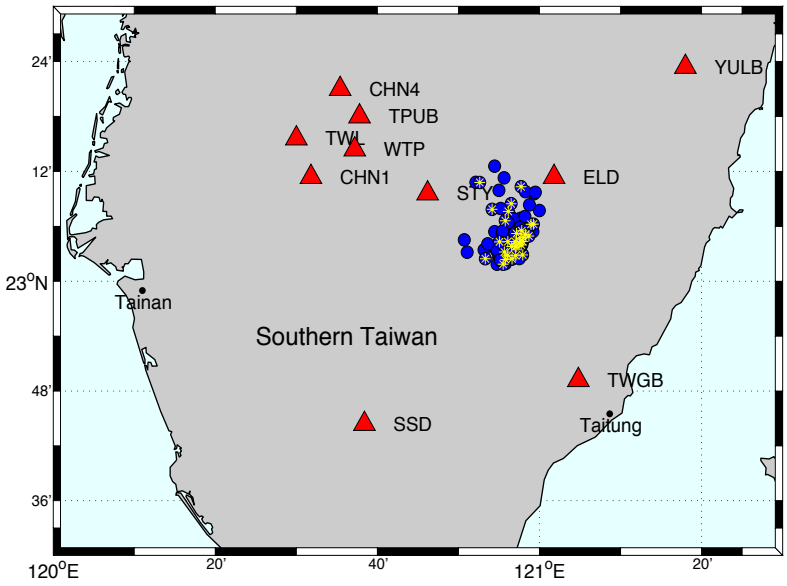

Figure 4.17: Map showing the 27 earthquakes (yellow dots) used to compare to the LFE template, selected out of the total of 98 events (blue).

We compare the LFE template for the most quiet stations to each of the earthquakes from the cluster to see if the template *S*-wave is similar to each earthquake's *S*-wave. For this, we cross-correlate the template with each earthquake and align them based on the cross-correlation (Figure 4.18).

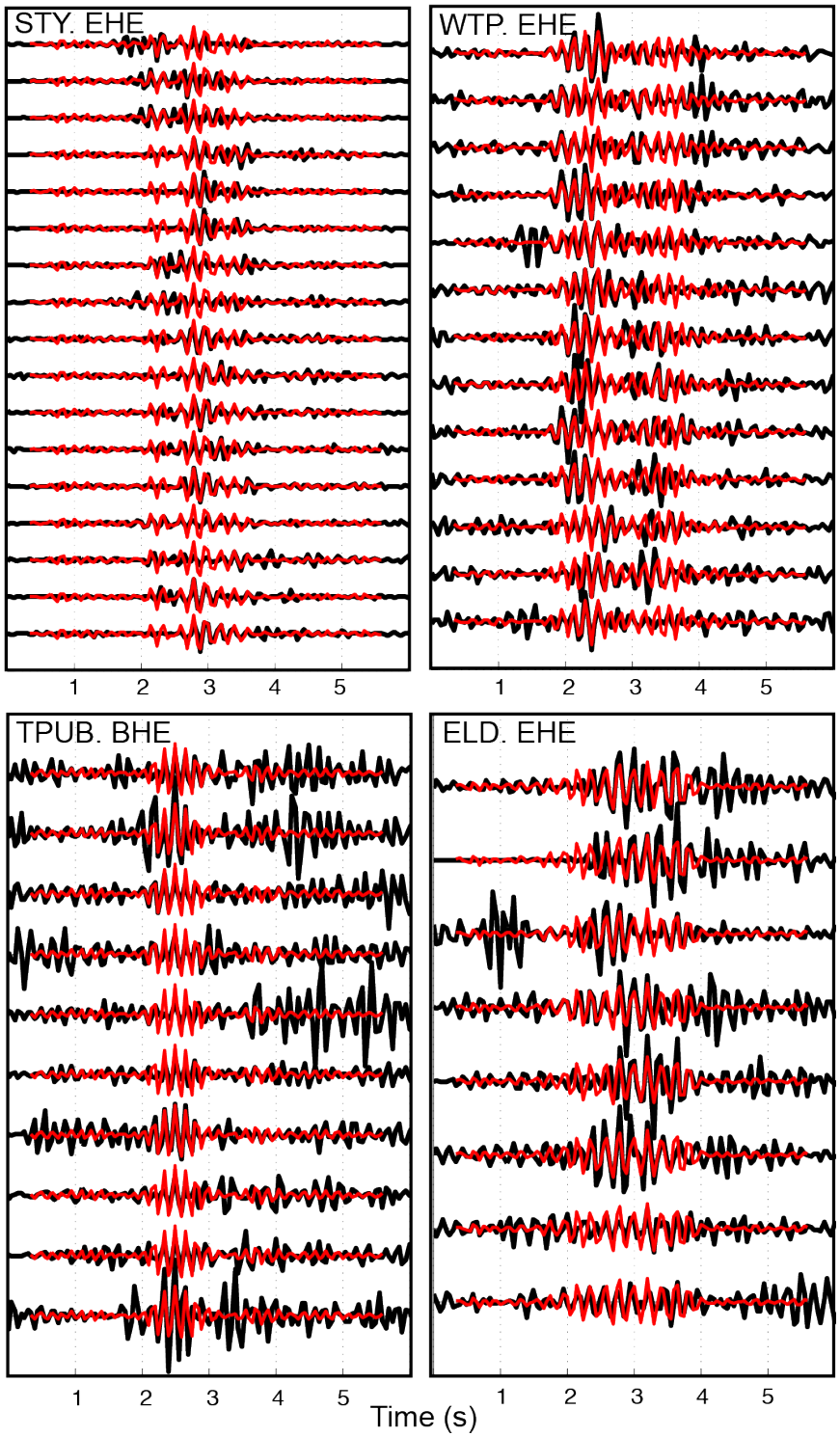

Figure 4.18: Clustered earthquakes (black) band-pass filtered and aligned using cross-correlation with the LFE template (red) from ambient tremor, four different stations from the analysis are shown with events that had a CC value higher than 0.4.

All cross-correlations with CC above 0.4 are shown in Figure 4.18 for 4 different stations, on one horizontal component. From this we can see that the template signal obtained from tremor is very similar to the *S*-wave of the clustered earthquakes for most of the stations. The similarity between the LFE template and the earthquakes suggests the repeating signal found during the tremor is coming from the same area as the clustered earthquakes. This similarity also allows us to use the *P*-wave information from the earthquakes, which is very clear, to find the *P*-waves of the LFEs and locate them with greater accuracy. Therefore, from the earthquake data we pick the average *P*-wave arrival time for all events and use this time to search for the *P*-wave on the LFE detections found using the ambient tremor data.

The LFE detections previously found during the ambient tremor data set can be cross-correlated again to find the relative arrival times between events. We cross-correlated each detection with all others to find these times. As mentioned before, the *S*-wave arrival for all events is very clear, but the *P*-wave cannot be easily observed. Using the average *P*-wave arrival time from the local earthquakes we have cross-correlated the LFE detections again, focusing on the time where the *P*-wave should be. The relative arrival times for the most quiet stations are shown in table 4.2

Table 4.2: Average relative arrival times estimated from local earthquake data

Station Name	***S-P* arrival time (s)**
CHN1	3.0
ELD	3.75
STY	3.25
WTP	4.0
TPUB	6.25
YULB	6.25

The results using all LFE detections (a total of 141 LFEs) found using the ambient tremor data, for the aligned signals to both, *S*-wave and *P*-wave independently, are shown in the following plots:

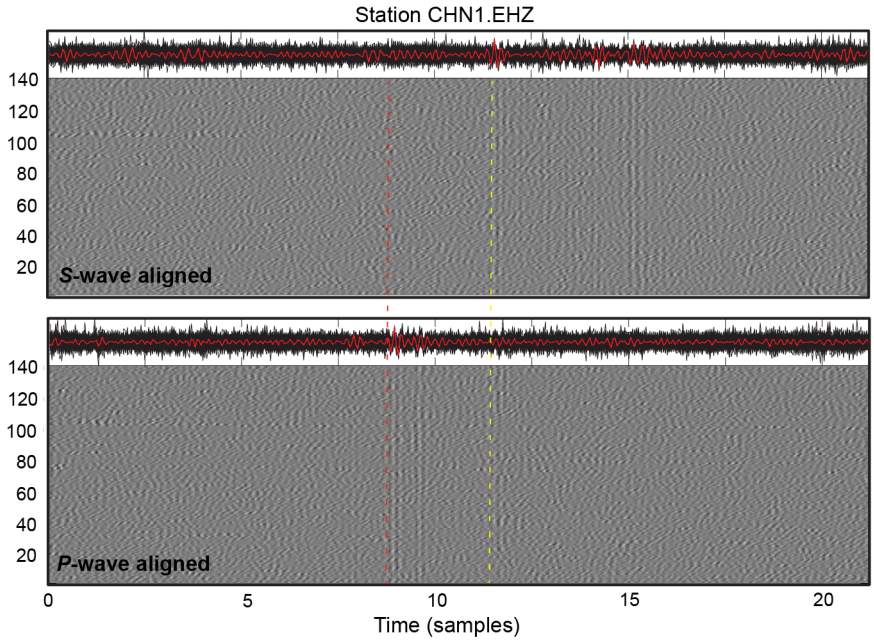

Figure 4.19: Grayscale plots of the LFE detections from ambient tremor (black traces) for component CHN1.EHZ, aligned by cross-correlation to the *S* wave (top), and aligned by cross-correlation to the *P* wave (bottom). Yellow and red dashed lines show *S*-wave and *P*-wave arrivals respectively.

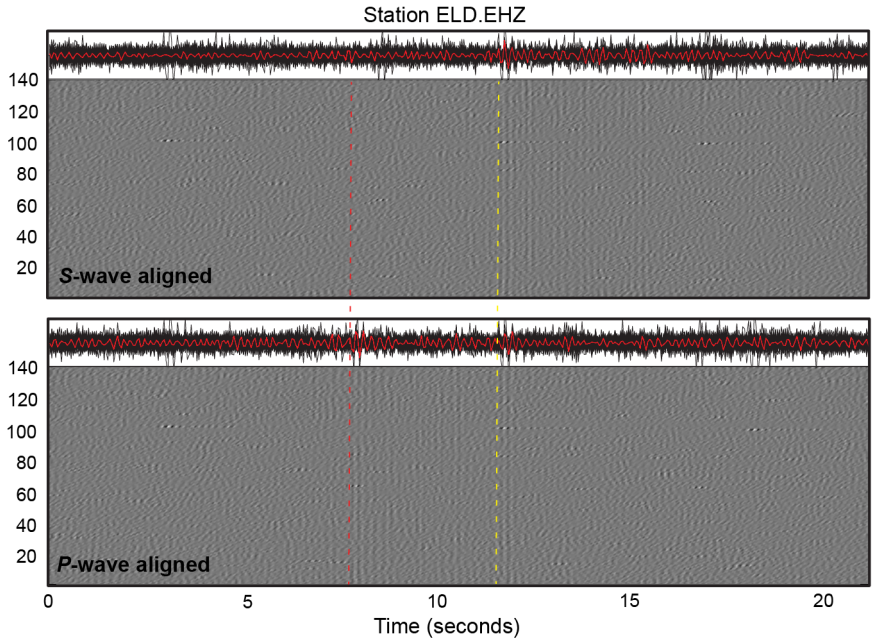

Figure 4.20: Grayscale plots of the LFE detections from ambient tremor (black traces) for component ELD.EHZ, aligned by cross-correlation to the *S* wave (top), and aligned by cross-correlation to the *P* wave (bottom). Yellow and red dashed lines show *S*-wave and *P*-wave arrivals respectively.

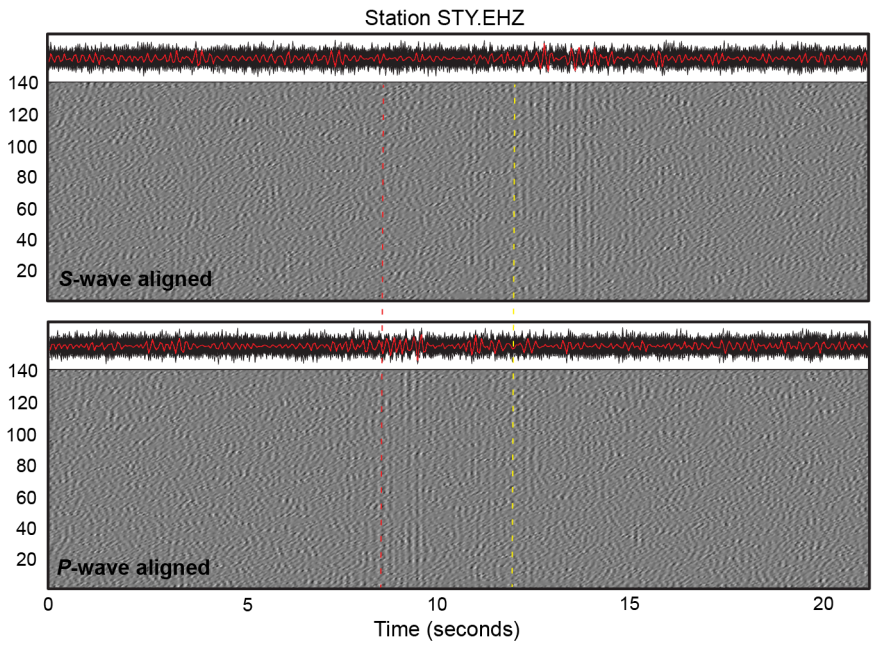

Figure 4.21: Grayscale plots of the LFE detections from ambient tremor (black traces) for component STY.EHZ, aligned by cross-correlation to the *S* wave (top), and aligned by cross-correlation to the *P* wave (bottom). Yellow and red dashed lines show *S*-wave and *P*-wave arrivals respectively.

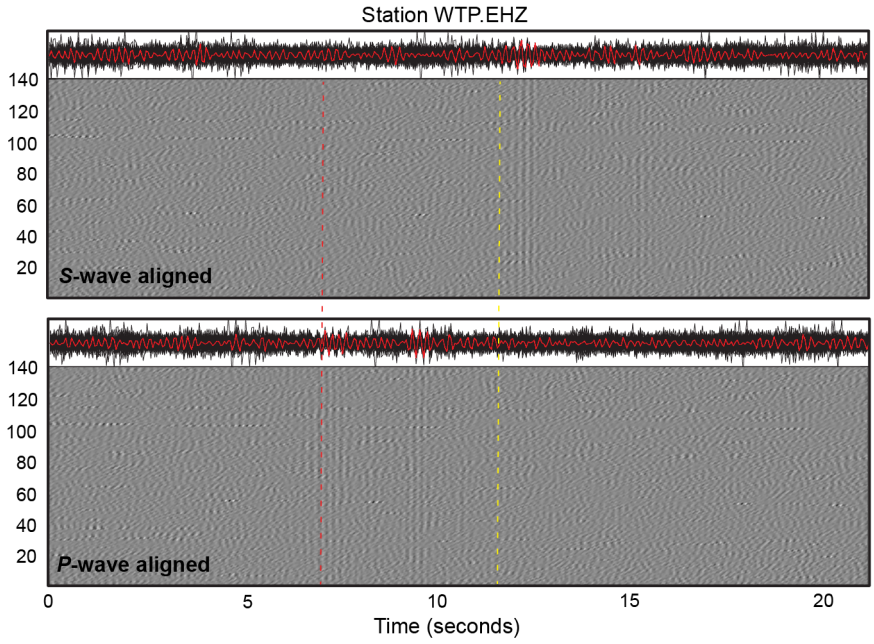

Figure 4.22: Grayscale plots of the LFE detections from ambient tremor (black traces) for component WTP.EHZ, aligned by cross-correlation to the *S* wave (top), and aligned by cross-correlation to the *P* wave (bottom). Yellow and red dashed lines show *S*-wave and *P*-wave arrivals respectively.

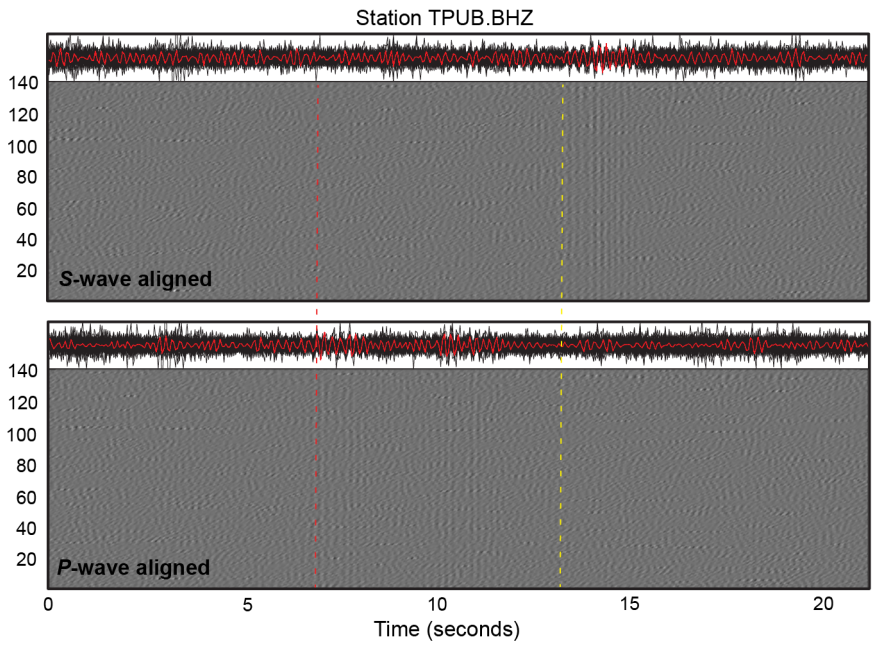

Figure 4.23: Grayscale plots of the LFE detections from ambient tremor (black traces) for component TPUB.BHZ, aligned by cross-correlation to the *S* wave (top), and aligned by cross-correlation to the *P* wave (bottom). Yellow and red dashed lines show *S*-wave and *P*-wave arrivals respectively.

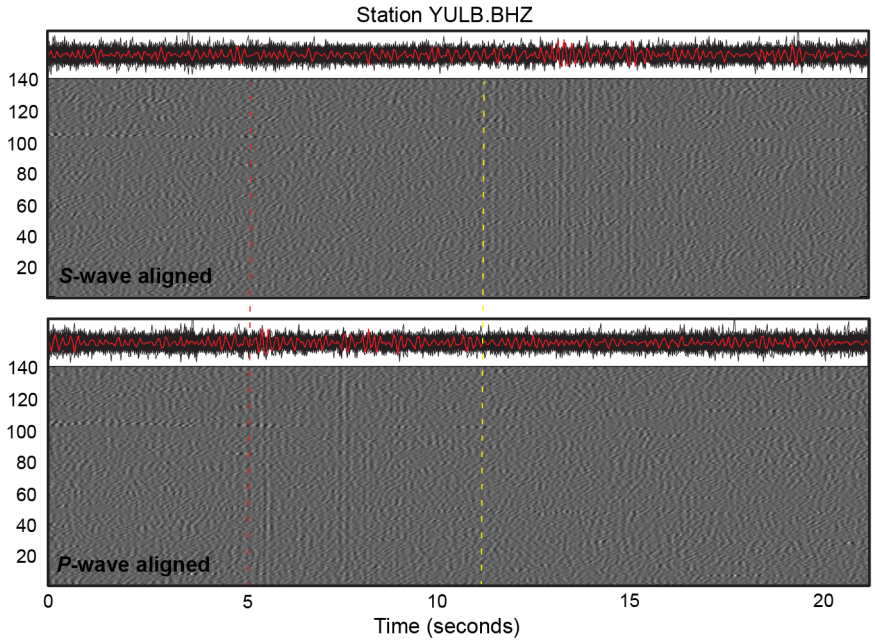

Figure 4.24: Grayscale plots of the LFE detections from ambient tremor (black traces) for component YULB.BHZ, aligned by cross-correlation to the *S* wave (top), and aligned by cross-correlation to the *P* wave (bottom). Yellow and red dashed lines show *S*-wave and *P*-wave arrivals respectively.

Using cross-correlation to find relative arrival times we are able to find clear *P*-wave arrivals for the LFE detections prior to the *S*-wave arrival on each of the stations. The *P*-waves that emerge from the cross-correlation alignment are in good agreement with the times listed in Table 4.2, and this is shown from the red and yellow dashed lines in Figures 4.19 to 4.24 for the stations analyzed. This result strongly suggests that the location of the LFEs found during the ambient tremor data is in the same general area as the earthquakes used to find the P-wave information of the LFEs.

As mentioned previously, the detections used to create the gray scale plots shown above are detections found during the ambient tremor of January 19, 2009. These detections are shown in the bottom plot of Figure 4.25 as the result for the associated stations used in the analysis.

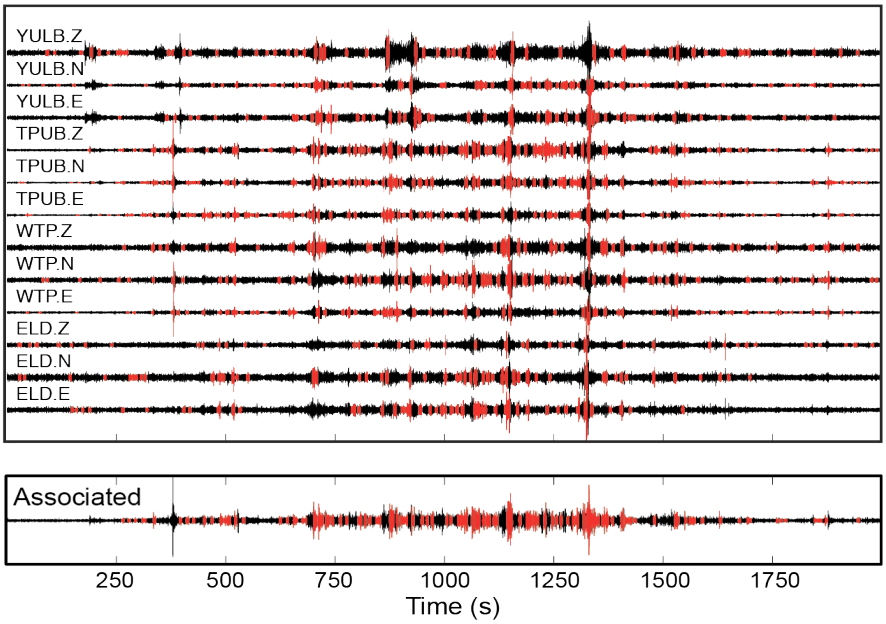

Figure 4.25: Detections found during tremor of January 19 from the analysis. Top plot shows detections found on each station independently and bottom plot shows the result for the associated stations above.

Using the relative arrival times from the cross-correlations as previously explained, we have located these detections using the double-difference earthquake hypocenter location technique (hypoDD) with both relative times from *P*- and *S*- wave by using the information from all available components. These locations are shown below in blue circles (Figure 4.26).

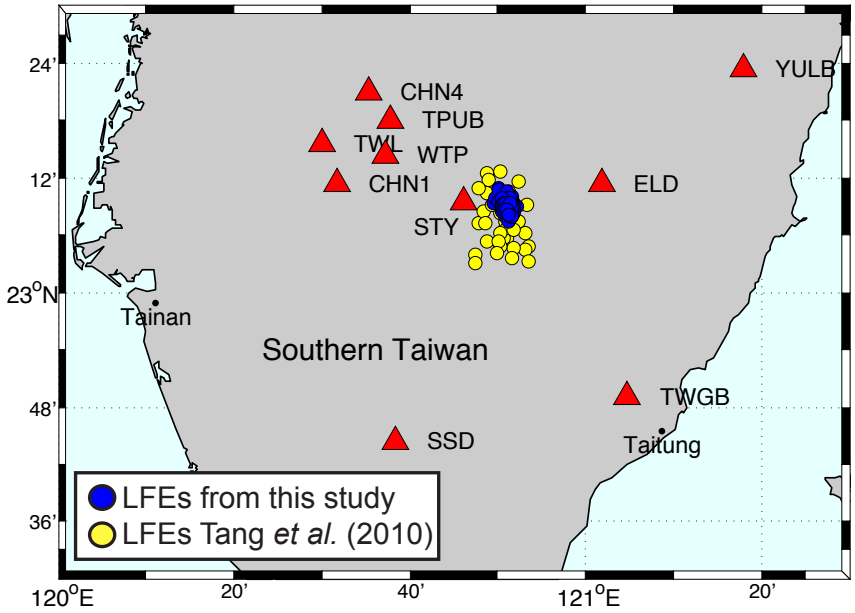

Figure 4.26: Detection locations for the ambient tremor (blue dots) during January 19, 2009 overlain on the result from Tang *et al.* (2010) for LFEs found during the triggered tremor of Nias earthquake of 2005 (yellow dots).

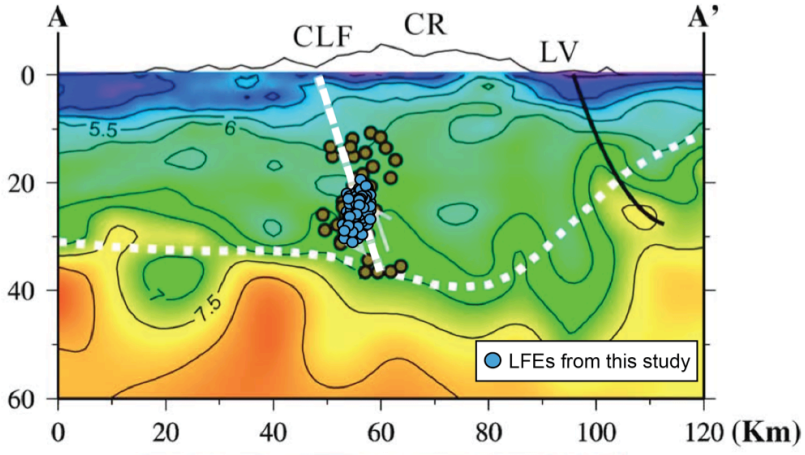

Figure 4.27: Cross-section of detection locations for the ambient tremor (blue dots) during January 19, 2009 overlain on the result from Tang *et al.* (2010) for LFEs found during the triggered tremor of Nias earthquake of 2005 (yellow dots). AA' is the same as in Figure 4.2. White thick dotted line represent the estimated projection of the Chaochou-Lishan fault (CLF), CR denotes the Central Range and LV denotes the Longitudinal Valley suture.

The locations for LFEs during the ambient tremor analyzed here show a more compact cluster compared to the previously found LFEs from the 2005 triggered tremor, but the general location area is very similar for both (Figure 4.26). The cross section shown in Figure 4.27 was obtained from Tang *et al.* (2010) and it is perpendicular to Taiwan's Central range. In this cross-section we can also see how the locations from our detections are more compactly clustered than the locations found by Tang *et al.* (2010).

As mentioned before, it has been suggested in previous studies that the source of the LFEs could be the deep extension of the Chaochou-Lishan fault. We observe a very linear feature in our locations, which could potentially be related to the fault plane. To understand this better we applied the same LFE template to other data from different days where ambient tremor is known to be present to see if we can map this planar feature more robustly. For this we use data from February, 28, 2010. We analyzed the 24 hours for this date using the same template created from the ambient

tremor from January of 2009 presented at the beginning of this chapter (Figure 4.6). We find a large number of detections during the full day; a total of 1135 detections and this are shown in the histogram in Figure 4.28.

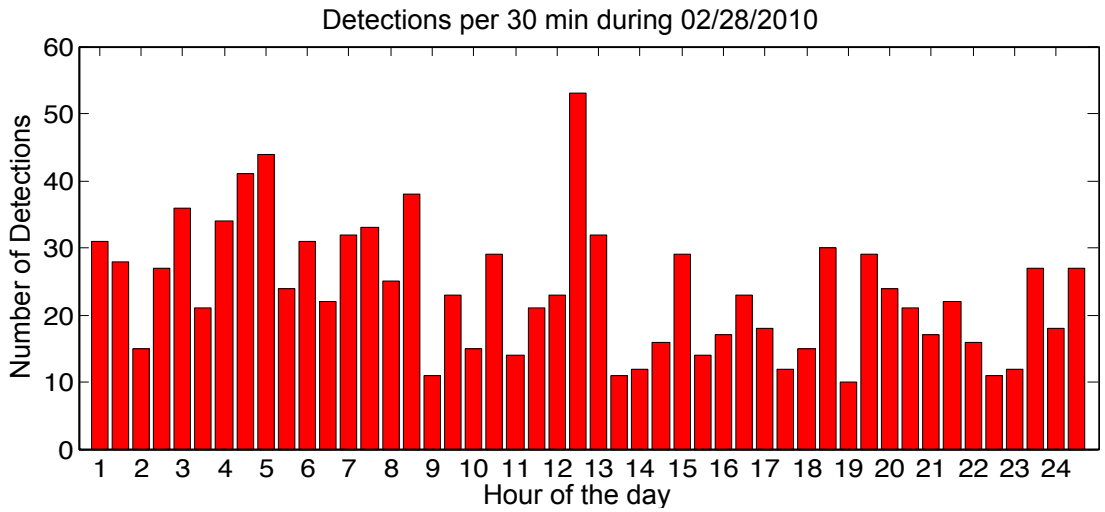

Figure 4.28: Histogram of number of LFE detections found during February 28, 2010 using the same LFE template from Figure 4.6. Each red bar of the histogram represents 30 minutes of data for this date.

We located these detections as before by using relative arrival times from cross correlation and find a similar clustering result to that shown for the ambient tremor of January 2009. This detections are shown in Figure 4.29, compared with the locations of detections found by Tang *et al.* (2010) during the 2005 triggered tremor. In cross section (Figure 4.30), we see again that the locations follow a linear trend between depths of 20 to 35 Km, delineating a linear feature parallel to the inferred projection of the Chaochou-Lishan fault.

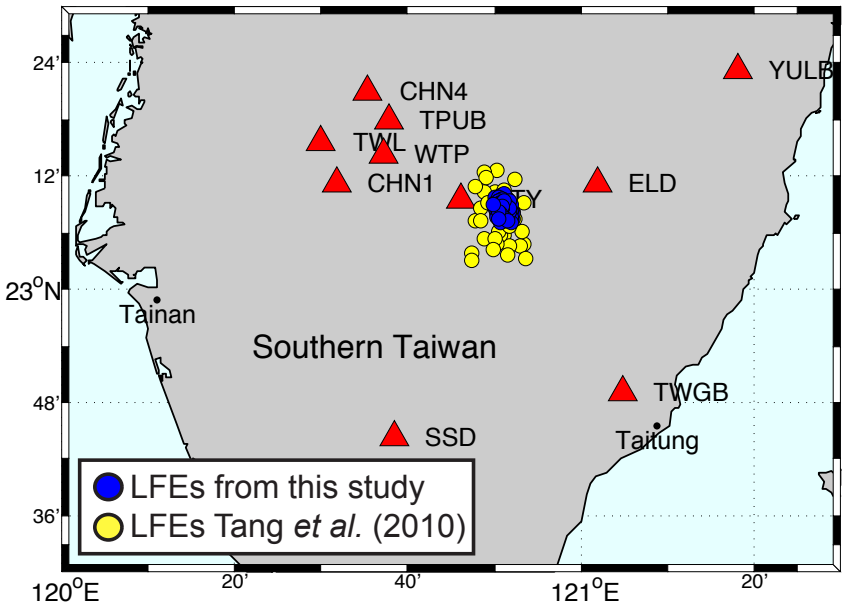

Figure 4.29: Detection locations for the ambient tremor (blue dots) during January 19, 2009 overlain on the result from Tang *et al.* (2010) for LFEs found during the triggered tremor of Nias earthquake of 2005 (yellow dots).

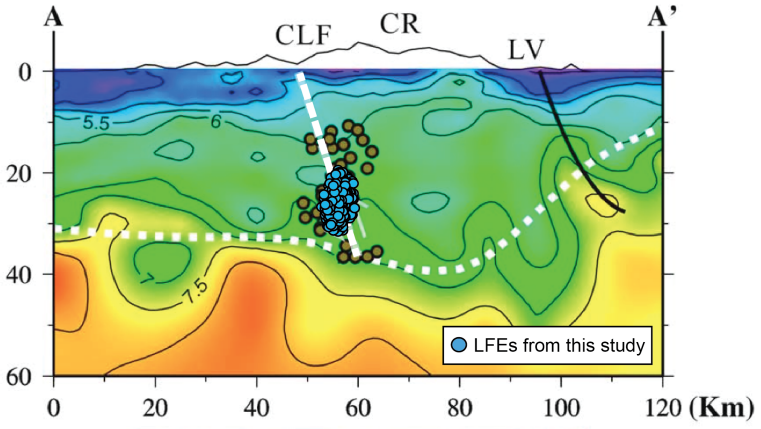

Figure 4.30: Cross-section of detection locations for the ambient tremor (blue dots) during January 19, 2009 overlain on the result from Tang *et al.* (2010) for LFEs found during the triggered tremor of Nias earthquake of 2005 (yellow dots). AA' is the same as in Figure 4.2. White thick dotted line represent the estimated projection of the Chaochou-Lishan fault (CLF), CR denotes the Central Range and LV denotes the Longitudinal Valley suture.

Since we can compare to the detections found by Tang *et al.* (2010) for the tremor triggered by the March 28, 2005 Nias earthquake, we also wanted to locate the detection we have found for this same event. For the detections found during the triggered tremor using the template created from the ambient tremor of January 2009, we locate these events, again by using relative arrival times from cross-correlation. For this time period, the only available data are the vertical components of the 6 stations that show the tremor clearly. We use only these 6 components to try to locate the detections found. These stations are CHN1, ELD, SSD, WTP, TPUB, and YULB. The locations found for these detections are shown in Figure 4.31 and we can see that they cover a larger area than the locations found for the ambient tremor and do not show a cluster as before. From the cross-section in Figure 4.32 we can see that the locations follow a linear feature, this time mostly perpendicular to the implied projection of the Chaochou-Lishan fault denoted as the white line.

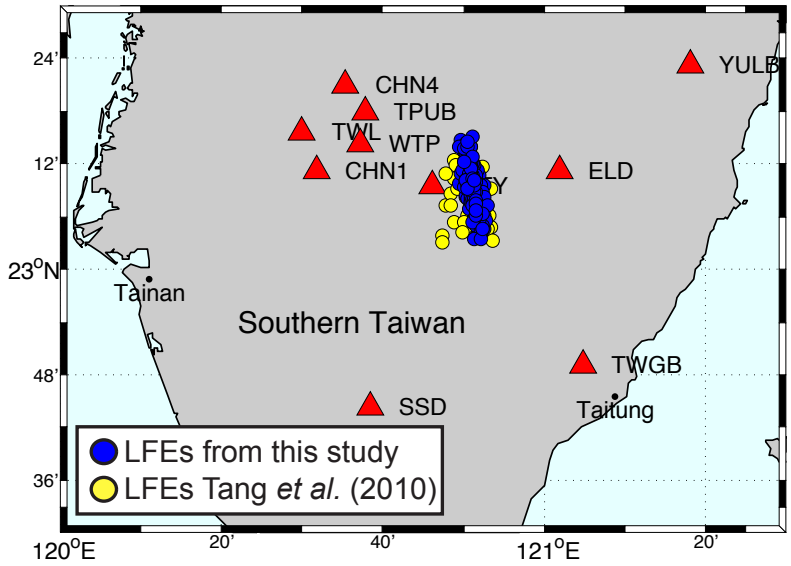

Figure 4.31: Detection locations for the triggered tremor (blue dots) during March 28, 2005 overlain on the result from Tang *et al.* (2010) for LFEs found during the same triggered tremor of Nias earthquake of 2005 (yellow dots).

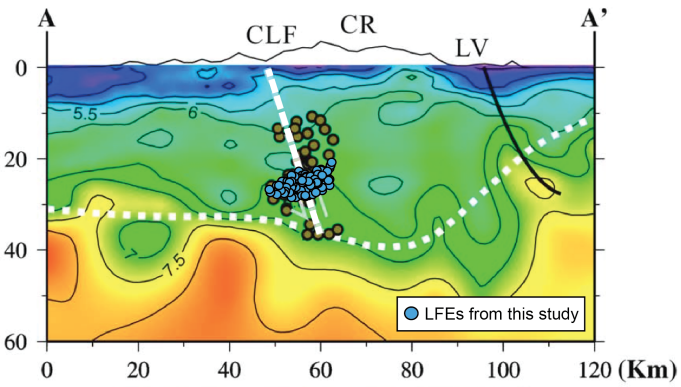

Figure 4.32: Cross-section of detection locations for the triggered tremor (blue dots) during March 28, 2009 overlain on the result from Tang *et al.* (2010) for LFEs found during the same triggered tremor of Nias earthquake of 2005 (yellow dots). AA' is the same as in Figure 4.2. White thick dotted line represent the estimated projection of the Chaochou-Lishan fault (CLF), CR denotes the Central Range and LV denotes the Longitudinal Valley suture.

We can also see from a cross-section, parallel to latitude how these locations are much less clustered than before, staying around the 25 km depth (Figure 4.33). Since we were only able to use the vertical component in this part of the analysis, we believe that the locations obtained are most likely biased by the station coverage used. To test this we located the events found during the first three hours of data from February 28, 2010 previously analyzed using all three components.

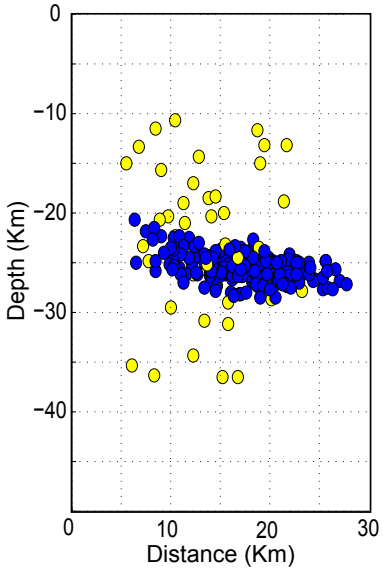

Figure 4.33: Cross-section parallel to line of latitude for the locations of LFE detections during the triggered tremor of March 28, 2005 from this study (blue dots), compared to the result from Tang *et al.* (2010) for LFEs found during the same triggered tremor of Nias earthquake of 2005 (yellow dots).

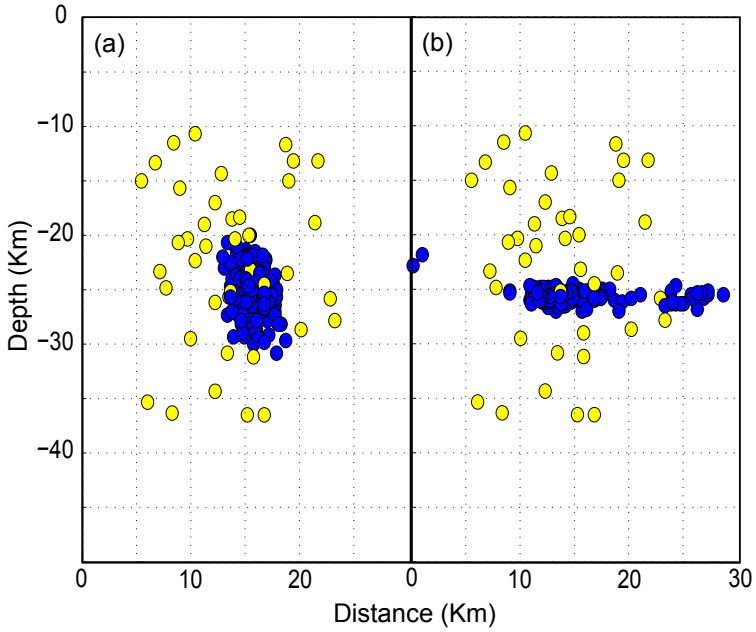

Figure 4.34: Cross-section parallel to latitude for the locations of LFE detections during the first three hours of data from February 28, 2010 (blue dots), compared to the result from Tang *et al.* (2010) for LFEs found during the triggered tremor of 2005 (yellow dots). (a) Locations using all components available, (b) locations using only the vertical components available during the 2005 triggered event.

We can see very clearly from Figure 4.34 how the locations for the first three hours of data from February 28, 2010 using all components show a more clustered result that increase the depths from 20 to 30 Km (Figure 4.34a). Whereas the locations using only the vertical component of the six stations available tend to stretch out horizontally around the 25 Km line (Figure 4.34b) suggesting this result is biased by the station coverage as well as the fact that the relative arrival times for the *S* waves obtained from cross-correlation are probably not as reliable as the result obtained by including the horizontal components in the analysis.

4.4 Discussion and Conclusions

After applying the PageRank algorithm to tremor data from Taiwan, we find that LFE templates created from ambient tremor during January 2009 are very similar to LFE templates within triggered tremor during the 2005 Nias earthquake. We also showed that using the LFE templates from either event, we can detect LFEs within most tremor bursts during the triggered tremor of 2005. This similarity between templates strongly suggests that the repeating signal recovered from both events is coming from the same general area and that I can recover a strong signal by applying the PageRank algorithm.

As for the Hikurangi subduction zone in New Zealand and the Nankai Trough in Japan, we created histograms of the PageRank values for the tremor and find that the distributions tend towards the higher values suggesting a large number of repeating signals within the tremor, validating once more the efficiency of our method to detect the LFEs.

Finally, we compared the LFE template from the ambient tremor to local, small earthquakes located to a similar area of the tremor. After cross-correlating the templates with the earthquakes and aligning them according to the cross-correlation we find that the *S*-wave of the templates is very similar to the *S*-wave of the earthquakes. This strongly suggests that the repeating signal we find is generated near the earthquakes and with similar mechanism. To test this statement further, we used the relative *P*-wave arrivals from the local earthquakes to cross-correlate the LFE detections using this relative time as a focus. We find that the *P*-wave arrival times also match the LFE *P*-wave arrival, as we are able to recover a clear arrival during that time for all 6 stations analyzed. This approach has helped us obtain clear *P*- and *S*-wave arrivals, which we used to find relative arrival times for locating the LFEs found during ambient tremor.

Using this approach to find the *P*-wave arrival, we apply it to a longer data set of 24 hours during February 28, 2010 where tremor is known to occur, as well as the ambient tremor of January 19, 2009 previously analyzed. We locate the detections found during both of these data sets and show that LFEs for both dates locate to a more compact cluster compared to previous results of LFEs detected during the triggered tremor of the March 28, 2005 Nias earthquake (Tang *et al.*, 2010). The cluster that we locate seems to follow a linear feature, which seems to be parallel to the inferred projection of the Chaochou-Lishan fault, suggesting this could be an asperity patch of this fault. We also show that using only the vertical components of the stations available for the analysis we can not resolve the locations of the LFEs detected, for neither the ambient tremor of 2010 nor the tremor triggered by the March 28, 2005 Nias earthquake. The station coverage as well as the fact that the relative arrival times are lees robust due to the lack of horizontal components bias the result of the locations showing locations that stretch out following the 25 km depth line.

CHAPTER 5

Mapping Amplitude Decay from Tremor PGA and PGV in the Cascadia Subduction Zone

The Cascadia subduction zone, where the Juan de Fuca plate subducts beneath the North America plate, is located in the northwestern United States and southwestern Canada. It extends 1100 km from Cape Mendocino, California, to northern Vancouver Island, British Columbia. It is locked mainly offshore, except for central Oregon, where the locked zone extends inland (Figure 5.1). Most of Oregon and southwest Washington is undergoing a clockwise rotation with respect to North America at a rate of 0.4-1.0˚/Myr for 10-15 Ma, and on Vancouver Island the motion is more aligned with the Juan de Fuca-North America relative plate motion (McCaffrey *et al.*, 2007). The dip of the slab varies as it extends inland from 2˚-7˚ offshore to 12˚ onshore (Parsons *et al.*, 1998).

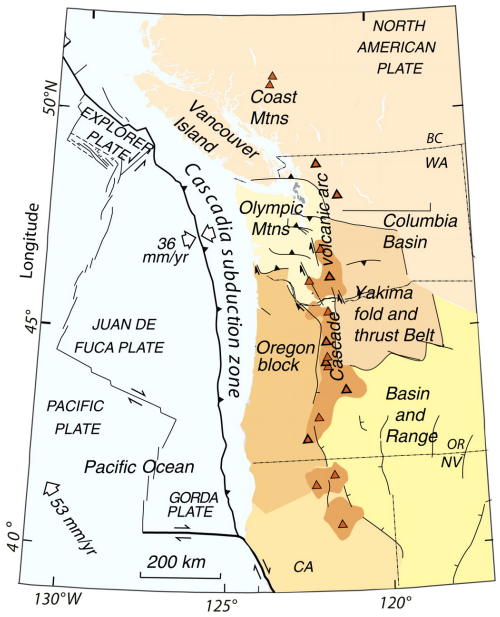

Figure 5.1: The Cascadia subduction zone. Major provinces (shaded areas and italicized labels) are distinguished by the dominant deformation style and rates, stress fields that drive the deformation, and geologic histories and structures. Arrows straddling major plate boundaries indicate relative plate motions, and other solid curves schematically show trends and types of crustal faults within the North American plate. Triangles denote volcanoes (Gomberg *et al.*, 2010).

This subduction zone is thought to rupture the full margin with Mw~9 events every five hundred years (Atwater, 1987; Satake *et al.*, 1996; Atwater and Hemphill-Haley, 1997). Geological and historical evidence show consistently that the last large earthquake on this subduction zone occurred in January, 1700 with a magnitude that may have been as large as Mw 9.0 event (Atwater and Moore, 1992; Satake *et al.*, 1996; Satake *et al.*, 2003; Atwater *et al.*, 2005). Initial viscoelastic models used for the Cascadia subduction zone determined that the locked zone is mostly fully locked for 60 km down dip of the trench, at the plate boundary, with another 60 km of transition zone after that (Dragert *et al.*, 1994).

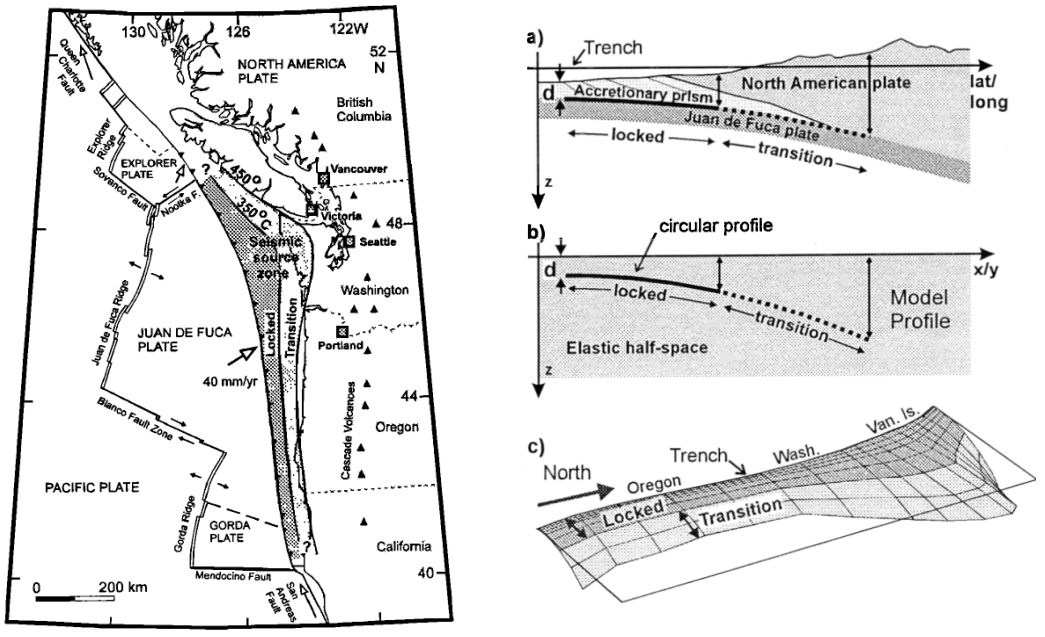

Figure 5.2: From Hyndman and Wang (1995) The Cascadia subduction zone on the left plot. Locked and transition zones estimated from dislocation modeling. Down dip limits coincide approximately to the 350 °C and 450 °C isotherms. Right plot shows a cross section of the subduction zone at depth (Flück *et al.*, 1997).

As mentioned in Chapter 1, a large section of the subduction zone is slipping down dip of the locked zone around 25 to 45 km depths. This region was initially

thought to be slipping steadily, then episodically without any accompanying seismic signal, before the discovery of tremor as part of ETS events (Linde *et al.*, 1988; Dragert *et al.*, 2001).

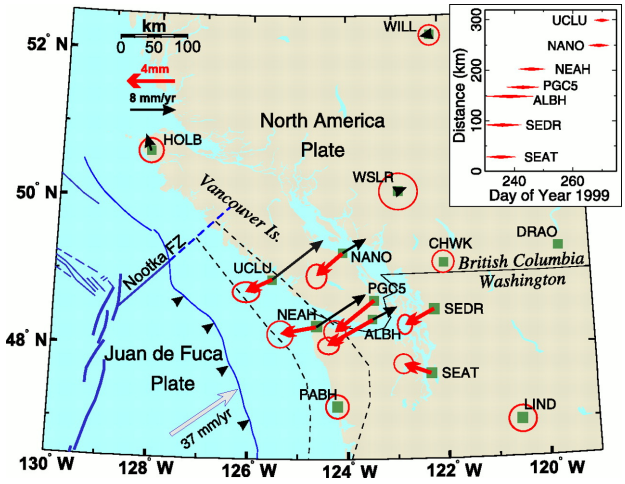

Figure 5.3: From Dragert *et al.* (2001). Reversal of the long term in GPS-measured surface velocities during slow slip events. Red arrows show displacements (wrt DRAO) due to the slip event. Black arrows show 3- to 6-year average GPS motions with respect to DRAO. Dashed lines show nominal down-dip limits of the locked and transition zones from the model of Flück *et al.* (1997)

It was here where these events where denoted ETS (Rogers and Dragert, 2003) (Figure 1.1) and where it was suggested that both tremor and slip are a manifestation of the same process at depth. To date, more than 39 slow slip events have been recognized since 1997. They still follow a consistent periodicity in the Puget Sound region, usually last several weeks and accumulate approximately 5 mm of transient slip (Szeliga *et al.*, 2008). Here, all slow slip events are accompanied by tectonic tremor (Kao *et al.*, 2009; Gomberg *et al.*, 2010). Initially, the tremor signals were located to a wide range of depths, and attributed to fluid movements along the subduction zone (Kao *et al.*, 2005; McCausland *et al.*, 2005). But more recently, they have been shown to locate along the plate interface (Brown *et al.*, 2009; La Rocca *et al.*, 2009).

Given that tremor in Cascadia co-locates with the slip distributions during the ETS events (Figure 5.4), different ideas of where the locked zone might end have been explored. Using variable-sized subfaults to estimate the distribution of slow slip, Chapman and Melbourne (2009) found that the GPS data delineate the slip distributions during the ETS events between 25- and 40- km depths of the plate interface. This falls within the previously denoted transition zone (Hyndman and Wang, 1993; Dragert *et al.*, 1994; Flück *et al.*, 1997) shown in Figure 5.2. Applying a different method, where the velocities are estimated using a block/fault model, McCaffrey (2009) found the slip distributions to be between 15- to as deep as 70- km depth contours of the fault. As a different approach, Bartlow *et al.* (2011) have focused on the spatio-temporal relationship between tremor and slip themselves, showing that tremor is actually caused by the slip during a large 2009 ETS event, suggesting that slip can be used as a proxy for slip. But there is evidence that not all is understood, as some slip events seem to occur ahead of tremor or tremor ahead of slip (Wech and Bartlow, 2014).

Given the uncertainty of the extent of the locked zone in the Cascadia subduction zone, the spatio-temporal correlation between slip an tremor, as well as the evidence of recurring Mw~9 earthquakes that can produce strong ground motions north to south, in highly populated areas such as Seattle and Portland (Atwater, 1987; Satake *et al.*, 1996; Atwater and Hemphill-Haley, 1997), it is important to characterize the seismic hazard in this area as accurately as possible.

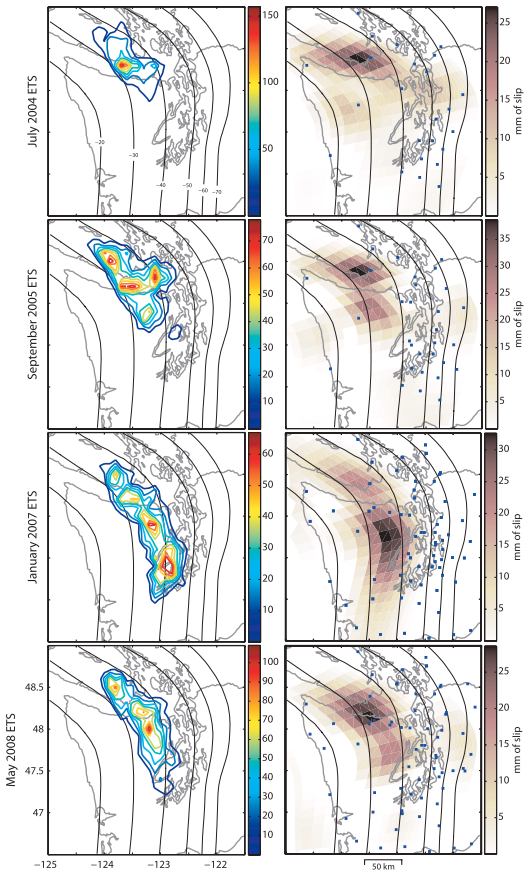

Figure 5.4: From Wech *et al.* (2009). Summed tremor epicenter locations and slip distributions for four different ETS events in Cascadia, blue squares are GPS stations.

Ground motion prediction equations (GMPEs) that predict the strength and variability at a site for a given earthquakes are a central part of hazard analysis, but earthquake data needed for these calculations are sparse in Cascadia (Atkinson and Boore, 1997). Given the periodicity of ETS events here and the large amounts of tremor associated to them, there are large quantities of tremor data available. Baltay and Beroza (2013) have taken advantage of these data and have shown that tremor can be used to predict linear path effects on strong ground motion because the weak waves in the tremor signal pass through and are affected by the same complex geometry as for large earthquakes. In this chapter we use Baltay and Beroza (2013) attenuation terms calculated from tremor, and their residual misfit to map the amplitude variability of tremor across the northern Cascadia subduction zone.

5.1 Attenuation from Tremor

Following Baltay and Beroza (2013), the anelastic attenuation parameter can be estimated directly from the observed inter-station differences in the PGA and PGV amplitudes observed. For event *i* and station *j* the amplitude can be represented as follows,

$$\ln A_{ij} = c1_i - c2R_{ij} - \ln R_{ij} \tag{5.1}$$

where *c1* describes the initial amplitude, *c2* is the attenuation parameter and R_{ij} the hypocentral distance. Using the differential ground-motion amplitudes, the attenuation term for stations 1 and 2 can be expressed as

$$c2 = \frac{\left(\ln A_{i1} - \ln A_{i2}\right) + \left(\ln R_{i1} - \ln R_{i2}\right)}{R_{i2} - R_{i1}} \tag{5.2}$$

Back-substituting to find *c1* for each event and considering an average station term S_j for each station, the expression for the *c2* term can be written

$$c2 = \frac{\ln A_{ij} - \ln S_j - c1_i + \ln R_{ij}}{-R_{ij}} \tag{5.3}$$

for each event *i* and station *j* (Baltay and Beroza, 2013).

Using equation 5.3, *c2* values were calculated for data from three different ETS events in Cascadia: August 2010, August 2011, and September 2012, using stations from the PBO borehole network. Figure 5.5 shows the events that were used for each of the three ETS events.

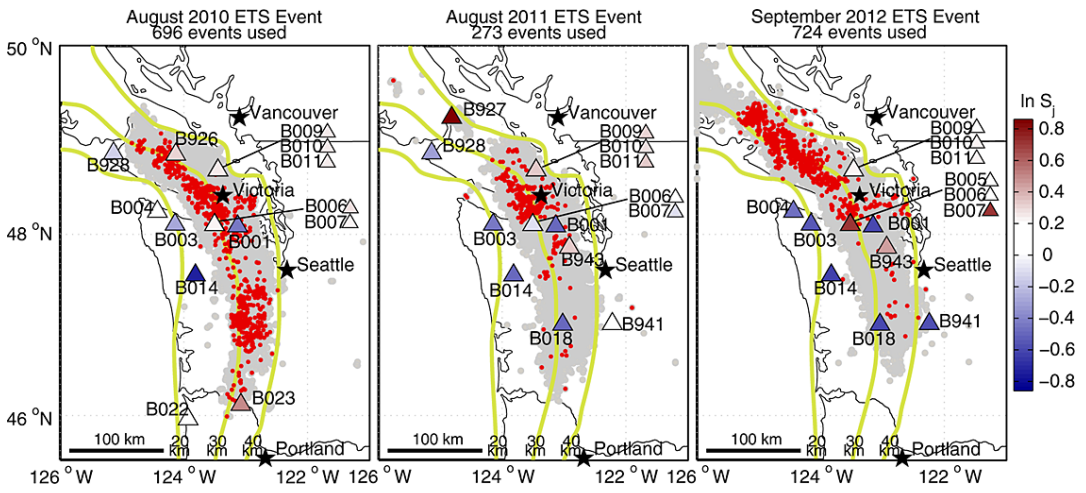

Figure 5.5: From Baltay and Beroza (2013). Locations of 5 min tremor events used (red dots) overlain on all available data (grey dots). Yellow lines show the plate interface (Audet *et al.*, 2010). Triangles show stations used, with color indicating the mean site/station term (S_j).

Baltay and Beroza (2013) measured the PGA, PGV and hypocentral distance to each station for each 5 min window of tremor, as determined by Wech and Creager (2008), during each of the three ETS events in 2010, 2011, and 2012. The attenuation term for all stations available during each of the three events is shown in Figures 5.6 to 5.8. Here the residual is plotted with respect to the mean *c2* of all the data used in the three events, which is 0.0071. In the color scale, zero is equal to the mean, red dots are *c2* values above the mean (stronger attenuation), and blue dots are *c2* values below the mean (weaker attenuation). Each plot has a total of 12 stations, some of which repeat between events and others only appear only for one event. The reason for the difference in stations is the varying spatial extent of tremor in the three sequences.

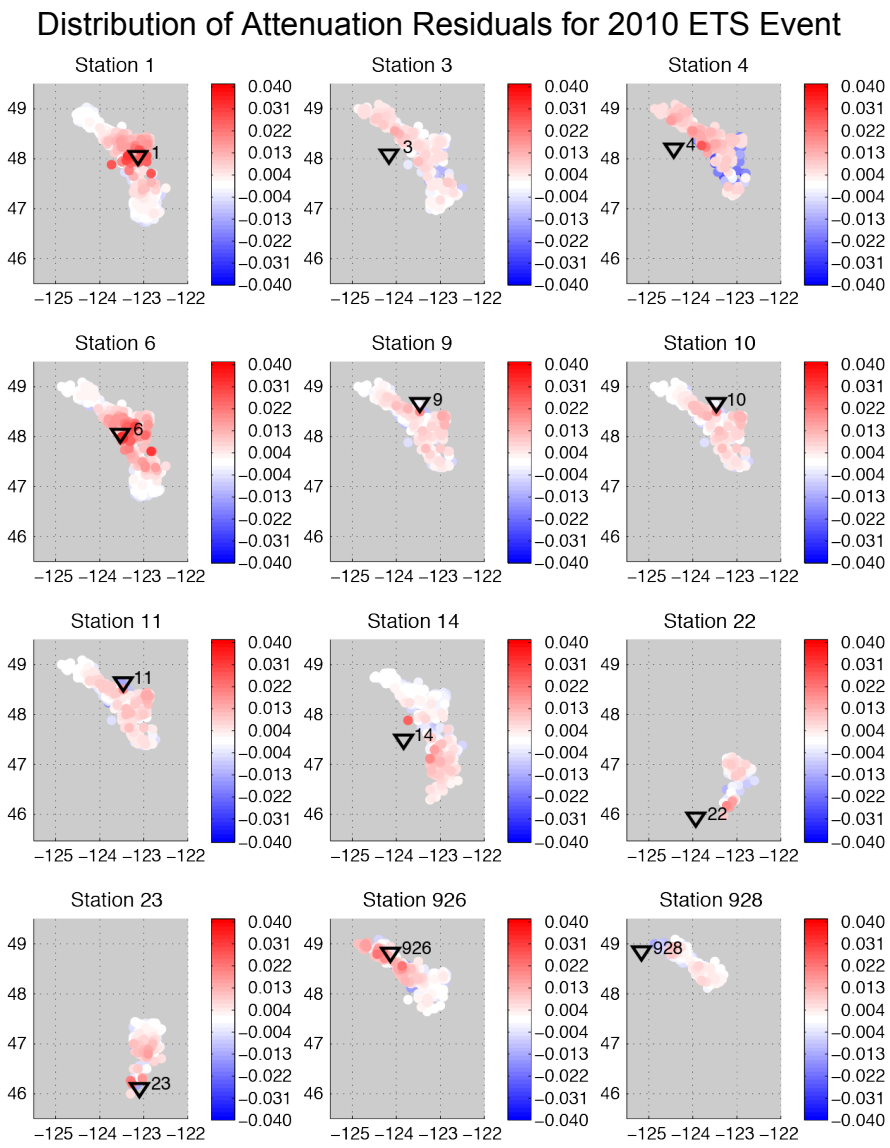

Figure 5.6: Distribution of attenuation residuals for 2010 ETS Event. Each plot shows the attenuation residuals for each of the 12 stations used for the analysis of the 2010 slow slip event. Color is plotted with respect to the mean.

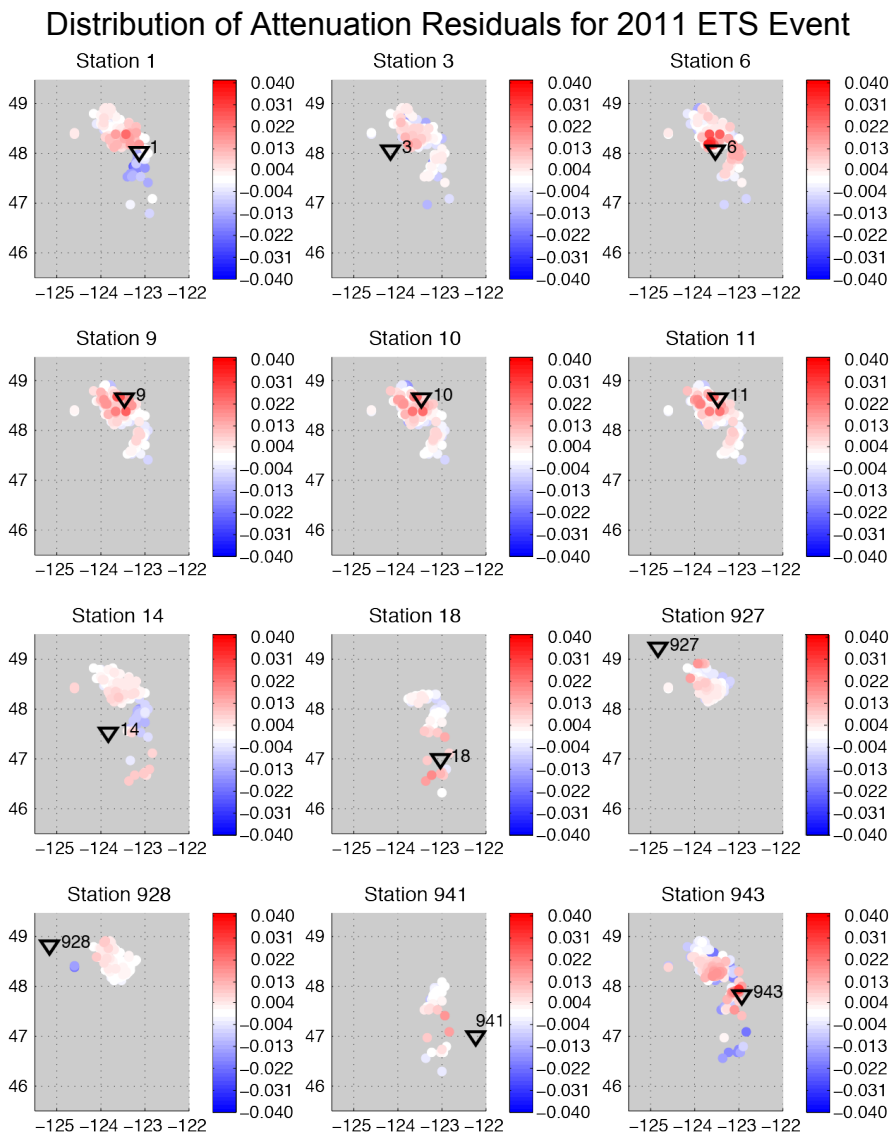

Figure 5.7: Distribution of attenuation residuals for 2011 ETS Event. Each plot shows the attenuation residuals for each of the 12 stations used for the analysis of the 2011 slow slip event. Color is plotted with respect to the mean.

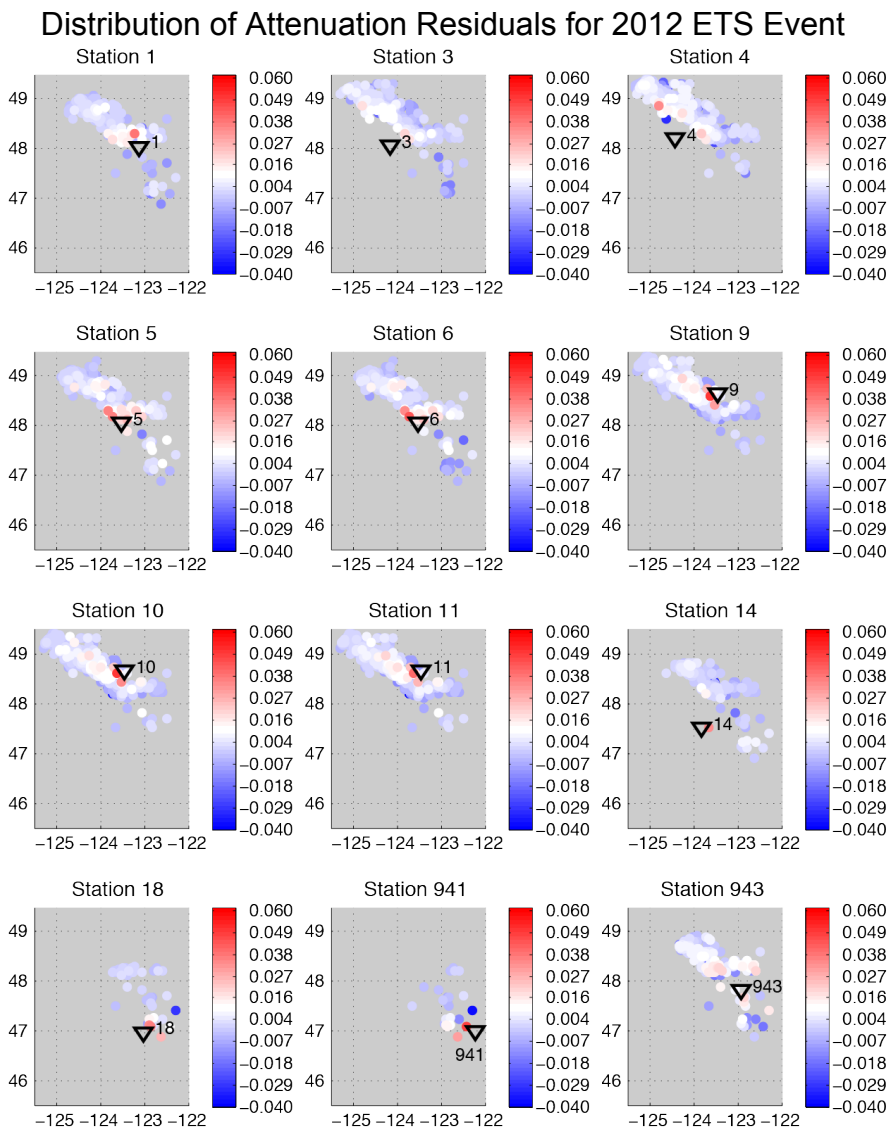

Figure 5.8: Distribution of attenuation residuals for 2012 ETS Event. Each plot shows the attenuation residuals for each of the 12 stations used for the analysis of the 2012 slow slip event. Color is plotted with respect to the mean.

We also analyzed the *c2* terms for each SSE for each station with respect to the hypocentral distance from the tremor source to the station. This helped reveal any possible systematics in the behavior at each station. These are plotted below (Figure 5.9 to 5.11), again color coded with respect to the mean.

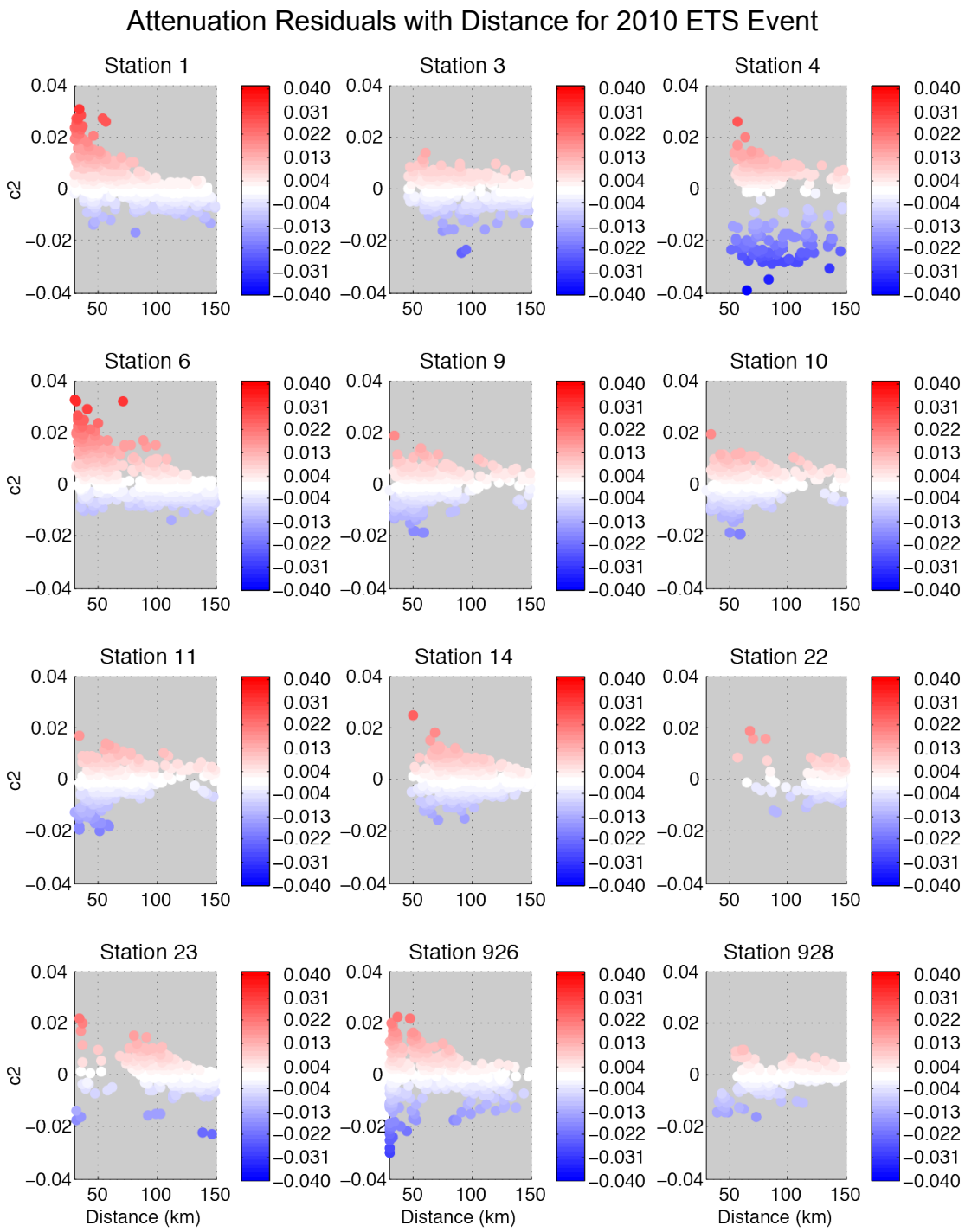

Figure 5.9: Attenuation residuals with distance for 2010 ETS event. Attenuation values with respect to epicentral distance to each station used in the analysis of the 2010 slow slip event. Color is plotted with respect to the mean.

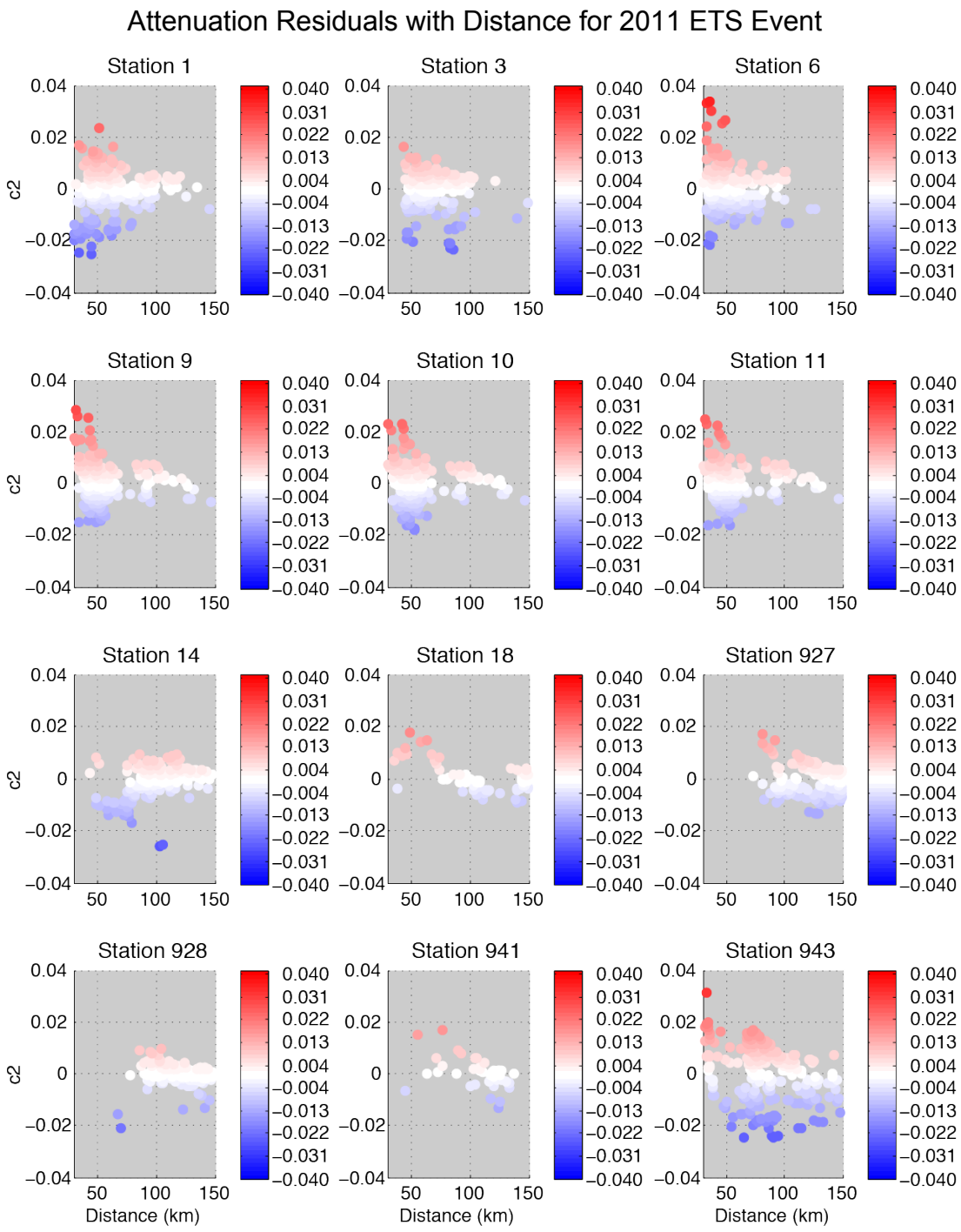

Figure 5.10: Attenuation residuals with distance for 2011 ETS event. Attenuation values with respect to epicentral distance to each station used in the analysis of the 2011 slow slip event. Color is plotted with respect to the mean.

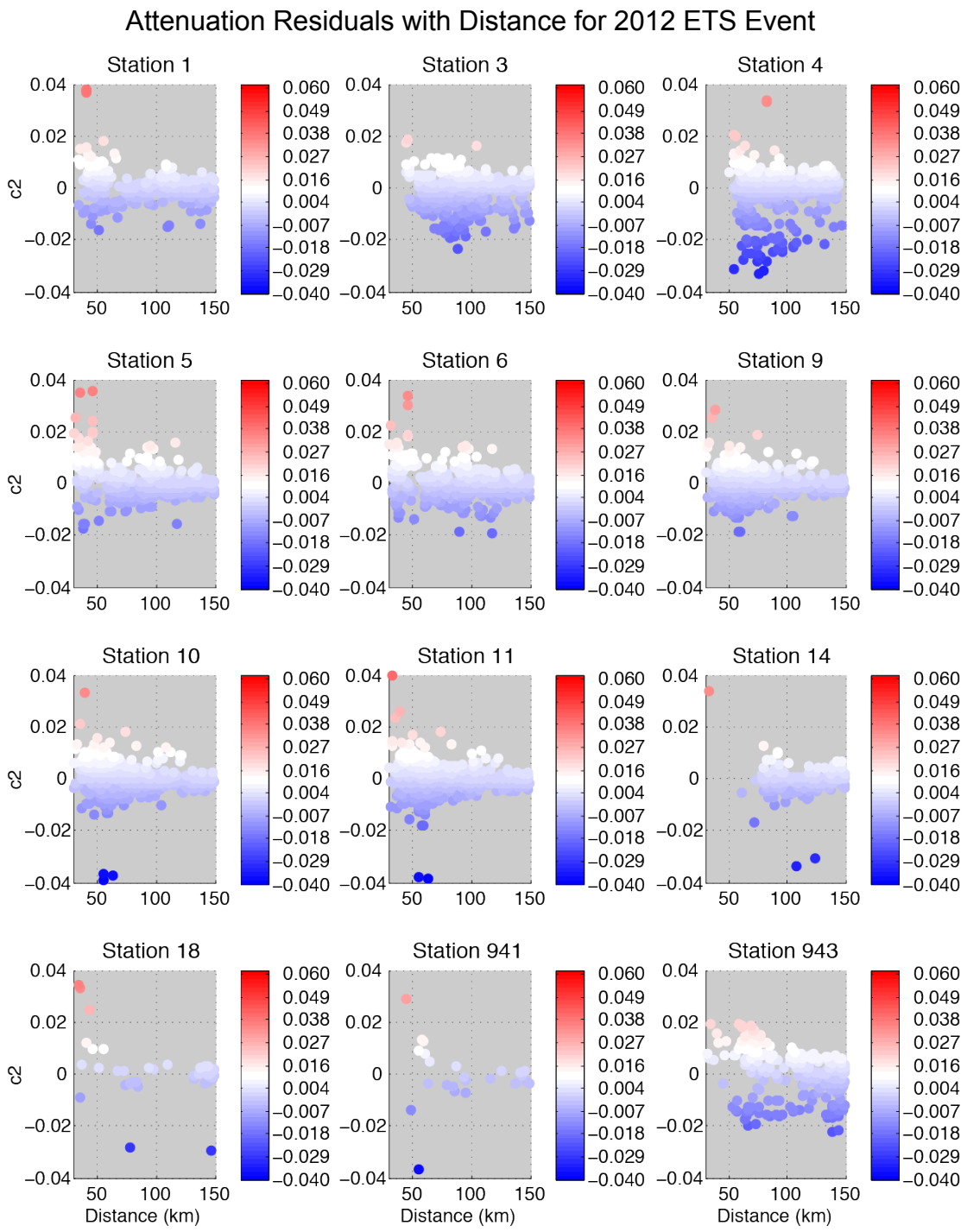

Figure 5.11: Attenuation residuals with distance for 2012 ETS event. Attenuation values with respect to epicentral distance to each station used in the analysis of the 2012 slow slip event. Color is plotted with respect to the mean.

Figures 5.9 to 5.11 reveal a consistent decrease in *c2* as the source-receiver distance increases. This behavior is particularly prominent on the stations that are located directly above the events, such as stations 1 and 6 for the 2010 SSE event (Figure 5.6), station 9-11 and 943 for the 2011 SSE event (Figure 5.7). This behavior is less prominent on stations farther from the event locations such as stations 3 and 14 observed in all three SSE events (Figure 5.6 to 5.8). This behavior seems to agree closely with calculations done by Yabe *et al.* (2014) for a synthetic test that represents a model with a thick weak attenuation layer overlain by a less attenuating layer, where for short distances they find higher values of *c2* and they decrease with distance. It is important to note here that station groups 5, 6 and 7, and station 9, 10, and 11 are co-located, and therefore show very similar results for each. Station 7, even though used by Baltay and Beroza (2013), has been omitted for our analysis due to inconsistent behavior during the 2012 SSE event.

To validate the results obtained for the attenuation values, we compare the attenuation values for repeated tremor events on co-located stations during each of the three ETS events.

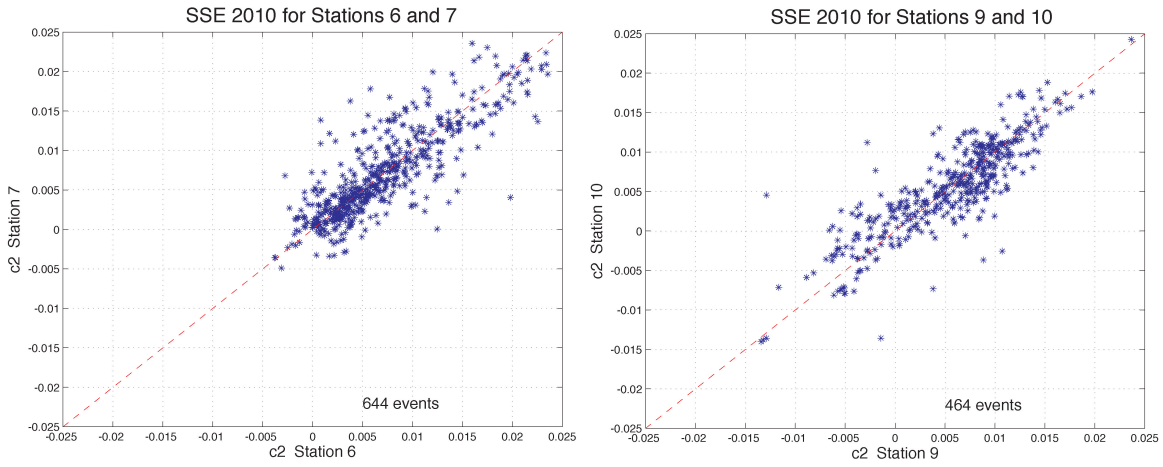

Figure 5.12: Comparison of repeated tremor events on different co-located stations during the 2010 SSE: Station 5 and 6 on the left, and 9 and 10 on the right. Red dash line represents the one-to-one relationship.

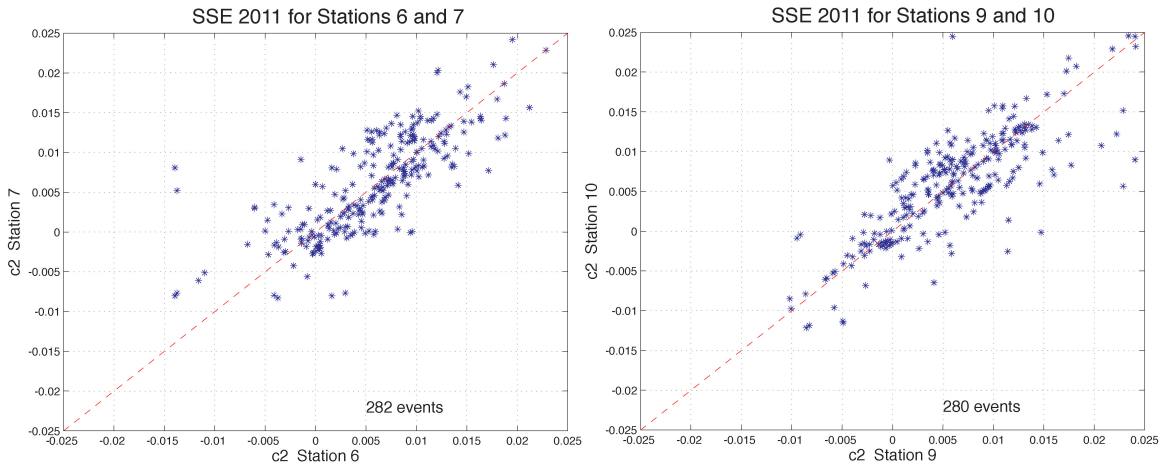

Figure 5.13: Comparison of repeated tremor events on different co-located stations during the 2011 SSE: Station 6 and 7 on the left, and 9 and 10 on the right. Red dash line represents the one-to-one relationship.

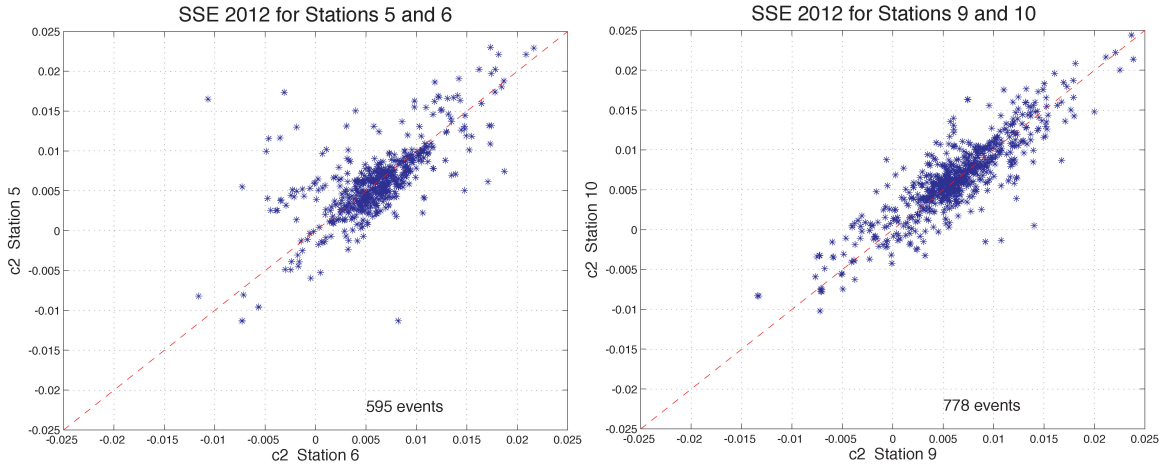

Figure 5.14: Comparison of repeated tremor events on different co-located stations during the 2012 SSE: Station 5 and 6 on the left, and 9 and 10 on the right. Red dash line represents the one-to-one relationship.

From Figures 5.12 to 5.14, it can be observed that co-located stations have very consistent attenuation values for each of the ETS events, closely following the one-to-one red dashed line. This validates the results obtained during each of the SSE events. If we compare common tremor events for all stations from each of the SSE event with the other two SSE events, we can see that this is not the case (Figure 5.15).

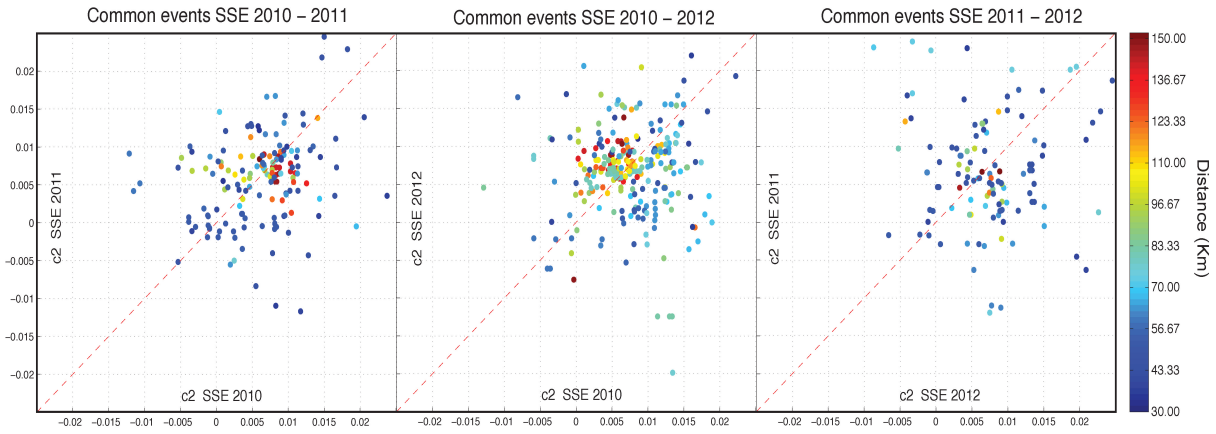

Figure 5.15: Comparison of attenuation values for common tremor events used in the analysis between SSEs. From left to right: (1) common events between SSE 2010 and 2011 (2) common events between SSE 2010 and 2012 (3) common events between SSE 2011 and 2012. Color represents hypocentral distance to the stations

Figure 5.15 shows a large scattering effect when we compare the common events, for each pair of SSE. Although these values seem to cluster around the mean value calculated from all the *c2* values used in the analysis, for all events (0.0071).

5.2 Moving Average of Attenuation terms

To understand the variability of *c2* values between the three ETS events we calculated a spatial average of *c2* for each event using all repeated stations. We calculate an average *c2* value for an area of 10 km radius and move it every 10 km to cover all the area where there are events happening during the three SSEs. Figures 5.16 to 5.22 show the moving average for all common stations during each of the SSE. Here, the *c2* values have been color coded with respect to the mean *c2* of all events. The red colors can be interpreted as *c2* above the mean (stronger attenuation), and the blue colors can be interpreted as *c2* below the mean (weaker attenuation).

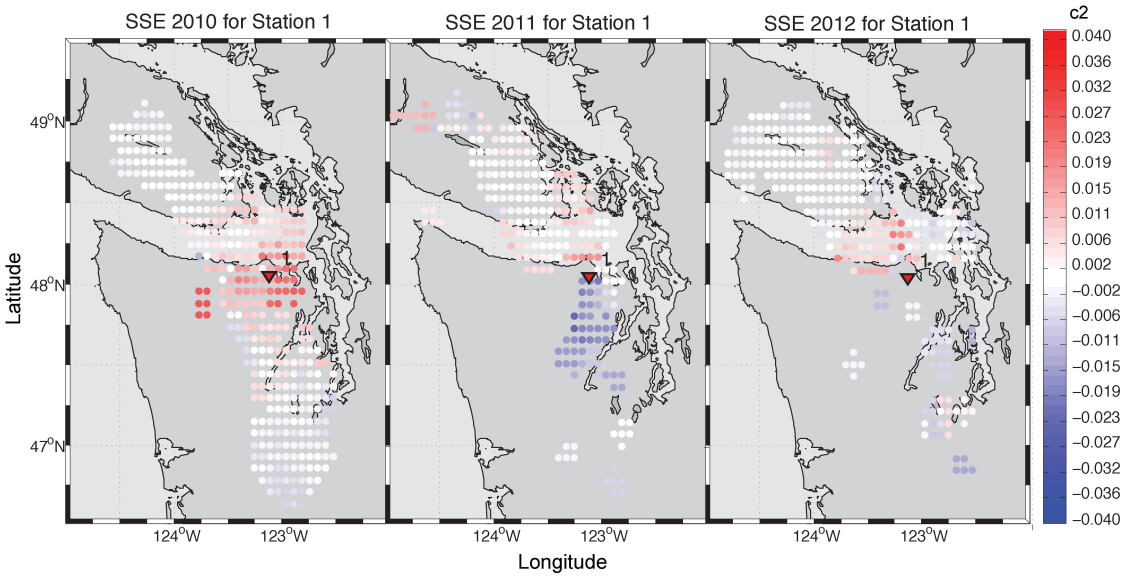

Figure 5.16: Moving average of *c2* for station 1 during the ETS events of 2010, 2011, and 2012. Color is plotted with respect to the mean.

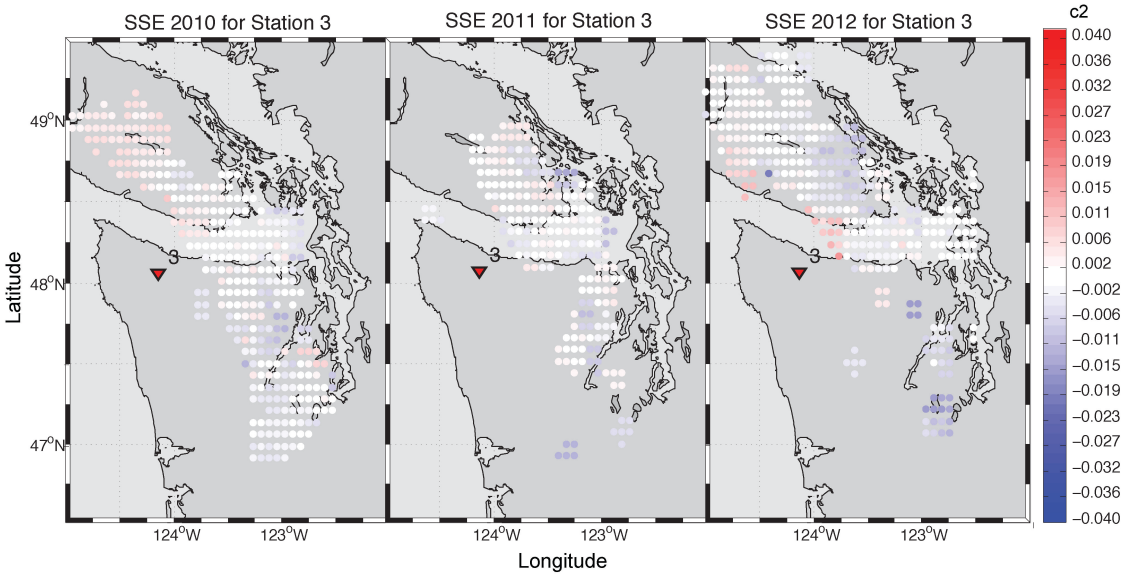

Figure 5.17: Moving average of *c2* for station 3 during the ETS events of 2010, 2011, and 2012. Color is plotted with respect to the mean.

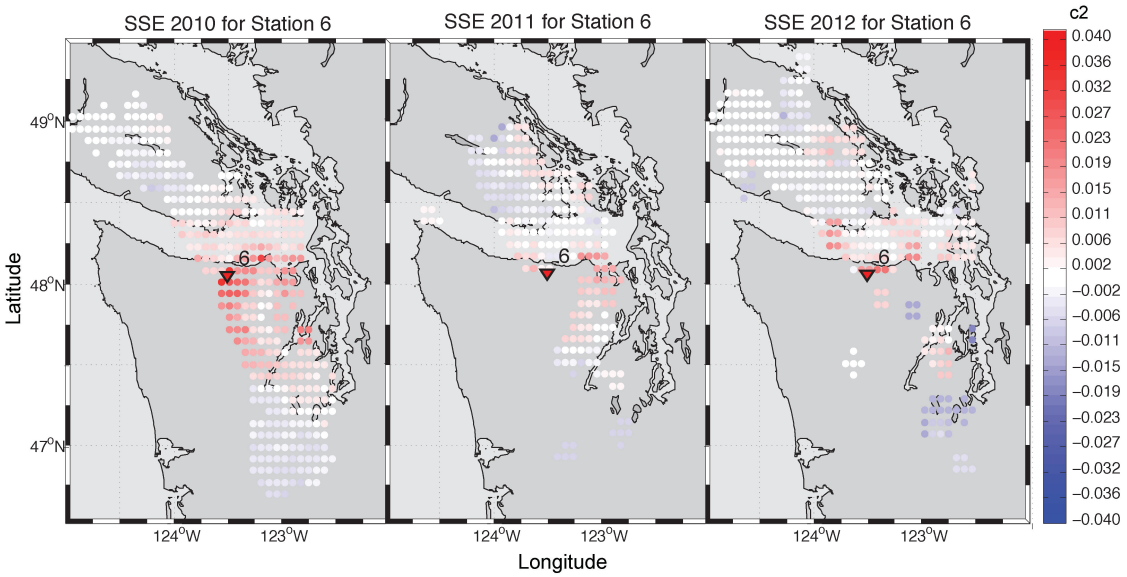

Figure 5.18: Moving average of *c2* for station 6 during the ETS events of 2010, 2011, and 2012. Color is plotted with respect to the mean.

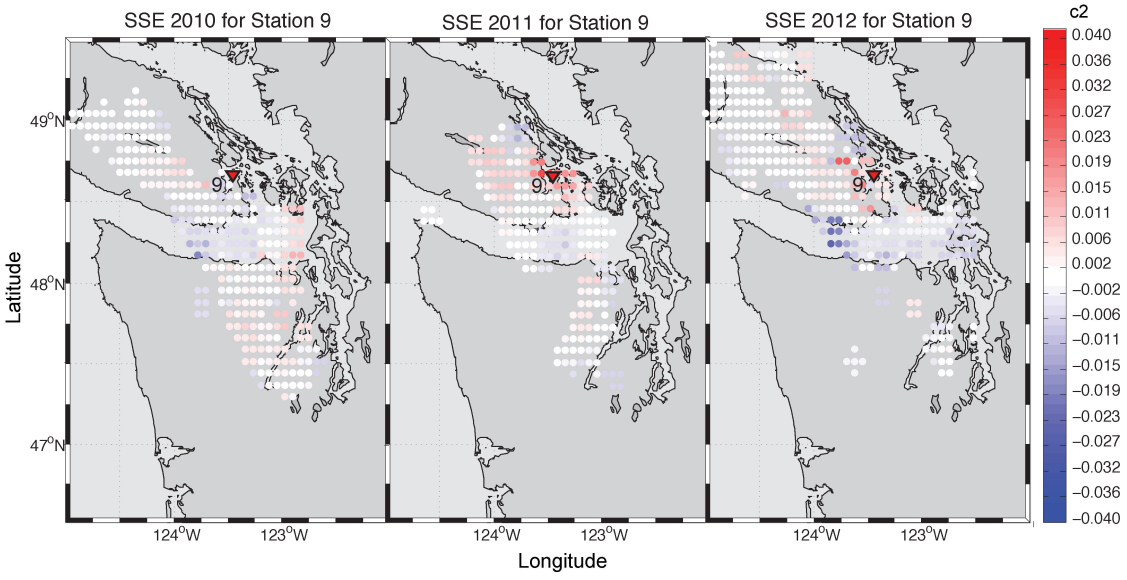

Figure 5.19: Moving average of *c2* for station 9 during the ETS events of 2010, 2011, and 2012. Color is plotted with respect to the mean.

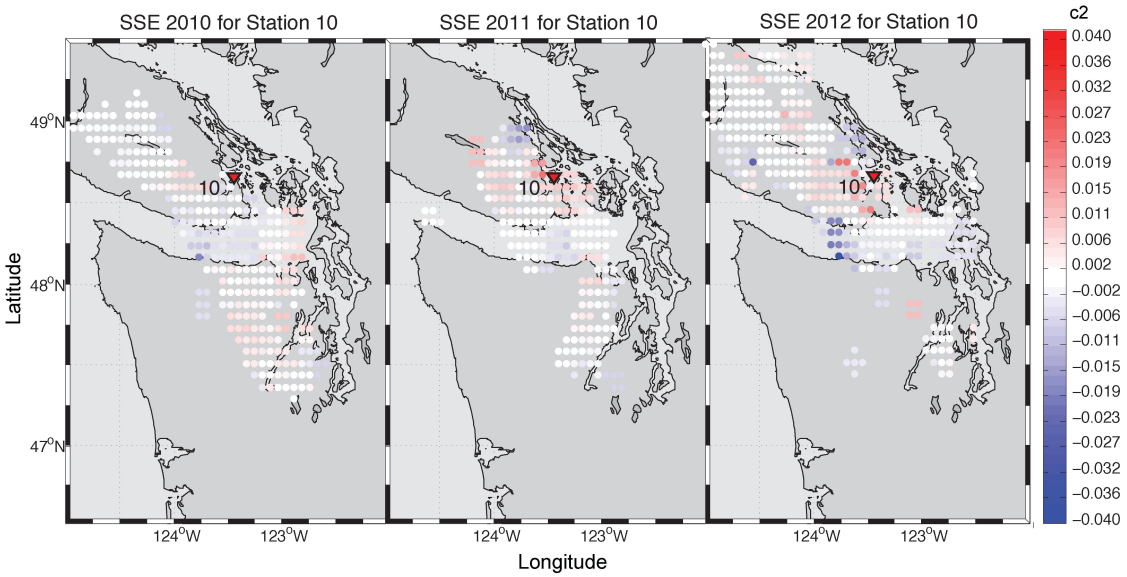

Figure 5.20: Moving average of *c2* for station 10 during the ETS events of 2010, 2011, and 2012. Color is plotted with respect to the mean.

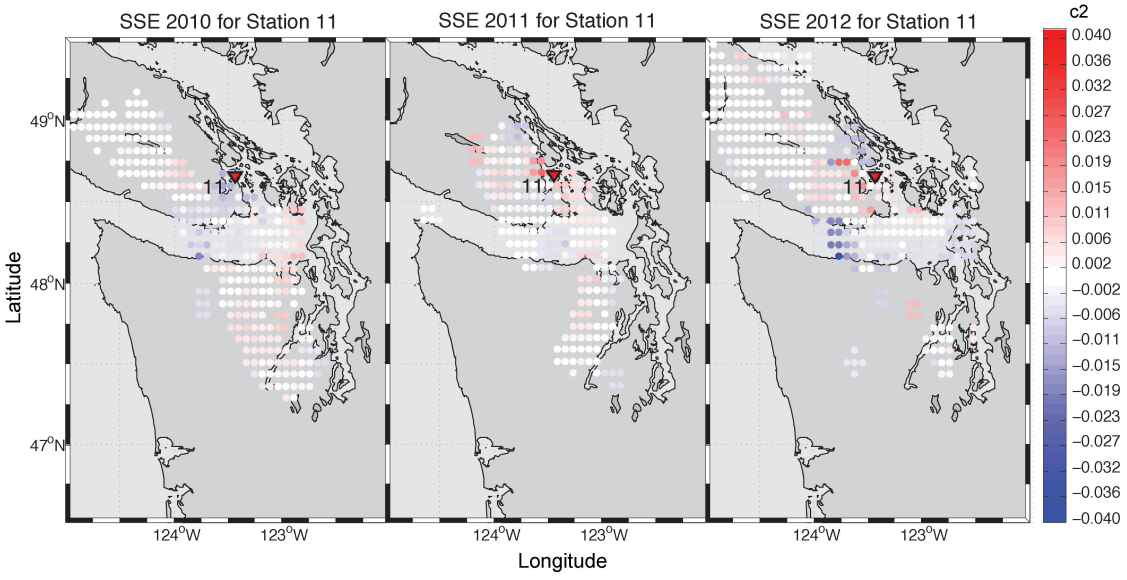

Figure 5.21: Moving average of *c2* for station 11 during the ETS events of 2010, 2011, and 2012. Color is plotted with respect to the mean.

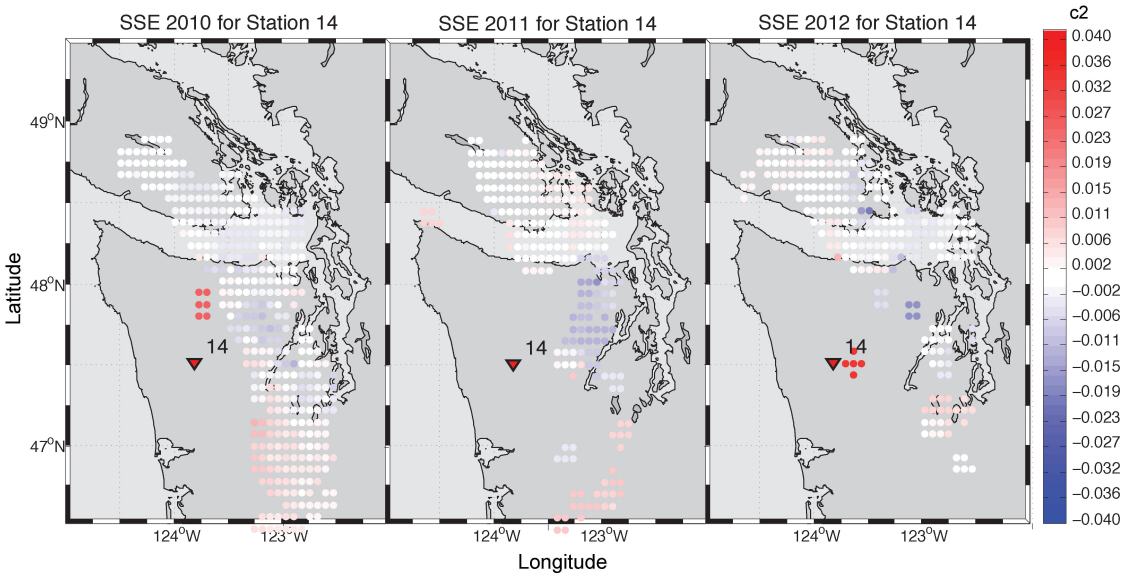

Figure 5.22: Moving average of *c2* for station 14 during the ETS events of 2010, 2011, and 2012. Color is plotted with respect to the mean.

The *c2* term shows higher values closer to the station, more prominently close to stations located right above the tremor events such as Station 1 (Figure 5.16) and Station 6 (Figure 5.18). Stations, 9, 10, and 11 show a noticeably similar map of average values, which is to be expected, as these are one of the groups of co-located stations used in the analysis. While the correspondence is far from perfect, some consistency is apparent in the variability between each of the SSEs for all the seven stations that repeated on all three events.

5.3 Semi-variograms of Attenuation terms

To characterize the spatial variability of the attenuation term for the Cascadia subduction zone, we need to address the spatial correlation of these values. If the *c2* values are dependent on the distance between sources $\Delta H_{i,j}$, where i and j are two different tremor bursts, we can determine values that are consistent with nearby

sources (Walling, 2009; Lin *et al.*, 2011). If we assume *c2* is stationary, then it should only depend on the offset $\Delta H_{i,j}$. By making this assumption, we can compute the semi-variogram (Walling, 2009) of the residuals as follows

$$\gamma_{c2} = \frac{1}{\left(\frac{N_{\Delta H}^2 - N_{\Delta H}}{2}\right)} \sum_{i=1}^{N_{\Delta H}} \sum_{j=1}^{i-1} \left(c2_i - c2_j\right)$$

and this can be used to calculate the correlation distance to which the event pairs can be considered stationary (Walling, 2009) (Figure 5.23).

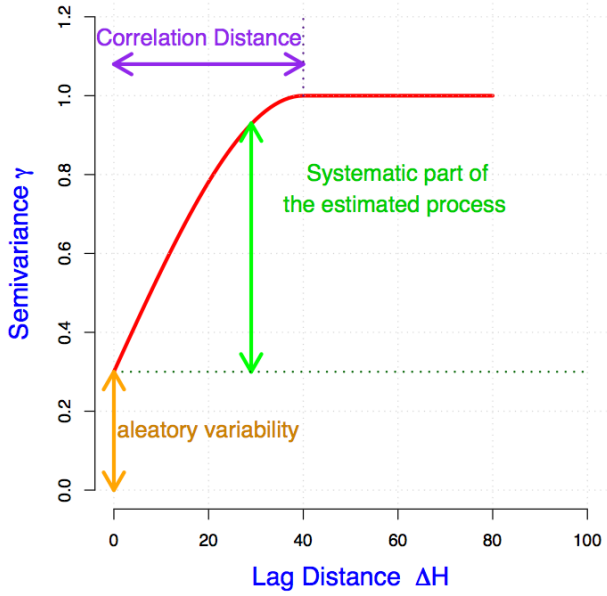

Figure 5.23: From Walling (2009). Relationship of the aleatory variability and epistemic uncertainty to the semi-variogram.

Following the stationarity assumption for *c2*, we have computed the semi-variogram for each station during the three SSEs. The analysis included trials using areas around the stations of different sizes and the semi-variogram for events within annuli that span a range of distances to the station. The test that we performed

included an annulus around the station that would move out every 15 km, 20 km, 50 km, and 150 km to the station, which included all events. We performed these tests to see if there is also a dependence of the *c2* values to the distance from the station. An example of this test is shown in Figure 5.24.

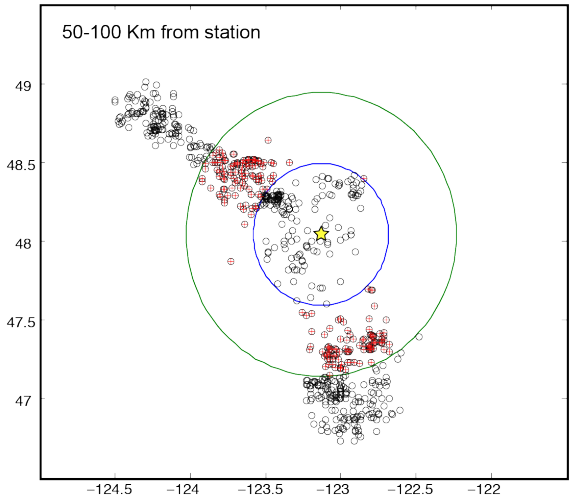

Figure 5.24: Example of the semi-variogram calculation for Station 1 during the 2010 SSE, including the events between 50 and 100 Km to the station shown in red. These are the events between the blue and green circles surrounding the station (yellow star).

During each SSE, a different set of tremor bursts were used for the analysis. The semi-variance is computed using each of these sets separately and plotted on the same semi-variogram for comparison. Baltay and Beroza (2013) focused on events within 150 Km of the stations to ensure that tremor is well observe on each station. To follow their approach, we calculate the semi-variograms using tremor bursts within the same distance. Because of this, for an annulus of 50 Km, three different semi-variograms have to be calculated. One for events between 0-50 Km to the station, the second for events within 50-100 Km to the station, and the third for events within 100-150 Km. Figures 5.25 to 5.34 show the events per SSE and semi-variogram respectively for all stations that repeat within SSE events for the case of a 50 Km annulus. For the co-located set of station 9-11, I have plotted only station 11, due to their similarity.

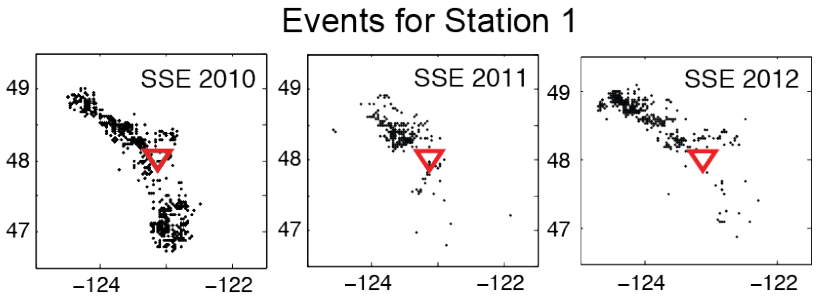

Figure 5.25: Maps for tremor bursts used during each SSE for station 1. Events (black) used to calculate semi-variograms during each SSE in the analysis. Station location is shown with red triangle.

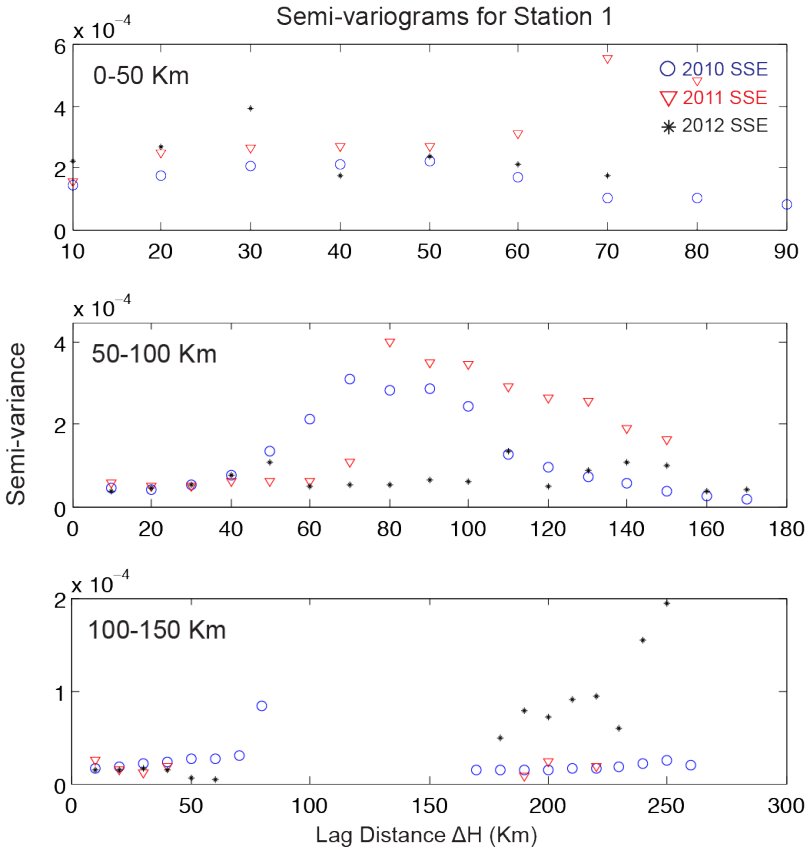

Figure 5.26: Semi-variograms in function of lag distance to station 1. Here I have used an annulus of 50 Km increments. This includes three different annuli cases. From top to bottom, results are shown for annuli of 0-50 Km, 50-100 Km, and 100-150 Km respectively. Blue, red and black symbols represent the semi-variogram for the 2010, 2011, and 2012 SSEs respectively.

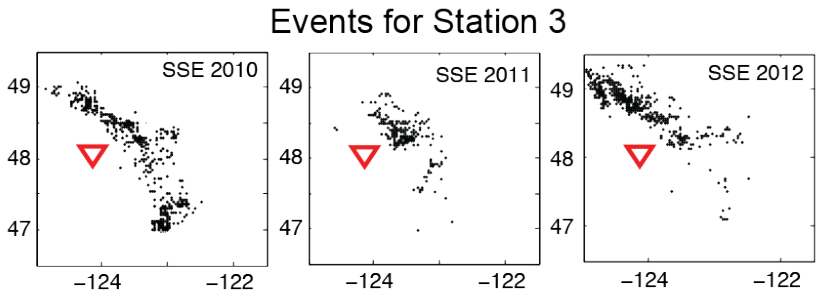

Figure 5.27: Maps for tremor bursts used during each SSE for station 3. Events (black) used to calculate semi-variograms during each SSE in the analysis. Station location is shown with red triangle.

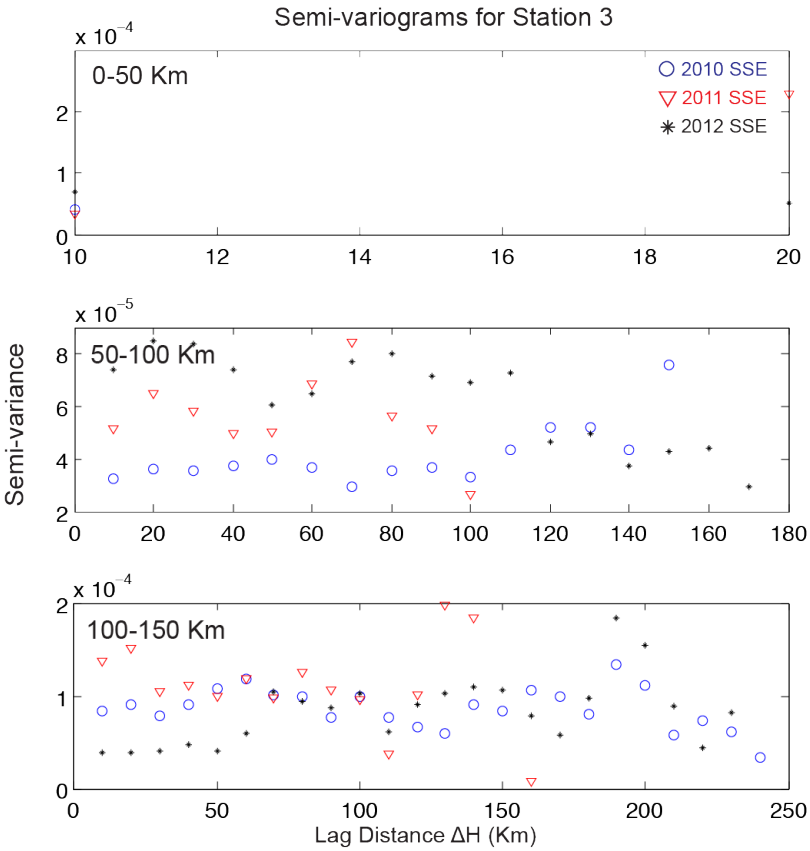

Figure 5.28: Semi-variograms in function of lag distance to station 3. Here I have used an annulus of 50 Km increments. This includes three different annuli cases. From top to bottom, results are shown for annuli of 0-50 Km, 50-100 Km, and 100-150 Km respectively. Blue, red and black symbols represent the semi-variogram for the 2010, 2011, and 2012 SSEs respectively.

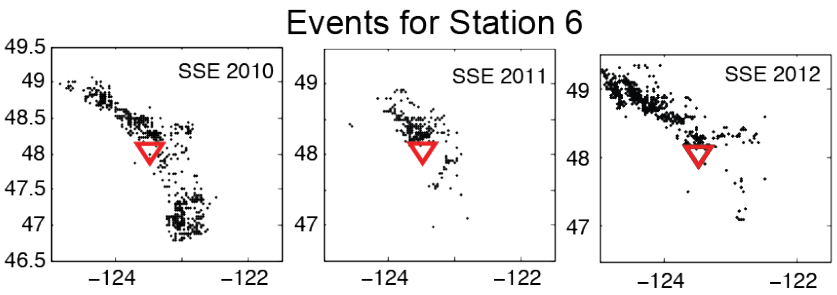

Figure 5.29: Maps for tremor bursts used during each SSE for station 6. Events (black) used to calculate semi-variograms during each SSE in the analysis. Station location is shown with red triangle.

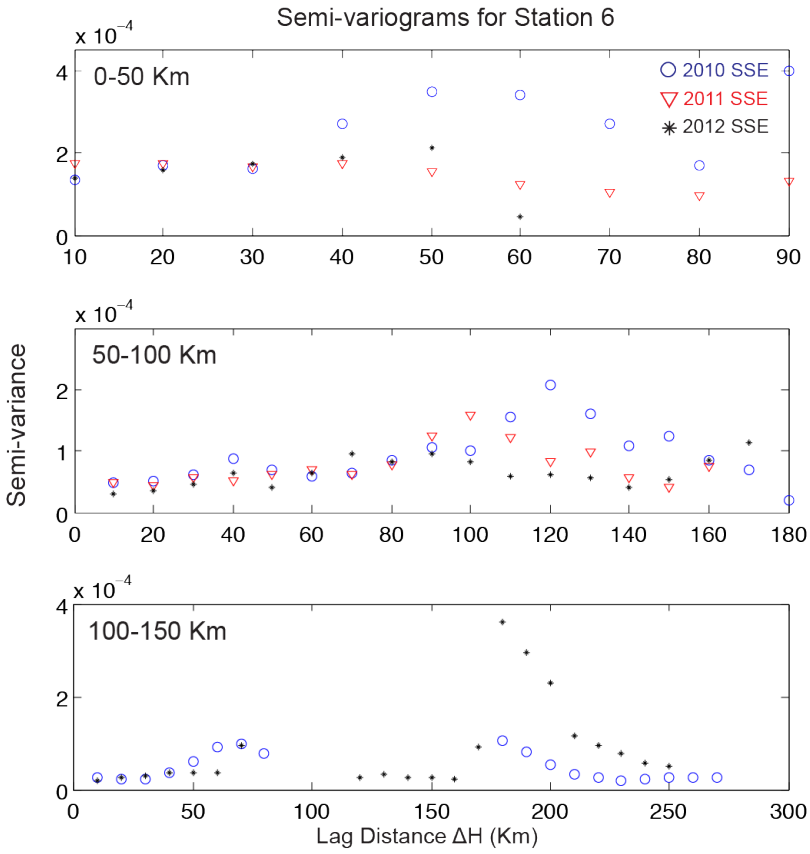

Figure 5.30: Semi-variograms in function of lag distance to station 6. Here I have used an annulus of 50 Km increments. This includes three different annuli cases. From top to bottom, results are shown for annuli of 0-50 Km, 50-100 Km, and 100-150 Km respectively. Blue, red and black symbols represent the semi-variogram for the 2010, 2011, and 2012 SSEs respectively.

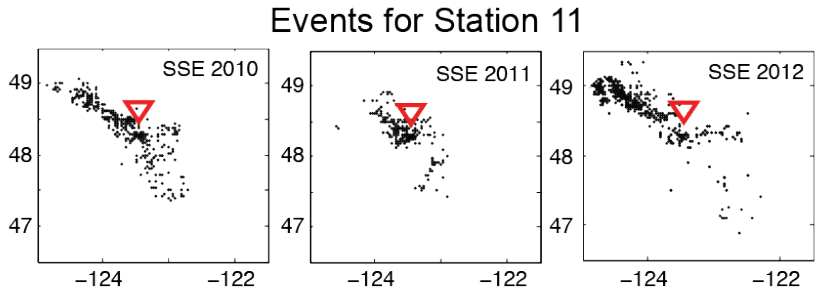

Figure 5.31: Maps for tremor bursts used during each SSE for station 11. Events (black) used to calculate semi-variograms during each SSE in the analysis. Station location is shown with red triangle.

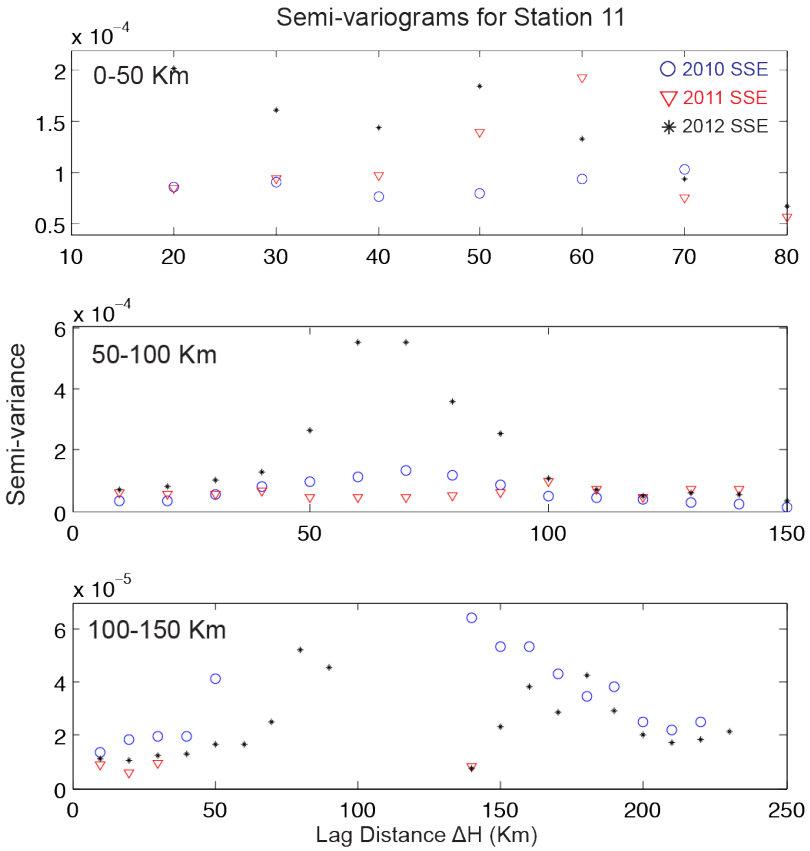

Figure 5.32: Semi-variograms in function of lag distance to station 11. Here I have used an annulus of 50 Km increments. This includes three different annuli cases. From top to bottom, results are shown for annuli of 0-50 Km, 50-100 Km, and 100-150 Km respectively. Blue, red and black symbols represent the semi-variogram for the 2010, 2011, and 2012 SSEs respectively.

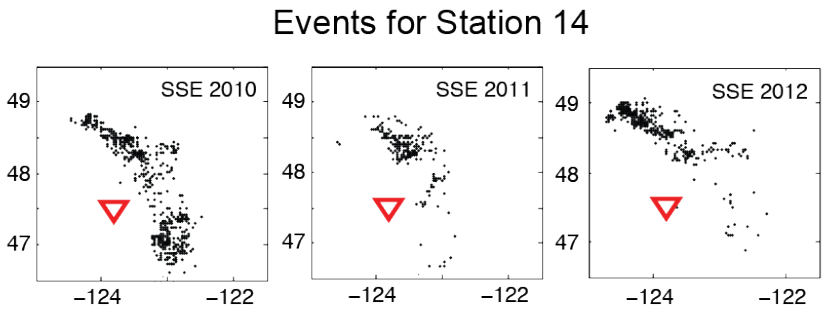

Figure 5.33: Maps for tremor bursts used during each SSE for station 14. Events (black) used to calculate semi-variograms during each SSE in the analysis. Station location is shown with red triangle.

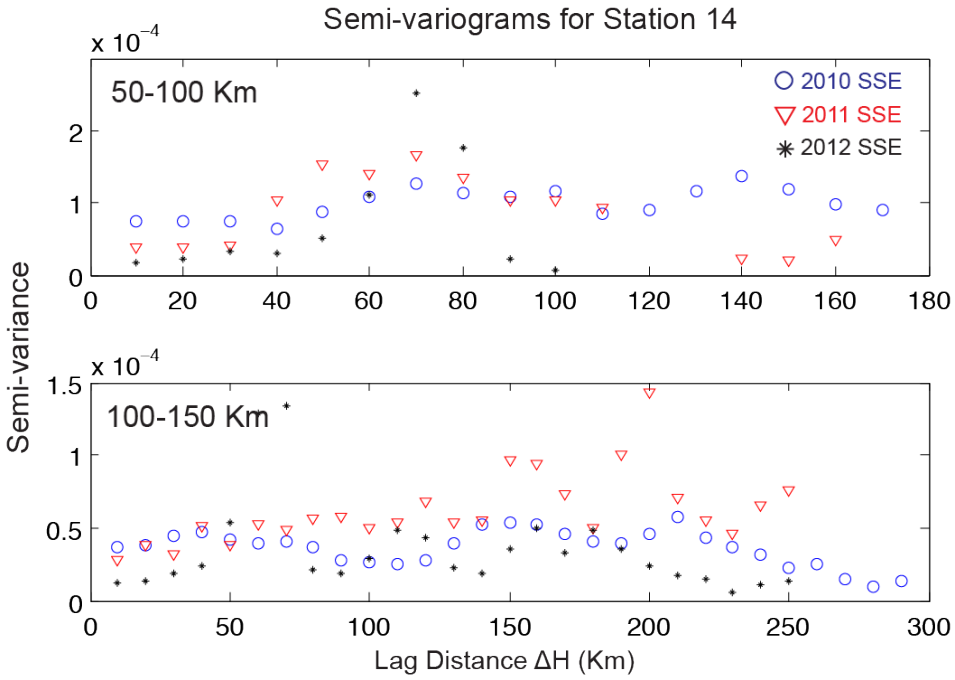

Figure 5.34: Semi-variograms in function of lag distance to station 14. Here I have used an annulus of 50 Km increments. This includes three different annuli cases. From top to bottom, results are shown for annuli of 0-50 Km, 50-100 Km, and 100-150 Km respectively. Blue, red and black symbols represent the semi-variogram for the 2010, 2011, and 2012 SSEs respectively.

From the previous plots we can see that most stations seem to show a slight increasing trend in the semi-variogram with lag distance ΔH. From Figure 5.23 we would expect for the semi-variance values to increase as the distance between events, or lag distance, increases. In theory, events that are further apart should have a greater *c2* difference than events close together. Event though the trend that we see in the semi-variograms is noisy, it is still possible to interpret several observations. For the stations closest to the events, such as station 1 and 6 (Figure 5.26 and 5.30), which are located directly above the tremor bursts, we can see a more clear increasing semi-variance trend for the annuli of 0 to 50 Km and 50 to 100 Km, becoming less clear as the events get further away for the annulus of 100 to 150 Km. A similar case seems to happen for stations further away from the tremor bursts, such as station 14 (Figure 5.34), where the slight increase in the semi-variogram can be observed for both 50 to 100 Km annulus and 100 to 150 Km annulus. Stations that are closer to the events, such as Station 3 and Stations 9 through 11 (co-located) (Figure 5.28 and 5.32), but not right above the SSEs, seem to have the noisier results.

Overall, there is a slight difference in behavior on the semi-variograms between stations, but one similarity does stand out from all stations. The correlation distance at which the semi-variograms seem to become stable increases as the 50 Km annuli gets further away from the station, for all stations that repeat between SSE events. The correlation distance for the annulus between 0 and 50 Km seems to become stable between a lag distance ΔH of 30-50 Km. For the annulus of 50 to 100 Km, the correlation distance seems to be between ΔH of 80-100 Km. And for the annulus of 100 to150 Km, the correlation distance seems to be consistently higher than a ΔH of 100 Km. These observations suggest that as the tremor bursts gets further away form the stations, the estimation of the attenuation terms might be harder to compute, by using a low SNR signal such as tremor. By computing the spatial correlation of *c2* accurately, which seems to be the case for events between 0 to 100 Km from the stations, it will allow us to characterize the special variability of attenuation.

5.4 Discussion and Conclusions

In this chapter we have used Baltay and Beroza (2013) attenuation terms to map the amplitude variability of tremor across the northern Cascadia subduction zone. By analyzing the attenuation terms with respect to hypocentral distance, we find that *c2* values are more highly attenuated as the tremor bursts measured get closer to the stations. This observation agrees closely with a model with a thick attenuation layer overlain by a less attenuating layer suggested by Yabe *et al.* (2014) were attenuation terms decrease as the hypocentral distance increases.

We validate the results obtained for the attenuation values by comparing the attenuation values for repeated tremor events on co-located stations during each of the three ETS events. These comparisons follow the one-to one relationship closely. We show that this is not the case as we compare all the common tremor bursts, for each pair of SSE. As we compare all events we see a large scattering effect for the attenuation terms, although the values seem to cluster around the mean value calculated from all the *c2* values used in the analysis.

Using an area of 10 Km radius, we calculate a spatial average of *c2* for each ETS, using all repeated stations, to understand the variability of *c2* values between the three ETS events. Again, we see that the *c2* term shows higher values closer to stations located right above the tremor events. We can see an apparent consistency in the variability between each of the SSEs for all the seven stations that repeated on all three events.

Lastly, to test the spatial correlation of *c2*, we calculate semi-variograms for each station using a moving annulus of 50 Km. We find that for stations right above the tremor bursts, the semi-variograms are more stable within event lag distances of 0-100 Km. For stations further away from the events, the stability appears at higher lag distances above 50 Km to 150 Km. All stations in the analysis show a similar behavior

for the correlation distance at which the semi-variograms becomes stable, for the different distances to the stations. For events between 0 and 50 Km there is a consistent correlation distance of 30-50 Km. For events between 50 to 100 Km from the station, the correlation distance seems to be between 80-100 Km. And for events 100 to150 Km from the station, the correlation distance seems to be consistently higher than a ΔH of 100 Km. These suggest that as the tremor bursts gets further away form the stations, the estimation of the attenuation terms might be harder to compute.

List of References

Aguiar, A. C., T. I. Melbourne, and C. Scrivner (2007). Tremor Constraints on Moment Release During the 2007 ETS from Surface and Borehole Seismometers (abstract), *American Geophysical Union Fall Meeting 2007*, T13F-03.

Atkinson, G. M., and D. M. Boore (1997). Stochastic Point-Source Modeling of Ground Motions in the Cascadia Region, *Seismological Research Letters* **68**, 1, 74-85.

Atwater, B. F. (1987). Evidence for great Holocene earthquakes along the outer coast of Washington State, *Science* **236**, 942-944.

Atwater, B. F., and A. L. Moore (1992). A tsunami about 1000 years ago in Puget Sound, Washington, *Science* **258**, 5088, 1614-1617.

Atwater, B. F., and E. Hemphill-Haley (1997), Recurrence intervals for great earthquakes in coastal Washington, in *Geological Society of America, 1997 annual meeting*, edited by Anonymous, p. 131, Geological Society of America (GSA).

Atwater, B. F., S. Musumi-Rokkaku, K. Satake, Y. Tsuji, K. Ueda, and D. K. Yamaguchi (2005), University of Washington Press, Seattle, WA.

Audet, P., M. G. Bostock, D. C. Boyarko, M. R. Brudzinski, and R. M. Allen (2010). Slab morphology in the Cascadia fore arc and its relation to episodic tremor and slip, *Journal of Geophysical Research: Solid Earth* **115**, B4, B00A16.

Baltay, A. S., and G. C. Beroza (2013). Ground-motion prediction from tremor, *Geophysical Research Letters* **40**, 24, 2013GL058506.

Bartlow, N. M., S. i. Miyazaki, A. M. Bradley, and P. Segall (2011). Space-time correlation of slip and tremor during the 2009 Cascadia slow slip event, *Geophysical Research Letters* **38**, 18, L18309.

Beroza, G. C., and S. Ide (2011). Slow Earthquakes and Nonvolcanic Tremor, *Annual Review of Earth and Planetary Sciences* **39**, 1, 271-296.

Bostock, M. G., A. A. Royer, E. H. Hearn, and S. M. Peacock (2012). Low frequency earthquakes below southern Vancouver Island, *Geochemistry, Geophysics, Geosystems* **13**, 11, Q11007.

Brown, J. R., G. C. Beroza, and D. R. Shelly (2008). An autocorrelation method to detect low frequency earthquakes within tremor, *Geophysical Research Letters* **35**, 16, L16305.

Brown, J. R., G. C. Beroza, S. Ide, K. Ohta, D. R. Shelly, S. Y. Schwartz, W. Rabbel, M. Thorwart, and H. Kao (2009). Deep low-frequency earthquakes in tremor localize to the plate interface in multiple subduction zones, *Geophysical Research Letters* **36**, 19, L19306.

Brown, K. M., M. D. Tryon, H. R. DeShon, L. M. Dorman, and S. Y. Schwartz (2005). Correlated transient fluid pulsing and seismic tremor in the Costa Rica subduction zone, *Earth and Planetary Science Letters* **238**, 1-2, 189-203.

Chao, K., Z. Peng, C. Wu, C.-C. Tang, and C.-H. Lin (2012). Remote triggering of non-volcanic tremor around Taiwan, *Geophysical Journal International* **188**, 1, 301-324.

Chao, K., Z. Peng, H. Gonzalez-Huizar, C. Aiken, B. Enescu, H. Kao, A. A. Velasco, K. Obara, and T. Matsuzawa (2013). A Global Search for Triggered Tremor Following the 2011 Mw 9.0 Tohoku Earthquake, *Bulletin of the Seismological Society of America* **103**, 2B, 1551-1571.

Chapman, J. S., and T. I. Melbourne (2009). Future Cascadia megathrust rupture delineated by episodic tremor and slip, *Geophys. Res. Lett.* **36**, 22, L22301.

Chuang, L. Y., K. H. Chen, A. Wech, T. Byrne, and W. Peng (2014). Ambient tremors in a collisional orogenic belt, *Geophysical Research Letters* **41**, 5, 2014GL059476.

Delahaye, E. J., J. Townend, M. E. Reyners, and G. Rogers (2009). Microseismicity but no tremor accompanying slow slip in the Hikurangi subduction zone, New Zealand, *Earth and Planetary Science Letters* **277**, 1–2, 21-28.

Douglas, A., J. Beavan, L. Wallace, and J. Townend (2005). Slow slip on the northern Hikurangi subduction interface, New Zealand, *Geophysical Research Letters* **32**, 16, L16305, doi:16310.11029/12005GL023607.

Dragert, H., K. Wang, and T. S. James (2001). A silent slip event on the deeper Cascadia subduction interface, *Science* **292**, 5521, 1525-1528.

Dragert, H., K. Wang, and G. Rogers (2004). Geodetic and seismic signatures of episodic tremor and slip in the northern Cascadia subduction zone, *Earth Planets and Space* **56**, 12, 1143-1150.

Dragert, H., R. D. Hyndman, G. C. Rogers, and K. Wang (1994). Current deformation and the width of the seismogenic zone of the northern Cascadia subduction thrust, *Journal of Geophysical Research* **99**, B1, 653-668.

Eberhart-Phillips, D., and M. Chadwick (2002). Three-dimensional attenuation model of the shallow Hikurangi subduction zone in the Raukumara Peninsula, New Zealand, *Journal of Geophysical Research: Solid Earth* **107**, B2, ESE 3-1-ESE 3-15.

Fisher, R. A. (1973), *Statistical methods for research workers*, 14th ed., rev. and enl. ed., Hafner Pub. Co., New York.

Flück, P., R. D. Hyndman, and K. Wang (1997). Three-dimensional dislocation model for great earthquakes of the Cascadia Subduction Zone, *Journal of Geophysical Research: Solid Earth* **102**, B9, 20539-20550.

Frank, W. B., and N. M. Shapiro (2014). Automatic detection of low-frequency earthquakes (LFEs) based on a beamformed network response, *Geophysical Journal International*.

Frank, W. B., N. M. Shapiro, V. Kostoglodov, A. L. Husker, M. Campillo, J. S. Payero, and G. A. Prieto (2013). Low-frequency earthquakes in the Mexican Sweet Spot, *Geophysical Research Letters* **40**, 11, 2661-2666.

Fry, B., K. Chao, S. Bannister, Z. Peng, and L. Wallace (2011). Deep tremor in New Zealand triggered by the 2010 Mw8.8 Chile earthquake, *Geophysical Research Letters* **38**, 15, L15306.

Gomberg, J., t. Cascadia, and Beyond Working Group (2010). Slow-slip phenomena in Cascadia from 2007 and beyond: A review, *Geological Society of America Bulletin* **122**, 7-8, 963-978.

Gomberg, J., J. L. Rubinstein, Z. G. Peng, K. C. Creager, J. E. Vidale, and P. Bodin (2008). Widespread triggering of nonvolcanic tremor in California, *Science* **319**, 5860, 173-173.

Hyndman, R. D., and K. Wang (1993). Thermal constraints on the zone of major thrust earthquake failure; the Cascadia subduction zone, *Journal of Geophysical Research, B, Solid Earth and Planets* **98**, 2, 2039-2060.

Hyndman, R. D., and K. Wang (1995). The rupture zone of Cascadia great earthquakes from current deformation and the thermal regime, *Journal of Geophysical Research* **100**, B11, 22,133-122,154.

Ide, S. (2010). Striations, duration, migration and tidal response in deep tremor, *Nature* **466**, 7304, 356-359.

Ide, S., D. R. Shelly, and G. C. Beroza (2007a). Mechanism of deep low frequency earthquakes: Further evidence that deep non-volcanic tremor is generated by shear slip on the plate interface, *Geophysical Research Letters* **34**, 3, L03308.

Ide, S., G. C. Beroza, D. R. Shelly, and T. Uchide (2007b). A scaling law for slow earthquakes, *Nature* **447**, 7140, 76-79.

Kao, H., S.-J. Shan, H. Dragert, and G. Rogers (2009). Northern Cascadia episodic tremor and slip: A decade of tremor observations from 1997 to 2007, *J. Geophys. Res.* **114**, B00A12.

Kao, H., S. J. Shan, H. Dragert, G. Rogers, J. F. Cassidy, and K. Ramachandran (2005). A wide depth distribution of seismic tremors along the northern Cascadia margin, *Nature* **436**, 7052, 841-844.

Katsumata, A., and N. Kamaya (2003). Low-frequency continuous tremor around the Moho discontinuity away from volcanoes in the southwest Japan, *Geophysical Research Letters* **30**, 1, 1020.

Kim, M. J., S. Y. Schwartz, and S. Bannister (2011). Non-volcanic tremor associated with the March 2010 Gisborne slow slip event at the Hikurangi subduction margin, New Zealand, *Geophysical Research Letters* **38**, 14, L14301.

La Rocca, M., K. C. Creager, D. Galluzzo, S. Malone, J. E. Vidale, J. R. Sweet, and A. G. Wech (2009). Cascadia tremor located near plate interface constrained by S minus P wave times, *Science* **323**, 5914, 620-623.

Lin, P.-S., B. Chiou, N. Abrahamson, M. Walling, C.-T. Lee, and C.-T. Cheng (2011). Repeatable Source, Site, and Path Effects on the Standard Deviation for Empirical Ground-Motion Prediction Models, *Bulletin of the Seismological Society of America* **101**, 5, 2281-2295.

Linde, A. T., K. Suyehiro, S. Miura, I. S. Sacks, and A. Takagi (1988). Episodic aseismic earthquake precursors, *Nature* **334**, 6182, 513-515.

McCaffrey, R. (2009). Time-dependent inversion of three-component continuous GPS for steady and transient sources in northern Cascadia, *Geophysical Research Letters* **36**, 7, L07304.

McCaffrey, R., L. M. Wallace, and J. Beavan (2008). Slow slip and frictional transition at low temperature at the Hikurangi subduction zone, *Nature Geoscience* **1**, 5, 316-320.

McCaffrey, R., A. I. Qamar, R. W. King, R. Wells, G. Khazaradze, C. A. Williams, C. W. Stevens, J. J. Vollick, and P. C. Zwick (2007). Fault locking, block rotation and crustal deformation in the Pacific Northwest, *Geophysical Journal International* **169**, 3, 1315-1340.

McCausland, W., S. Malone, and D. Johnson (2005). Temporal and spatial occurrence of deep non-volcanic tremor: From Washington to northern California, *Geophysical Research Letters* **32**, 24, L24311, doi:24310.21029/22005GL024349.

Melbourne, T. I., F. H. Webb, J. M. Stock, and C. Reigber (2002). Rapid postseismic transients in subduction zone earthquakes from continuous GPS, *Journal of Geophysical Research* **107**, doi:10.1029/2001JB000555, 2204.

Miller, M. M., T. I. Melbourne, D. J. Johnson, and W. Q. Sumner (2002). Periodic Slow Earthquakes from the Cascadia Subduction Zone, *Science* **295**, 2423.

Miyazawa, M., and J. Mori (2005). Detection of triggered deep low-frequency events from the 2003 Tokachi-oki earthquake, *Geophysical Research Letters* **32**, 10.

Moler, C. (2011), Experiments with MATLAB, edited, MathWorks, Inc., www.mathworks.com/moler/exm/chapters.html.

Nadeau, R. M., and D. Dolenc (2005). Nonvolcanic tremors deep beneath the San Andreas Fault, *Science* **307**, 5708, 389.

Obara, K. (2002). Nonvolcanic deep tremor associated with subduction in Southwest Japan, *Science* **296**, 5573, 1679-1681.

Obara, K., and H. Hirose (2006). Non-volcanic deep low-frequency tremors accompanying slow slips in the southwest Japan subduction zone, *Tectonophysics* **417**, 1–2, 33-51.

Page, L., S. Brin, R. Motwani, and T. Winograd (1999), The PageRank Citation Ranking: Bringing Order to the Web, *Technical Report Rep.*, Stanford InfoLab.

Parsons, T., A. M. Trehu, J. H. Luetgert, K. Miller, F. Kilbride, R. E. Wells, M. A. Fisher, E. Flueh, U. S. ten Brink, and N. I. Christensen (1998). A new view into the Cascadia subduction zone and volcanic arc: Implications for earthquake hazards along the Washington margin, *Geology* **26**, 3, 199-202.

Payero, J. S., V. Kostoglodov, N. Shapiro, T. Mikumo, A. Iglesias, X. Pérez-Campos, and R. W. Clayton (2008). Nonvolcanic tremor observed in the Mexican subduction zone, *Geophysical Research Letters* **35**, 7, L07305.

Peng, Z., and K. Chao (2008). Non-volcanic tremor beneath the Central Range in Taiwan triggered by the 2001 Mw 7.8 Kunlun earthquake, *Geophysical Journal International* **175**, 2, 825-829.

Peterson, C. L., and D. H. Christensen (2009). Possible relationship between nonvolcanic tremor and the 1998-2001 slow slip event, south central Alaska, *Journal of Geophysical Research* **114**, B6, B06302.

Rogers, G., and H. Dragert (2003). Episodic tremor and slip on the Cascadia Subduction Zone: The Chatter of Silent Slip, *Science* **300**, 1942-1943.

Rubinstein, J. L., J. E. Vidale, J. Gomberg, P. Bodin, K. C. Creager, and S. D. Malone (2007). Non-volcanic tremor driven by large transient shear stresses, *Nature* **448**, 7153, 579-582.

Satake, K., K. Wang, and B. F. Atwater (2003). Fault slip and seismic moment of the 1700 Cascadia earthquake inferred from Japanese tsunami descriptions, *Journal of Geophysical Research* **108**, B11.

Satake, K., K. Shimazaki, Y. Tsuji, and K. Ueda (1996). Time and size of a giant earthquake in Cascadia inferred from Japanese tsunami records of January 1700, *Nature* **379**, 6562, 246-249.

Shelly, D. R., G. C. Beroza, and S. Ide (2007a). Complex evolution of transient slip derived from precise tremor locations in western Shikoku, Japan, *Geochemistry Geophysics Geosystems* **8**, Q10014, doi:10010.11029/12007GC001640.

Shelly, D. R., G. C. Beroza, and S. Ide (2007b). Non-volcanic tremor and low-frequency earthquake swarms, *Nature* **446**, 7133, 305-307.

Shelly, D. R., G. C. Beroza, S. Ide, and S. Nakamula (2006). Low-frequency earthquakes in Shikoku, Japan, and their relationship to episodic tremor and slip, *Nature* **442**, 7099, 188-191.

Shelly, D. R., W. L. Ellsworth, T. Ryberg, C. Haberland, G. S. Fuis, J. Murphy, R. M. Nadeau, and R. Bürgmann (2009). Precise location of San Andreas Fault tremors near Cholame, California using seismometer clusters: Slip on the deep extension of the fault?, *Geophysical Research Letters* **36**, 1, L01303.

Szeliga, W., T. Melbourne, M. Santillan, and M. Miller (2008). GPS constraints on 34 slow slip events within the Cascadia subduction zone, 1997–2005, *J. Geophys. Res.* **113**, B4, B04404.

Tang, C.-C., Z. Peng, K. Chao, C.-H. Chen, and C.-H. Lin (2010). Detecting low-frequency earthquakes within non-volcanic tremor in southern Taiwan triggered by the 2005 Mw8.6 Nias earthquake, *Geophysical Research Letters* **37**, 16, L16307.

Wallace, L. M., and J. Beavan (2006). A large slow slip event on the central Hikurangi subduction interface beneath the Manawatu region, North Island, New Zealand, *Geophysical Research Letters* **33**, 11, L11301.

Wallace, L. M., and J. Beavan (2010). Diverse slow slip behavior at the Hikurangi subduction margin, New Zealand, *Journal of Geophysical Research: Solid Earth* **115**, B12, B12402.

Wallace, L. M., J. Beavan, R. McCaffrey, and D. Darby (2004). Subduction zone coupling and tectonic block rotations in the North Island, New Zealand, *Journal of Geophysical Research: Solid Earth* **109**, B12, B12406.

Walling, M. A. (2009), Non-Ergodic Probabilistic Seismic Hazard Analysis and Spatial Simulation of Variation in Ground Motion, University of California, Berkeley.

Walter, J. I., S. Y. Schwartz, J. M. Protti, and V. Gonzalez (2011). Persistent tremor within the northern Costa Rica seismogenic zone, *Geophysical Research Letters* **38**, 1, L01307.

Wech, A. G., and K. C. Creager (2008). Automated detection and location of Cascadia tremor, *Geophysical Research Letters* **35**, L20302, doi:20310.21029/22008GL035458.

Wech, A. G., and N. M. Bartlow (2014). Slip rate and tremor genesis in Cascadia, *Geophysical Research Letters* **41**, 2, 2013GL058607.

Wech, A. G., K. C. Creager, and T. I. Melbourne (2009). Seismic and geodetic constraints on Cascadia slow slip, *J. Geophys. Res.* **114**, B10, B10316.

Yabe, S., A. S. Baltay, S. Ide, and G. C. Beroza (2014). Seismic-Wave Attenuation Determined from Tectonic Tremor in Multiple Subduction Zones, *Bulletin of the Seismological Society of America* **104**, 4, 2043-2059.

Yu, S.-B., H.-Y. Chen, and L.-C. Kuo (1997). Velocity field of GPS stations in the Taiwan area, *Tectonophysics* **274**, 1–3, 41-59.